



Gravity studies of the structure of the Vatnaöldur and Veiðivötn crater rows, South Central Iceland

Jeanne M. Giniaux



**Faculty of Earth Sciences
University of Iceland
2013**

Gravity studies of the structure of the Vatnaöldur and Veiðivötn crater rows, South Central Iceland

Jeanne M. Giniaux

60 ECTS thesis submitted in partial fulfillment of a
Magister Scientiarum degree in Geology

Supervisor
Magnús Tumi Guðmundsson

MS-Committee
Magnús Tumi Guðmundsson
Guðrun Larsen

Examiner
Gylfi Páll Hersir

Faculty of Earth Sciences
School of Engineering and Natural Sciences
University of Iceland
Reykjavik, June 2013

Gravity studies of the structure of the Vatnaöldur and Veiðivötn crater rows, South Central Iceland

Crater row structures from gravity surveying.

60 ECTS thesis submitted in partial fulfillment of a *Magister Scientiarum* degree in Geology

Copyright © 2013 Jeanne M. Giniaux

All rights reserved

Faculty of Earth Sciences
School of Engineering and Natural Sciences
University of Iceland
Sturlugata 7,
101, Reykjavík
Iceland

Telephone: 525 4000

Bibliographic information:

Giniaux, J.M., 2013, *Gravity studies of the structure of the Vatnaöldur and Veiðivötn crater rows, South Central Iceland*, Master's thesis, Faculty of Earth Sciences, University of Iceland, pp. 82.

Printing: Háskólaprent
Reykjavík, Iceland, June 2013

Abstract

A gravity survey was carried out to study the structure and geometry of craters and underlying diatremes formed in two major explosive basaltic fissure eruptions, the ~60 km long AD 871±2 Vatnaöldur and AD ~1477 Veiðivötn fissures in South Central Iceland, both belonging to the Bárðarbunga-Veiðivötn volcanic system. A minor effusive phase at the end of the Veiðivötn eruption filled the bottom of the large phreatomagmatic craters from the main explosive phase, while the Vatnaöldur eruption was almost purely explosive. Six gravity profiles were surveyed across six explosive craters, using a LaCoste&Romberg gravimeter and kinematic GPS. Complete Bouguer anomalies were obtained by integrating the gravitational effects of the mass of the topography using a high-resolution DEM. Studies of the subsurface geometry and structures were made using 2.5-D forward gravity models. The results indicate 100-300 m deep diatreme structures at both Vatnaöldur and Veiðivötn. The purely explosive edifices at Vatnaöldur Innri are filled with relative low density unconsolidated water-saturated tephra, and have much narrower diatremes than those seen at the Veiðivötn fissure, which experienced a late effusive stage leading to lava-filling of the craters. It is proposed that softer subsurface at Veiðivötn led to wider diatremes than found at Vatnaöldur. At least at one of the craters in Vatnaöldur, the activity may have lasted long enough to lead to minor effusive activity, as a relatively high density body, assumed to be lava, fills the diatreme.

Útdráttur

Lýst er rannsókn á byggingu gíga og efsta hluta gosrásar í tveimur stórum tætigosum, Vatnaöldugosinu 871±2 og Veiðivatnagosinu ~1477. Báðar gossprungurnar tilheyra eldstöðvakerfi Bárðarbungu. Til að skoða innri gerð gíga og gosrásar voru sex snið mæld með þyngdarmæli, fjögur yfir gíga í Vatnaöldum og tvö yfir gíga í Veiðivötnum. Botn gíganna úr Veiðivatnagosinu er þakinn hrauni sem rann í lok þess. Í Vatnaöldum virðist hafa verið svo til hreint tætigos. Hæð mælistöðva var ákvörðuð með LaCoste-Romberg þyngdarmæli og KGPS mælingum. Bouguer þyngdarfrávik voru ákvörðuð með heildun stafræns, þéttmökva landlíkans næst mælistað en gisnari landlíkön notuð fjær. Líkanreikningar af byggingu gíganna voru gerðir með 2,5-víðri túlkun, þar sem búnir eru til bergskrokkar með mismunandi eðlismassa en endanlega lengd þvert á mælilínu. Stærð, lögun og eðlismassi bergskrokka er ákvarðaður með hliðsjón af jarðfræði svæðisins og öðrum skorðum, og lögun og eðlismassa hnikað til þar til gott samræmi næst milli mældra frávika og reiknaðra frávika líkansins. Niðurstöðurnar benda til að trektlaga gosrásir, verulega víðari en nokkur berggangur, nái niður á 100-300 m dýpi undir botni gíganna, bæði í Vatnaöldum og í Veiðivötnum. Í gígum í Vatnaöldum innri er gosrásin fyllt gjósku sem veldur þyngdarlægð. Jafnframt eru gosrásirnar mun þrengri en í Veiðivötnum, þar sem hraun frá lokum gossins liggur á botni gíganna. Sprengivirkni í Veiðivötnum virðist hafa myndað breiðari en grynri gosrásir, sem fylltust af hrauni í lok gossins. Vísbendingar eru um að í a.m.k. einum af gígum Vatnaaldna fremri hafihraun myndast í lok gossins, því berg með háan eðlismassa liggur undir gjósku í miðju gígsins.

*To my father, deceased in 2004,
who gave me the scientific curiosity,
and with who I would have loved to talk about my research.*

Table of Contents

List of Figures	ix
List of Tables.....	xii
Acknowledgements	xiii
1 Introduction.....	1
1.1 The geology of Iceland.....	2
1.2 The Eastern Volcanic Zone	4
1.3 The Bárðarbunga-Veiðivötn volcanic system	5
1.4 The AD 871±2 Vatnaöldur and AD ~1477 Veiðivötn eruptions	7
2 Phreatomagmatism.....	9
2.1 Phreatomagmatism, a process of interaction.....	9
2.1.1 Phreatomagmatic eruptive styles	10
2.1.2 Last stages of phreatomagmatic eruptions	11
2.2 Structures of monogenetic phreatomagmatic volcanoes	12
2.2.1 Maar volcanoes	14
2.2.2 Tuff ring and tuff cone volcanoes.....	15
2.2.3 Subsurface diatreme structures	16
2.2.4 Relation between explosive styles and basaltic volcanic structures	18
2.3 Gravity investigations of the structure of explosive monogenetic volcanoes	18
2.3.1 Efficiency and reliability of gravity investigations.....	19
2.3.2 Variations in eruptive styles highlighted from gravity	20
2.4 Choice of the study area	21
3 Gravity theory.....	23
3.1 Basic principles	23
3.2 Gravity reductions	25
3.2.1 Tidal correction.....	25
3.2.2 Drift correction.....	26
3.2.3 Latitude correction.....	26
3.2.4 Free air correction.....	26
3.2.5 Correction for topography: a combined Bouguer and terrain correction.....	27
3.3 Free-air and Bouguer anomalies.....	28
4 Gravity survey, data and methods	29
4.1 Data acquisition.....	30
4.2 Digital Elevation Models.....	31
4.3 Data processing	32
4.3.1 Survey point coordinates.....	32
4.3.2 Reading corrections and free-air anomalies.....	33
4.3.3 Complete Bouguer anomalies	34
4.3.4 Densities.....	35

4.3.5	Accuracy of the Bouguer anomalies.....	41
5	Forward modelling	43
5.1	Forward modelling at Vatnaöldur Innri	46
5.1.1	Profile Va-3	46
5.1.2	Profile Va-4	49
5.2	Forward modelling at Vatnaöldur Fremri	51
5.2.1	Profile Va-1	51
5.2.2	Profile Va-2	52
5.3	Forward modelling of the Veiðivötn profiles Ve-1 and Ve-2.....	55
5.3.1	Profile Ve-2	55
5.3.2	Profile Ve-1	57
6	Discussion	59
6.1	Conduit structures at Vatnaöldur	59
6.2	Conduit structures at Veiðivötn	61
7	Conclusions	65
	References	67
	Appendix A	77
	Appendix B.....	81

List of Figures

Figure 1.1	The geology and tectonic settings of Iceland.....	3
Figure 1.2	The Bárðarbunga-Veiðivötn volcanic system.....	6
Figure 1.3	Geological morphology of the Vatnaöldur and Veiðivötn fissures	8
Figure 2.1	Graph showing the classification of eruptive styles based on the degree of fragmentation (F) and the dispersal (D) of the pyroclastic falls.....	10
Figure 2.2	Schematic cross-section of a maar volcano explaining the terminology used in Table 2.1.....	14
Figure 2.3	Schematic-cross section showing the structure and morphology of a maar-diatreme volcano	14
Figure 2.4	Schematic cross-sections comparing the structures, morphologies and deposits between a tuff ring and a tuff cone	15
Figure 2.5	A diatreme forms by downward migration of the explosion chamber, located in the root zone.....	17
Figure 2.6	Schematic cross-section of a tuff ring volcano and its associated shallow diatreme	17
Figure 2.7	Cross-sections showing the structure of the Mýtina-maar volcano (Central Europe) inferred from 3-D modelling	20
Figure 2.8	Cross-sections through 3-D models highlighting the bulk structures of four tuff ring volcanoes in the Auckland Volcanic Field (New Zealand).....	21
Figure 3.1	The gravity anomaly can be negative (left) or positive (right) and is influenced by the density contrast caused by an anomalous body of density ρ_1 with respect to the surrounding materials having a bulk density ρ_0	24
Figure 3.2	Deflection of the vertical of an angle Φ where \mathbf{g} is the total acceleration of gravity in the presence of an anomalous body, which causes a total gravity anomaly (\mathbf{g}_a).	25
Figure 4.1	Area of study in the Veiðivötn area, South Central Iceland	30
Figure 4.2	Picture taken during the fieldtrip, showing all the equipment required for precise gravity and elevation measurements	31

Figure 4.3	Chart of the distribution of the vertical errors (Δz_{gps}) from the GPS measurements	33
Figure 4.4	The mass effect of the topography is integrated over a square of 100 km-side-length, centred on each survey point	34
Figure 4.5	Graphical representation of the integration of the effect of the bedrock topography over the 25 m grid spacing DEM, using the Nagy formula	35
Figure 4.6	Cross-section over the Vatnaöldur and Veiðivötn fissures.....	37
Figure 4.7	Bedrock geology at the Vantaöldur and Veidivötn fissures, and immediate surroundings	37
Figure 4.8	Density determinations of the topographic formations along the Vatnaöldur profiles using the Nettleton's method	40
Figure 4.9	Density determinations of the topographic formations along the Veidivötn profiles using the Nettleton's method	41
Figure 5.1	Schematic cross-section of a 2.5-D gravity forward model defining the terminology used for modelling descriptions.....	44
Figure 5.2	Bodies of same densities having different shapes and lying at different depths can produce the same gravity anomaly	44
Figure 5.3	Topographic map of the area of study	46
Figure 5.4	Observed gravity anomaly (top) along the Va-3 profile (Vatnaöldur Innri)	47
Figure 5.5	2.5-D gravity forward modelling highlighting the volcanic structure of the edifice crossed by the Va-3 gravity profile (Vatnaöldur Innri).....	48
Figure 5.6	2.5-D gravity forward modelling highlighting the volcanic structure of the edifice crossed by the Va-4 gravity profile (Vatnaöldur Innri).....	50
Figure 5.7	2.5-D gravity forward modelling highlighting the volcanic structure of the edifice crossed by the Va-1 gravity profile (Vatnaöldur Fremri).....	53
Figure 5.8	2.5-D gravity forward modelling highlighting the volcanic structure of the edifice crossed by the Va-2 gravity profile (Vatnaöldur Fremri).....	54
Figure 5.9	2.5-D gravity forward modelling highlighting the volcanic structure of the edifice crossed by the Ve-2 gravity profile (Veiðivötn).....	56
Figure 5.10	2.5-D gravity forward modelling highlighting the volcanic structure of the edifice crossed by the Ve-1 gravity profile (Veiðivötn).....	58
Figure 6.1	Schematic cross-section showing the phreatomagmatic structure of the purely explosive Va-4 edifice.....	61

Figure 6.2 Schematic cross-section showing the phreatomagmatic structure of the explosive Ve-1 edifice	62
--	----

List of Tables

Table 2.1	Comparisons between maar, tuff ring and tuff cone volcanoes	13
Table 4.1	Information about the gravity base station JH (at Jökulhleimar)	34
Table 4.2	Density of Quaternary and Holocene rocks in Iceland	36
Table 4.3	Bulk basaltic tephra densities determined from density measurements.....	38
Table 4.4	Density values of the topographic formations inferred from the Nettleton's method.....	39
Table 5.1	Half-strike lengths of the polygons determined from the approximate crater diameters.	45
Table 6.1	Approximate dimensions of the volcanic edifices at Vatnaöldur (Va-) and Veiðivötn (Ve-)	60

Acknowledgements

I would like to express my gratitude, first and foremost, to my supervisor Magnús Tumi Guðmundsson for his guidance, useful comments and availability during this master project, despite his very busy schedule. Thanks to him, I learnt a lot about phreatomagmatic eruptions and also about gravity, this great geophysical tool that I had only briefly heard about before. My gratitude also goes to Guðrun Larsen, for her kind help in providing me with the geological knowledge and articles related to the area of study. Without her, the completion of the thesis would not have been possible. I also wish to warmly thank Dís Högnadóttir for all the time she allowed me in software explanations and for the useful additional data she supplied me. Special thanks to Þorbjörg Ágústadóttir for her generous contribution of experience and nice company during the fieldwork. I also want to thank Rósa Ólafsdóttir for her useful help in ArcGis problems and for having allowed me saving a lot of digitalization time by giving me topographic data. I also thank Finnur Pálsson for his helpful explanations about GPS data analysis, and Páll Einarsson and Bryndís Bransdóttir for helping me find old articles. Many thanks to Þorsteinn Jónsson who stopped at my area for taking samples. I finally would like to thank all the staff at the Institute of Earth Sciences for their assistance and support during my two years of master at the University of Iceland.

I am grateful to thank the scientist Jan Mrlina for having provided me with useful articles and for our interesting email exchanges. I also would like to thank, Flora Grabowska, Peter Kokelaar and James D.L. White who also provided me with useful articles.

Special thanks to my uncle Jean Boissonnas, and my friend Lynn Erler, who kindly reviewed my thesis, for correcting my English and for their useful comments and advice regarding scientific style. And many thanks to Pascale Bizet for the last-minute English corrections.

I also want to thank my mother, my sister, my boyfriend and my friends for their support during the hardest times.

I finally would like to thank my French engineering school in geology, called LaSalle Beauvais, for having allowed me to undertake this master degree in Iceland as an equivalence of my fifth year. I thank all the staff from LaSalle Beauvais for the knowledge and experience I acquired there, which appeared very useful for completing my project.

1 Introduction

Phreatomagmatism characterizes explosive volcanic eruptions resulting from the interaction between hot rising magma and relatively cold fluid (e.g. Morrissey *et al.*, 2000). Basaltic phreatomagmatic eruptions commonly form monogenetic (i.e. single volcanic event) maar-diatreme volcanic structures (e.g. Lorenz *et al.*, 1970; Lorenz, 1986; White and Ross, 2011). A few places in the world where entire maar-diatreme structures outcrop, e.g. Hoppi Buttes in Arizona and Suoana maar-diatreme in Japan (White, 1991; Geshi *et al.*, 2011), have been widely studied from a petrographic point of view in order to understand the mechanisms of phreatomagmatic eruptions. Laboratory studies have revealed the details of the fragmentation mechanism associated with fuel-coolant interaction (e.g. Zimanowski, 1998). However, some aspects of phreatomagmatism are still not entirely understood because in most areas the whole structures do not outcrop, preventing the overall comprehension of the explosive system.

Local gravity investigations have proved to be efficient in detecting and characterizing buried phreatomagmatic structures (e.g. Mrlina *et al.*, 2009) as clear density contrasts often exist between the conduit filling materials and the surrounding bedrock. Gravity can therefore be very useful for understanding better the volcanic history of explosive volcanic edifices (e.g. Cassidy *et al.*, 2007).

The AD 871±2 Vatnaöldur and AD ~1477 Veiðivötn eruptions (e.g. Larsen, 1984; Larsen *et al.*, 2013) were both large tholeiite explosive fissure eruptions that occurred in a high groundwater level area in South Central Iceland. They respectively produced ~5 km³ and ~10 km³ (freshly fallen volumes) of basaltic tephra from discontinuous crater rows. Tephra from both events can be traced over large parts of Iceland. From geological mapping, the AD 871±2 Vatnaöldur eruption is considered to have been almost purely explosive; whereas the AD ~1477 Veiðivötn eruption became effusive at the end of volcanic activity.

The aim of the present study is to reveal and compare conduit structures of the Vatnaöldur and Veiðivötn crater rows by performing gravity profiling across relevant craters from both fissures (four profiles cross Vatnaöldur whereas two cross Veiðivötn).

The study addressed two main questions:

- What is the structure of the conduits at the selected volcanic edifices that formed during the AD 871±2 Vatnaöldur and AD ~1477 Veiðivötn phreatomagmatic eruptions and are there differences between both crater rows?
- What can those crater/conduit structures tell about the mechanism of the two eruptions and how do they compare with the results of other studies of similar volcanic structures?

The present chapter gives a brief overview of the geology of the study area. The second chapter outlines the process of phreatomagmatism and the common resulting volcanic structures. Gravity theory detailing the basic principles and the gravity reductions composes the third chapter. The methods for data acquisition and data processing are provided in the fourth chapter and the fifth chapter presents the results obtained from forward gravity modelling. A discussion, summary and conclusions are found in Chapters 6 and 7.

1.1 The geology of Iceland

Iceland straddles the N-S mid-Atlantic ridge (MAR), having an average spreading rate of 1.8 cm per year in the direction N105°E (Gudmundsson, 2000). Volcanism in Iceland is generated from the interaction between the MAR and a mantle plume, which has been highlighted by P- and S-wave structures from both seismic refraction (e.g. Pálmason, 1971; Gebrande *et al.*, 1980; Darbyshire *et al.*, 1998) and teleseismic tomography (e.g. Bijwaard and Spakman, 1999; Wolfe *et al.*, 1997; Foulger *et al.*, 2001). The Iceland plume is described as a narrow cylindrical zone of relatively hot material extending from ~75 km to at least ~400 km in depth, centred in the northwestern edge of Vatnajökull (Figure 1.1) (Bjarnason, 2008). Both relatively high volcanic activity (Saemundsson, 1978) and seismic activity (Einarsson, 1991) are observed above the centre of the Iceland plume where the crust is anomalously thick (38-40 km) (Darbyshire *et al.*, 1998).

The surface expressions of the volcanic activity in Iceland are the neovolcanic zones (Figure 1.1) (e.g. Saemundsson, 1978; Jakobsson, 1979a; Gudmundsson, 2000). Saemundsson (1978) defined two types of neovolcanic zones: the “axial rift zones” marking the plate boundary with extensive crustal spreading; and the “lateral rift zones”, also called the flank zones, where there is almost no spreading activity (Figure 1.1).

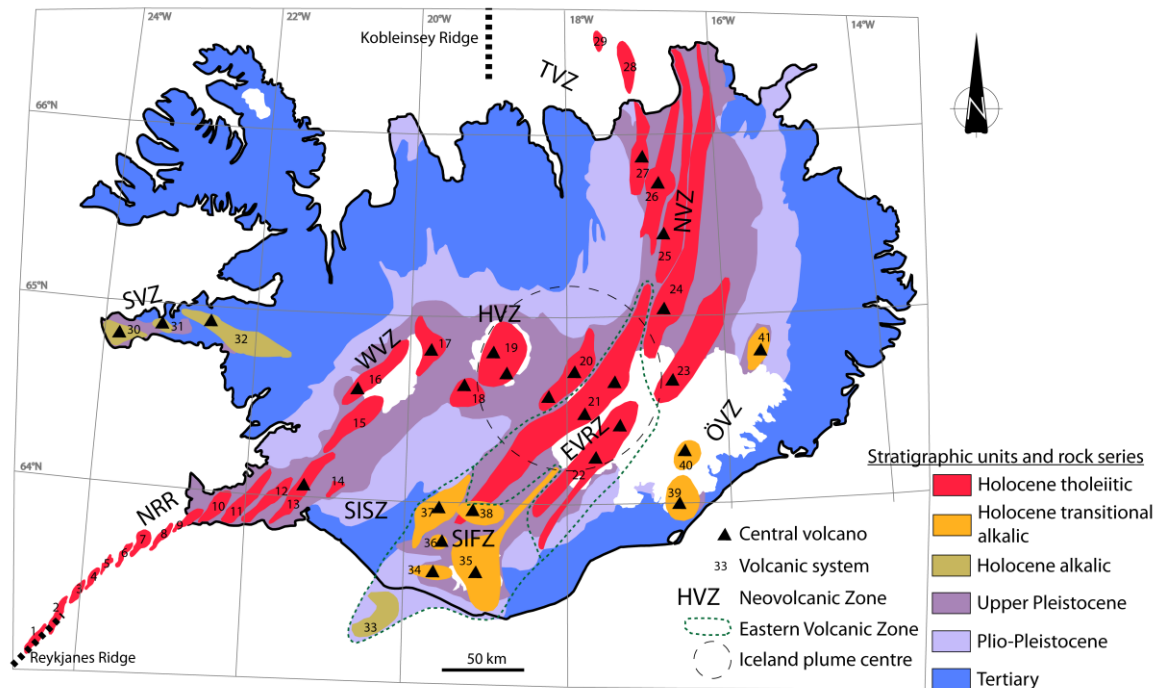


Figure 1.1 The geology and tectonic settings of Iceland. The axial rift zones are the Northern Volcanic Zone (NVZ), the Eastern Volcanic Rift Zone (EVRZ), the Hofsjökull Volcanic Zone (HVZ), the Western Volcanic Zone (WVZ) and the Northern Reykjanes Ridge (NRR). The lateral rift zones are the Snæfellsnes Volcanic Zone (SVZ), the Örfajökull Volcanic Zone in eastern Iceland (ÖVZ), and the South Iceland Flank Zone (SIFZ). Both the EVRZ and the SIFZ form the Eastern Volcanic Zone (EVZ). The transform zones are the Tjörnes Fracture Zone (TFZ) and the South Iceland Seismic Zone (SISZ). The volcanic systems of the EVZ are Bárðarbunga-Veiðivötn (21), Grimsvötn (22), Vestmannaeyar (33), Eyjafjallajökull (34), Katla (35), Tindfjallajökull (36), Hekla (37) and Torfajökull (38). The biggest glacier is named Vatnajökull (Based on Sigmundsson, 2006; Jakobsson *et al.*, 2008; Thordarson and Höskuldsson, 2008; and references therein).

The neovolcanic zones on land are composed of 29 volcanic systems (Figure 1.1) (Jóhannesson and Saemundsson, 1998; Jakobsson *et al.*, 2008). A volcanic system usually consists of fissure swarms and at least one central volcano that often has produced intermediate and silicic products as well as basalts. The fissure swarms are commonly characterized by graben structures and crater rows producing mafic basalt (Saemundsson, 1978; Jakobsson, 1979b). Each volcanic system may produce magma with specific petrographical and geochemical characteristics (Jakobsson, 1979a,b).

The eruptive styles in Iceland have been mainly controlled by environmental conditions throughout time. During the Holocene (<10,000 years), basaltic phreatomagmatic eruptions (e.g. Thordarson and Höskuldson, 2008; Larsen and Eiríksson, 2010), and effusive basaltic eruptions, including large basaltic flood lava episodes (e.g. Thordarson and Höskuldson, 2008) are the two main eruptive styles recorded in Iceland. The former relates to either subglacial or other wet environments; whereas the latter is an indicator of purely sub-aerial eruptions (Thordarson and Höskuldson, 2008).

The Icelandic crust began to form during late Tertiary (3.1 to 16 million years ago). Lava shield volcanoes and crater rows are the two main Tertiary volcanic structures, mostly characterized by basaltic tholeiitic flood lava eruptions (Saemundsson, 1979; Hardarson *et al.*, 2008). The Plio-Pleistocene (0.7 to 3.1 million years ago) and the Upper-Pleistocene (0.01 to 0.7 million years ago) were characterized by alternative periods of cold and warm climate, leading to subglacial explosive activity and aerial flood lava eruptions, respectively (Saemundsson, 1979; Sigmundsson, 2006). Subglacial activity was prominent due to the repeated growth of an ice cap that extended beyond the present coast of Iceland at the end of the Upper-Pleistocene (Geirsdóttir and Eiríksson, 1994): extensive hyaloclastites, pillow lavas and breccias were produced from hyaloclastite ridges and tuyas and such activity still occurs under present-day glaciers (e.g. Gudmundsson, 2005; Jakobsson and Gudmundsson, 2008).

Several key volcanic eruptions have been recorded and dated using tephrochronology (Thorarinsson, 1979) and demonstrate that the EVZ was the most active neovolcanic zone during the Holocene, with both a relatively high eruption frequency rate (from years to decades) and the highest magmatic production (e.g. Larsen *et al.*, 1998; Thordarson and Larsen, 2007; Larsen and Eiríksson, 2008a; Larsen and Eiríksson, 2008b; Thordarson and Höskuldsson, 2008).

1.2 The Eastern Volcanic Zone

The EVZ is composed of 8 volcanic systems distributed over two subvolcanic zones: Grímsvötn and Bárðarbunga-Veiðivötn are tholeiitic volcanic systems, belonging to the Eastern Volcanic Rift Zone (EVRZ); whereas Katla, Hekla, Vestmannaeyar, Eyjafjallajökull, Tindfjallajökull and Torfajökull are more silicic volcanic systems, belonging to the South Iceland Flank Zone (SIFZ) (Figure 1.1) (Jakobsson, 1979a; Jóhannesson and Saemundsson, 1998; Thordarson and Höskuldsson, 2008; Jakobsson *et al.*, 2008).

In the EVZ, prehistorical times (i.e. before 1,100 years ago) were characterized by large ($>1 \text{ km}^3$), high-discharge ($>1,000 \text{ m}^3 \text{ s}^{-1}$) basaltic lava flood episodes (Thordarson *et al.*, 2003; Thordarson and Larsen, 2007; Thordarson and Höskuldsson, 2008) as well as several hundred explosive eruptions (e.g. Óladóttir *et al.*, 2011). The historical period was mainly characterized by large basaltic explosive events, either due to subglacial activity under the Vatnajökull icecap or due to high groundwater levels within the fissure swarms (e.g. Larsen and Eiríksson, 2008b).

Before the Holocene, records are scarcer but extensive subglacial activity may have occurred in the EVZ during the Pleistocene, as it was covered by ice (Geirsdóttir and Eiríksson, 1994): the nature of the bedrock of the EVZ mostly consists of hyaloclastite and other subglacial deposits (Jóhannesson and Saemundsson, 1998).

About 80% of the volcanic events recorded after the Norse Settlement occurred in the EVZ. Grímsvötn, Bárðarbunga-Veiðivötn, Katla and Hekla volcanic systems, have been the most active volcanic systems, respectively (e.g. Thordarson and Larsen, 2007).

Two main reasons have been suggested to explain such high volcanic activity in the EVZ, and above all in the EVRZ: (1) the EVRZ lies just above the centre of the inferred Iceland plume (Figure 1.1); (2) the EVZ accommodates almost all the spreading compared to its

parallel neighbour, the WVZ (LaFemina *et al.*, 2005). The spreading axis is located along the eastern edge of the Bárðarbunga-Veiðivötn volcanic system, decreasing, from 19.0 ± 2.0 mm per year in the north-east to 8 ± 2.0 mm per year towards the SIFZ in the south-west (LaFemina *et al.*, 2005).

1.3 The Bárðarbunga-Veiðivötn volcanic system

The Bárðarbunga-Veiðivötn volcanic system partly lies under the northwestern part of the Vatnajökull ice cap, i.e. above the centre of the Iceland plume (Figure 1.1). From Holocene records, it is the second most active volcanic system after the Grímsvötn system and the fourth most productive in terms of erupted magma volumes, after the Katla, Grímsvötn and Hekla volcanic systems, respectively (e.g. Thordarson and Larsen, 2007; Thordarson and Höskuldsson, 2008).

In terms of size, Bárðarbunga-Veiðivötn is the largest volcanic system in Iceland, being ~190 km long, ~28 km wide and covering a total area of ~2500 km² (Thordarson and Larsen, 2007; Jóhannesson and Saemundsson, 1998). Nearly 60 km of the length are ice-covered. The Bárðarbunga-Veiðivötn volcanic system lies on a bedrock mainly composed of Upper Pleistocene hyaloclastite formations (see section 1.1) and is one of the two purely tholeiite volcanic systems of the EVZ, the other being Grímsvötn (Jakobsson, 1979a; Jóhannesson and Saemundsson, 1998). No high temperature geothermal field has been found within the volcanic system (Jakobsson, 1979a).

Bárðarbunga is the dominant central volcano of the volcanic system (Björnsson and Einarsson, 1990; Jóhannesson and Saemundsson, 1998). A second auxiliary central volcano, Hamarinn, has been inferred to be part of the Bárðarbunga volcanic system (Figure 1.2) (Thorarinsson *et al.*, 1973; Gudmundsson and Högnadóttir, 2007). Its existence may be an indicator of a high magma supply over limited period followed by sporadic lateral magma movements (Gudmundsson and Högnadóttir, 2007).

The fissure swarms of the Bárðarbunga-Veiðivötn volcanic system are oriented NE-SW, i.e. following the MAR rifting axis direction (Jóhannesson and Saemundsson, 1998). The Dyngjuháls fissure swarm extends to the northeast part of the system; whereas the Veiðivötn fissure swarm intersects the Torfajökull central volcano in the southwesternmost part of the system (Figure 1.2) (Björnsson and Einarsson, 1990; Larsen, 1984). The Veiðivötn fissure swarm is composed of numerous NE-SW fissures from 10 to 67 km-long (e.g. Larsen *et al.*, 2008).

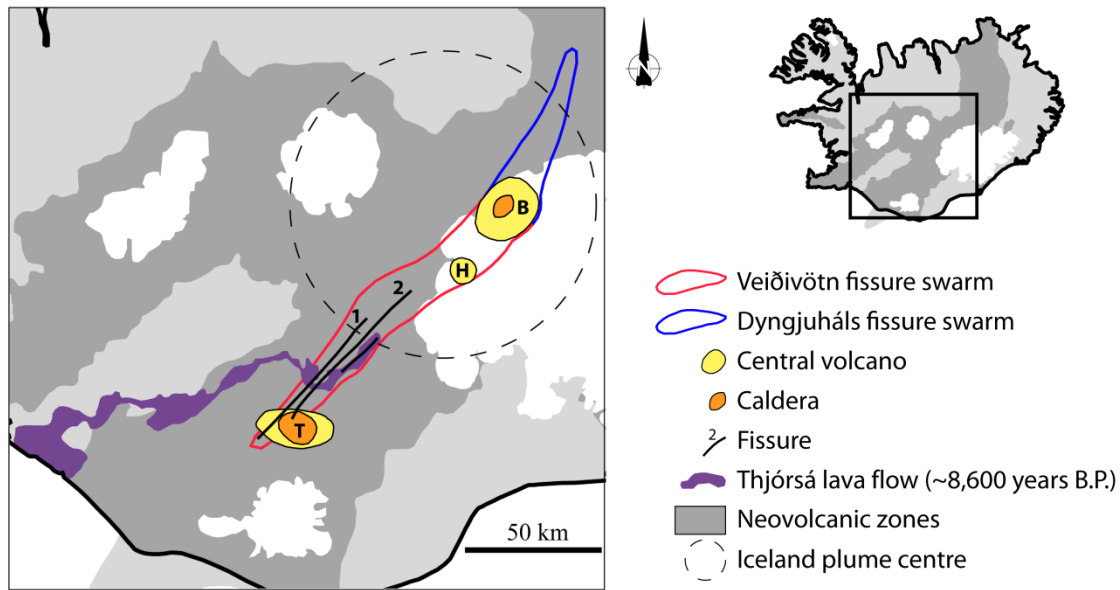


Figure 1.2 The Bárðarbunga-Veiðivötn volcanic system has two central volcanoes, Bárðarbunga (B) and Hamarinn (H), and two main volcanic fissures known from historical phreatomagmatic episodes, Vatnaöldur (1) and Veiðivötn (2) (Based on Jónsson *et al.*, 1997; Jakobsson *et al.*, 2008; Thordarson and Höskuldsson, 2008; Larsen *et al.*, 2013 and references therein).

The eastern edge of the south part of the Bárðarbunga volcanic system, i.e. along the Veiðivötn fissure swarm, is the location of the highest spreading in the EVRZ; therefore, this region accumulates the maximum strain of the EVZ (Jónsson *et al.*, 1997; LaFemina *et al.*, 2005). This phenomenon may explain the relatively high rifting activity recorded within the Veiðivötn fissure swarm during the Holocene (LaFemina *et al.*, 2005). Before the Norse Settlement, during a warm period, a sequence of at least 10 large tholeiite basaltic flood lava eruptions, referred to as the Tungnaá lavas, have been verified as originating from the Veiðivötn fissure swarm (e.g. Vilmundardóttir, 1977; Jakobsson, 1979a; Jakobsson, 1979b; Hjartarson, 1988; Thordarson *et al.*, 2003; Halldórsson, 2007). The Thjórská eruption is the earliest and biggest flood episode of this lava sequence (~8,600 years B.P.): ~25 km³ of erupted lava extended up to the south coast, over ~140 km (Figure 1.2). The Thjórská eruption is also one of the largest flood events on Earth with the longest lava flow in Iceland (Thordarson and Höskuldsson, 2008). The Tungnaá lavas flowed within the Tungnaá and Thjórská riverbeds and gradually raised the groundwater level within the Veiðivötn fissure swarm. One or more lakes formed within the volcanically active area as a result of a lava dam by an eruption nearly 2,000 years ago (Larsen, 1984). During historical times, two of the main rifting episodes, the AD 871±2 Vatnaöldur (Larsen 1984; Grönvold *et al.*, 1995) and the AD ~1477 Veiðivötn (Larsen, 1984; Larsen *et al.*, 1998; Thorarinson, 1976) eruptions, occurred in this “wet” part of the Veiðivötn fissure swarm, leading to phreatomagmatic eruptive episodes that produced large amounts of basaltic tephra (e.g. Larsen, 1984; Jónsson *et al.*, 1997; Larsen *et al.*, 2013). In parallel, 23 explosive subglacial eruptions have been recorded in the Bárðarbunga volcanic system during historical times (e.g. Larsen, 2002; Larsen and Eiríksson, 2008b). Volcanic activity at Bárðarbunga and even at Grímsvötn may have occurred at the same time as the AD ~1477 Veiðivötn fissure eruption (e.g. Larsen, 1984; Larsen *et al.*, 1998; Larsen, 2002). A periodic major rifting activity at intervals of 600 to 800 years has been suggested at the

Veiðivötn fissure swarm, implying lateral magma movement from the Bárðarbunga central volcano (Larsen, 1984).

In total, during the entire Holocene, the Bárðarbunga-Veiðivötn volcanic system has erupted at least 57 km³ of basaltic magma in subaerial episodes, and ~10 km³ of basaltic magma has been estimated from subglacial eruptions (including both the AD 871±2 Vatnaöldur and AD ~1477 Veiðivötn eruptions) (Thordarson *et al.*, 2003). For the last decades, the Veiðivötn fissure swarm has been aseismic (e.g. Einarsson, 1991; Jakobsdóttir 2008), but it is still considered as an active volcanic region and eruptions similar to the large historical episodes may be expected in the future (Larsen, 1984; LaFemina *et al.*, 2005).

1.4 The AD 871±2 Vatnaöldur and AD ~1477 Veiðivötn eruptions

The AD 871±2 Vatnaöldur (Larsen 1984; Grönvold *et al.*, 1995) and AD ~1477 Veiðivötn (Larsen, 1984; Larsen *et al.*, 1998; Thorarinson, 1976) eruptions occurred during the two most recent rifting episodes on the Bárðarbunga-Veiðivötn volcanic system (EVRZ). They took place along the western parts of the NE-SW discontinuous 60 km-long Vatnaöldur and 67 km-long Veiðivötn fissures, respectively (Figure 1.2) (Larsen, 1984; Larsen, 2005). In this part of the Veiðivötn fissure swarm, the environmental settings had been modelled by large prehistorical flood episodes that raised the groundwater level by filling up the riverbeds of the Tungnaá and Thjórsá rivers (see section 1.2). The Vatnaöldur fissure formed along the Veiðivötn lake basin during the AD 871±2 Vatnaöldur eruption that modified again the environmental settings, creating the temporary, large, tephra-dammed Langalón lake (~140 km²) (e.g. Larsen, 1984; Larsen, 2005; Larsen *et al.*, 2013). The Veiðivötn fissure formed in the middle of the basin of the former Langalón, during the AD ~1477 Veiðivötn eruption that altered again the hydrological context and new temporary lakes were created before the tephra dams broke (e.g. Larsen, 1984; Larsen, 2005; Larsen *et al.*, 2013). The high groundwater-level explains the large predominance of phreatomagmatic activity during both the AD 871±2 Vatnaöldur and AD ~1477 Veiðivötn eruptions. However, the AD ~1477 Veiðivötn eruption can be classified as a “mixed eruption” as the explosive activity changed into an effusive style at the end of the event: small amounts of lava filled the bottom of the craters (Larsen, 1984; Larsen, 2005).

Phreatomagmatic explosive activity dominated on a ~25 km-long discontinuous portion of the AD 871±2 Vatnaöldur fissure. In case of the AD ~1477 Veiðivötn event, the phreatomagmatic activity occurred along a fairly continuous ~31 km of the Veiðivötn fissure (Larsen, 1984; Larsen, 2005). Both explosive phases may have lasted for 1-5 days (Larsen, 2005). The bulk of the tephra produced during both events was tholeiite basalt (Larsen, 1984) but some magma mixing and hybridization occurred in the southwesternmost part of the Veiðivötn fissure swarm, where it enters the Torfajökull volcanic system (Blake, 1984; Zellmer *et al.*, 2008). The AD ~1477 Veiðivötn basaltic tephra was coarser than the bulk of the AD 871±2 Vatnaöldur ash, being lapilli and ash size and contained some non-juvenile lithics of alluvial and lacustrine origin (Larsen, 2005). A volume of ~5 km³ basaltic tephra (freshly fallen volume) within the 0.5 cm isopach, was emitted during the AD 871±2 Vatnaöldur eruption; whereas the AD ~1477 Veiðivötn eruption produced ~10 km³ of basaltic tephra (freshly fallen volume) (Larsen, 2005). During each event, the tephra expelled out of craters and crater rows (Figure 1.3),

coalescing into a tephra layer with a maximum thickness of 12 meters (Larsen, 1984; Larsen, 2005).

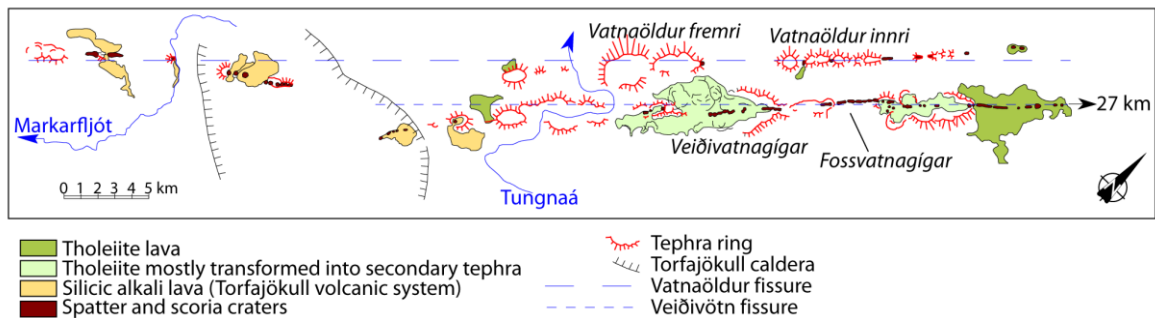


Figure 1.3 Geological morphology of the Vatnaöldur and Veiðivötn fissures (Larsen *et al.*, 2013).

The AD 871±2 Vatnaöldur tephra layer dispersed almost in all directions around the fissure, covering an area of 50,000 km² within the 0.5 cm isopach but has also been identified in some Greenland ice cores (e.g. Grönvold *et al.*, 1995). The AD ~1477 Veiðivötn tephra layer covers an area of 53,000 km² on land towards the E, NE, and NNE (Larsen, 1984; Larsen, 2005) and the 1 cm isopach extends offshore in North Iceland (Larsen *et al.*, 2002; Larsen and Eiríksson, 2010; Larsen *et al.*, 2013). Tephrostratigraphy and tephrochronology studies have pinpointed the probable presence of the AD ~1477 Veiðivötn tephra layer in both western Ireland (Chambers *et al.*, 2004) and Central Sweden (Davies *et al.*, 2007).

The large thickness of the tephra layers and their extensive dispersal characterize both the AD 871±2 Vatnaöldur and AD ~1477 Veiðivötn events as Phreatoplinian eruptions according to the classification scheme of Walker (1973, 1980) (see further, Figure 2.1 and section 2.2.4), the latter being the largest explosive eruption in Iceland, recorded in historical times (Larsen, 2005; Thordarson and Larsen, 2007; Larsen and Eiríksson, 2008b).

2 Phreatomagmatism

The Vatnaöldur and Veidivötn fissures (e.g. Larsen, 1984) were both formed in phreatomagmatic activity. A large amount of tholeiitic basaltic tephra was emitted during each explosive event (see section 1.4), forming aligned monogenetic edifices (i.e. formed during one single event), such as tuff rings and tuff cones with maar-like craters up to 1.8 km in diameter (Jakobsson, 1979a; Larsen, 1984; Thordarson and Larsen, 2007).

Few places in the world display outcropping phreatomagmatic conduits of such monogenetic explosive volcanoes, e.g. the Hoppi Buttes in Arizona (e.g. White, 1991) and the Suoana volcano in Japan (Geshi *et al.*, 2011); and have therefore enabled a better understanding of the volcanic structures and the related phreatomagmatic mechanisms. Some relatively recent geophysical investigations (gravity and magnetics) have completed the information by highlighting the overall geometry of some buried explosive volcanic structures (e.g. Cassidy *et al.*, 2007; Mrlina *et al.*, 2007; Mrlina *et al.*, 2009).

This chapter summarizes current knowledge of the phreatomagmatic processes that mostly arise from petrographic studies and experiments (e.g. Wohletz, 1983; Zimanowski, 1998), and focuses on morphological aspects. Firstly, the overall phreatomagmatism process is briefly explained; the resultant explosive structures are then compared and some forward geophysical models similar to the present gravity investigation are tackled. Finally, the reasons for focusing on the Vatnaöldur and Veidivötn fissures for this study are explained.

2.1 Phreatomagmatism, a process of interaction

Subaerial phreatomagmatic activity (or hydrovolcanic activity) is based on the interaction between magma and water, leading to explosive eruptions. Most of the water required originates from external non-magmatic sources, i.e. groundwater or surface water (e.g. sea water, meteoric water, lake water) (e.g. Lorenz *et al.*, 1970; Morrissey *et al.*, 2000; Houghton *et al.*, 2000).

The magma-water interaction process is analogous to an industrial explosion called “fuel-coolant interaction” (FCI): an extremely rapid conductive heat transfer occurs from the magma (fuel) to the water (coolant), converting thermal energy into kinetic energy in a short period of time (e.g. Wohletz, 1983; Zimanowski, 1998; Morrissey *et al.*, 2000). Experiments on remelted lava and water revealed that vapour films develop when the water is trapped within the magma, which becomes partly insulated (Zimanowski, 1998). Collapse of the vapour films due to disturbance causes the rapid heat transfer that superheats the water. As a result, the magma undergoes a rapid thermal contraction, leading to its fragmentation into small particles (e.g. Zimanowski, 1998) called pyroclasts or tephra (e.g. Francis and Oppenheimer, 2004).

The heated water then flash boils and volumetrically expands, causing a fast explosive vaporization cloud generated by a shockwave, due to the increase in hydrostatic and dynamic pressure (e.g. Lorenz *et al.*, 1970; Wohletz and Sheridan, 1983; Zimanowski, 1998; Morrissey *et al.*, 2000; Lorenz, 2000). The shockwaves (or explosive bursts) occur

periodically, by the cyclic formation and collapse of the vapour films (Wholetz, 1983; Zimanowski, 1998; Morrissey *et al.*, 2000).

The degree of explosivity is controlled by numerous parameters, the most important of which being (1) the area of contact surface between magma and water, (2) the depth of the “explosion chamber” (Lorenz, 2000) where the fragmentation occurs, (3) the local water/magma ratio, (4) the difference in temperature and the pressure conditions, (5) the magma ascent rate and (6) the propagation of shockwaves through the mixing zone. (e.g. Wohletz, 1983; Vespermann and Schmincke, 2000). The stronger the explosivity, the stronger both the fragmentation and the transportation of the fragments, the finer the pyroclasts (Wohletz, 1983).

The hydrological and geological settings are variable, leading to the production of a great diversity of phreatomagmatic eruptions that are relatively difficult to classify strictly (Morrissey *et al.*, 2000; White and Houghton, 2000).

2.1.1 Phreatomagmatic eruptive styles

A classification of both magmatic and phreatomagmatic eruptive styles, based on both the degree of fragmentation of pyroclastic falls (F) and their area of dispersal (D), was first suggested by Walker (1973) and refined later (Self and Sparks, 1978; Walker, 1980) (Figure 2.1). The Surtseyan (Walker, 1973) and Phreatoplinian (Self and Sparks, 1978) are the two main phreatomagmatic eruptive styles encountered on Earth.

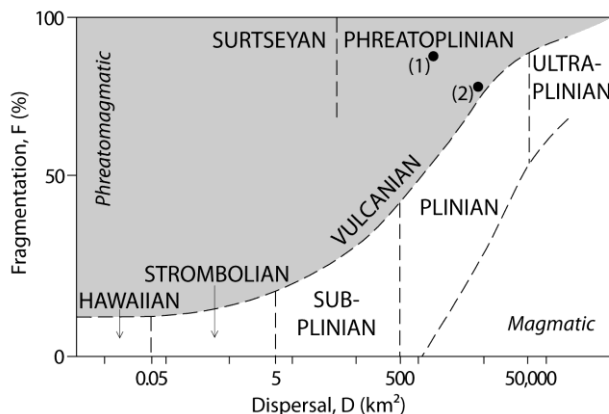


Figure 2.1 Graph showing the classification of eruptive styles based on the degree of fragmentation (F) and the dispersal (D) of the pyroclastic falls where (1) refers to the AD 871±2 Vatnaöldur eruption and (2) corresponds to the AD ~1477 Veiðivötn eruption (After Thordarson and Höskuldson, 2008, based on Larsen, 2005). F corresponds to the percentage of pyroclasts finer than 1 mm at the point where the 0.1 T_{max} crosses the axis of dispersal; whereas D is the area enclosed by the 0.01 T_{max} isopach; T_{max} being the maximum thickness of tephra measured (Walker, 1973).

Surtseyan eruptions (named after the 1963 Surtsey eruption in Iceland) are either characterized by explosive jets of ash (cock’s tails or cypressoid) during intermittent activity or by continuous upsursh activity carrying tephra to much greater heights (e.g. White and Houghton, 2000). Both resulting from the interaction between a rising basaltic magma and water (e.g. Morrissey *et al.*, 2000; Francis and Oppenheimer, 2004). This phreatomagmatic interaction leads to high fragmentation (F ~80-90%) and the eruption

height may reach several kilometers. However, the Surtseyan being moderately intense, the dispersion is restricted to 50 km^2 ($D < 50 \text{ km}^2$) (Figure 2.1) (Walker, 1973).

Some authors have differentiated the Surtseyan style from the Taalian style (Kokelaar, 1986) (named after the 1965 eruption of the Taal volcano in Phillipines) by noticing a slight difference in magma-water interaction processes (e.g. Wohletz and Sheridan, 1983; Kokelaar, 1986; Vespermann and Schmincke, 2000): a Taalian eruption is due to the interaction of ascending magma with external lacustrine water entering the volcanic vent; whereas a Surtseyan eruption results from the interaction of ascending magma and external seawater as the magma enters the water body (Kokelaar, 1986). Therefore, relatively less water is involved in Taalian eruptions, leading to more powerful eruptions. Note that when authors only consider the Surtseyan style, it is used for characterizing both lacustrine and seawater interactions as the explosive power is similar.

Depending upon the water/magma ratios, the amount of heat energy involved per unit time in any phreatomagmatic eruption is variable, causing the transformation of the water either into steam (or even superheated steam) or into a 2-phase fluid (vapour and liquid) that leads to “dry” or “wet” phreatomagmatic eruptions, respectively (Wohletz and Sheridan, 1983; Morrissey *et al.*, 2000). Therefore, Surtseyan and Taalian eruptions can be subdivided into either wet or dry eruptions (e.g. Sohn, 2012). Note that because of the relatively larger amount of water available, Surtseyan eruptions are commonly “wetter” than Taalian eruptions (e.g. Morrissey *et al.*, 2000).

Phreatoplinian eruptions are poorly understood large eruptions that commonly result from the interaction of silicic magma with a large amount of external water, during an explosive eruption of a polygenetic volcano (i.e. volcano built from numerous eruptive episodes) (Houghton *et al.*, 2000). The explosivity occurs at deeper levels than during Surtseyan eruptions, i.e. $\sim 1 \text{ km}$ depth (e.g. Kokelaar, 1986) and the explosivity is more powerful. The high degree of explosivity of Phreatoplinian eruptions converts most of the water into steam, leading to dry phreatomagmatic eruptions with respect to Surtseyan and Taalian eruptions (Morrissey *et al.*, 2000). The three more relevant indicators defining Phreatoplinian eruptions are (1) a wide dispersion of tephra ($D > 50 \text{ km}^2$) (Figure 2.1), (2) a high degree of fragmentation similar to Surtseyan eruptions and (3) fine-grained fallout deposits near the eruption site (Self and Sparks, 1978; Houghton *et al.*, 2000). The duration of a Phreatoplinian eruption usually lasts from hours to weeks or months (Houghton *et al.*, 2000).

2.1.2 Last stages of phreatomagmatic eruptions

During any phreatomagmatic eruption, when the explosion becomes too weak compared to the depth of the explosion site to allow the eruptive cloud to reach the surface, the explosive eruption slows down. This stage usually marks the end of the fragmentation process, and consequently, the end of the explosive phase (Lorenz and Kurszlaukis, 2007). If no magma is supplied to the system anymore, the phreatomagmatic structure becomes water-saturated and post-eruptive subsidence occurs due to compaction and diagenesis in the crater (Lorenz and Kurszlaukis, 2007). However, if there is still some supply of magma, the cessation of explosivity is generally due to a lack of water available: the transition from explosive into effusive styles may occur (e.g. Lorenz *et al.*, 1970). Water

usually lacks in the system either when (1) the magma ponds above the groundwater level, or when (2) the magma has sealed the walls of the volcanic conduit (Houghton *et al.*, 2000). The most common effusive styles observed in transition from phreatomagmatic styles are either Strombolian or Hawaiian, and commonly lead to the formation of scoria cones or lava lakes, respectively (Lorenz, 1986; Houghton *et al.*, 1999). If the transition into effusive occurs at the last stage of volcanic activity, the magma may only fill the conduit without reaching the surface (e.g. White, 1991) or a small amount of magma may reach the surface and be buried by post-eruptive deposits (Lorenz, 2003). Note that the opposite transition from effusive to explosive style may also occur if water is added to the magmatic system (e.g. Geshi *et al.*, 2011).

2.2 Structures of monogenetic phreatomagmatic volcanoes

Monogenetic volcanoes commonly result from basaltic phreatomagmatic eruptions (e.g. Lorenz *et al.*, 1970). A typical explosive monogenetic volcano consists of a crater, surrounded by a tephra ring encircling a cone-shaped conduit called a diatreme (e.g. Lorenz *et al.*, 1970; White and Ross, 2011). Note that the polygenetic complex structures resulting from Phreatoplinian eruptions (e.g. Francis and Oppenheimer) are not detailed here as none of the volcanic edifice considered in the present study presents such landforms.

As seen in section 2.1, environmental settings lead to specific degrees of explosivity, producing different styles of phreatomagmatic eruptions. Consequently, both the surface and subsurface structures of the resulting monogenetic volcanoes may be different. Maars, tuff rings and tuff cones are the most common explosive monogenetic landforms (Table 2.1), and the most common subaerial volcanoes observed on land after scoria cones (Vespermann and Schmincke, 2000); they are usually associated with various different subsurface diatremes in terms of size (e.g. Lorenz *et al.*, 1970; White and Ross, 2011).

After each explosion burst of any on-going explosive eruption at a monogenetic volcano, (see section 2.1), an eruptive cloud, composed of vaporized water and tephra, reaches the surface. Water condenses again, due to cooling and decompression, leading to large tephra fallout deposition inside the crater (primary deposits) by base surges and fallout (Table 2.1); whereas proximal tephra deposits pile up as thin beds (commonly from several millimetres to few meters thick) surrounding the crater to form the ejecta ring (Lorenz, 2003). Pyroclastic surge processes are responsible for bedding tephra deposition where each bed commonly refers to one shockwave (see section 2.1) (Wohletz, 1983). In large phreatomagmatic eruptions, creating large tephra rings, substantial fallout deposits can extend ten to hundreds of kilometres beyond the crater (e.g. Larsen, 1984).

Poorly vesiculated deposits of glassy juvenile materials are typically observed in any phreatomagmatic eruptions at monogenetic volcanoes (e.g. Geshi *et al.*, 2011), and accretionary lapilli and vesiculated tuff may form in case of wet phreatomagmatic eruption (see section 2.1) (Table 2.1) (White and Ross, 2011).

Table 2.1 Comparisons between maar, tuff ring and tuff cone volcanoes (Based on White and Ross, 2011 and references therein; Wohltez and Sheridan, 1983; Kokelaar, 1986; and Vespermann and Schmincke, 2000). Refer to Figure 2.2 for terminology.

	Maar volcanoes	Tuff ring volcanoes	Tuff cone volcanoes
Bottom of the crater above/below groundwater level*	Below	Above (usually)	Above
Volume of erupted material (km ³)	?	0.0001 to 1	0.0001 to 1
Ring (or crater) diameter	Usually 200-300 m	Usually 200-300 m	Between 100 and 300 m
Average thickness of tephra	< 30 m on average	< 50 m (can reach 200 m)	Between 100 and 300 m
Dip of beds at the rims	Sub-horiz. to 20°	Sub-horiz. to 20°	10-30°
Stratification	Well-stratif. (1 to 5 cm intervals)	Well-stratif. (1 to 5 cm intervals)	Massive (10 cm to 1 m intervals) or weakly stratif.
Dominant grain size	Ash and lapilli	Ash and lapilli	Ash and lapilli
Proportion of non-juvenile fragments	Up to 90%	Variable	A few % or less
Vesicular juvenile fragments	Possible	Possible	Possible
Dense to poorly vesicular juvenile fragments	Typically abundant	Typically abundant	Typically abundant
Transport mode of pyroclasts	Base surges (dominant) and fallout	Base surges (dominant) and fallout	Base surges, fallout (dominant) and remobilize
Vesiculated tuffs	Possible	Possible	Possible
Accretionary lapilli	Common	Common	Common
External water	Limited	Abundant to limited	Abundant
Diatreme thickness	Deep	Shallow	Absent
Palagonitization	Little or no	Little of no	Highly

*Conditions after the end of the eruption.

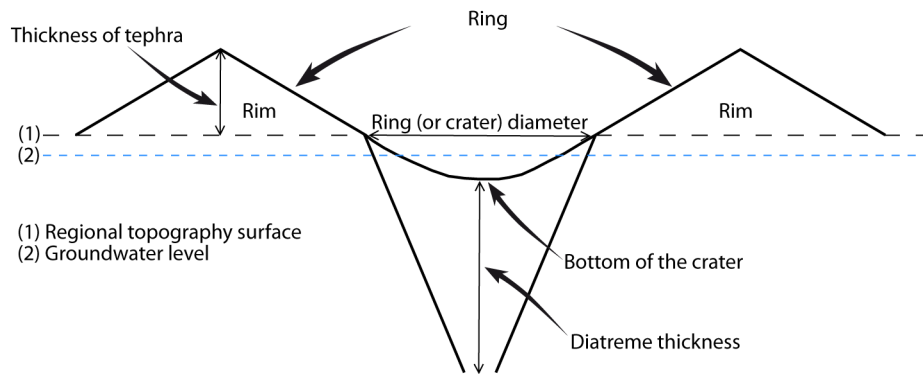


Figure 2.2 Schematic cross-section of a maar volcano explaining the terminology used in Table 2.1. Note that (1) and (2) can be at the same elevation (Based on Vespermann and Schmincke, 2000).

2.2.1 Maar volcanoes

A maar is a monogenetic volcano named after its relatively large and shallow explosive crater having a diameter-to-depth ratio of at least 3:1, which has been cut into the pre-eruption surface (Lorenz *et al.*, 1970; Lorenz, 1986; White and Ross, 2011). Maar crater diameters vary between less than 100 m to more than 1,500 m and usually measure several tens of meters in depth (some can exceed a depth of 500 m) (Lorenz, 1986). A maar crater is usually surrounded by a relatively small ejecta ring (10-30 m thick on average) (Table 2.1) that does not have a specific name. In some cases, the ejecta ring surrounding a maar crater can be high enough to be called a tuff ring (e.g. Geshi *et al.*, 2011) but it rarely matches the characteristics of a tuff cone (Lorenz *et al.*, 1970; Wohltz and Sheridan, 1983; Lorenz, 1986; White and Ross, 2011). A deep diatreme commonly develops beneath a maar (Figure 2.3).

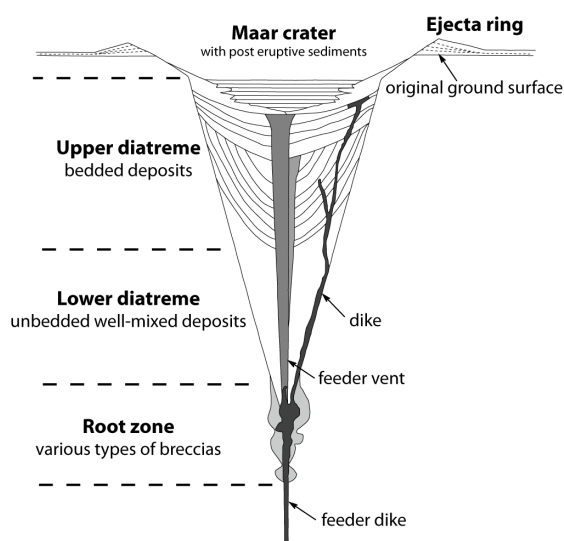


Figure 2.3 Schematic-cross section showing the structure and morphology of a maar-diatreme volcano (Scale 1:1) (From Lorenz, 2003).

2.2.2 Tuff ring and tuff cone volcanoes

Tuff rings and tuff cones are monogenetic volcanoes named after their specific ejecta rings. Tuff rings have characteristic low topographic slopes associated with low dip beds that commonly do not exceed 20° and the height of the tuff ring rims usually does not exceed 50 m (Table 2.1) (Wohltez and Sheridan, 1983; White and Ross, 2011). Tuff cones have higher profiles and steeper slopes than tuff rings (Figure 2.4); their rim heights are greater than for tuff rings, measuring usually between 100 and 300 m; the beds commonly dip between 10 and 30° (Table 2.1) (Wohltez and Sheridan, 1983; White and Ross, 2011).

Tuff ring volcanoes have wide pyroclast-filled craters similar to maar craters, but that rarely lie below the groundwater surface (Lorenz *et al.*, 1970; Lorenz, 1986; White and Ross, 2011). Tuff cone craters also commonly lie above the groundwater level (Wohltez and Sheridan, 1983; White and Ross, 2011).

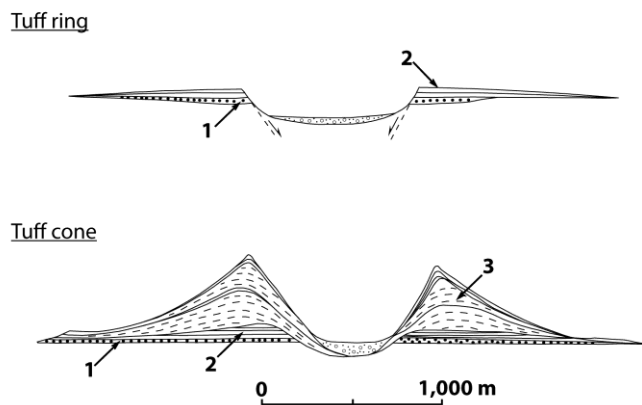


Figure 2.4 Schematic cross-sections comparing the structures, morphologies and deposits between a tuff ring and a tuff cone. 1: Explosion breccias; 2: Thinly bedded deposits; 3: Thickly bedded deposits (Wohltez and Sheridan, 1983).

The primary dominant process leading to the morphological difference between tuff rings and tuff cones is the deposition process that is mostly the result of pyroclastic surges in the formation of tuff rings and tuff cone structures are mainly formed by fallouts (Table 2.1) (e.g. White and Ross, 2011; Sohn, 2012).

The base of tuff ring and tuff cone ejecta rims is commonly made of an angular coarse-grained pyroclastic deposit called “explosion breccia” (Wohltez and Sheridan, 1983) (Figure 2.4). Those basal deposits consist mainly of country rock fragments measuring from 2 cm to more than 1 m supported by an ash and lapilli matrix, emplaced by dominant ballistic falls and minor surges (Wohltez and Sheridan, 1983). “Thinly bedded deposits”, emplaced mostly by pyroclastic surges, overlie the basal “explosion breccias” and consist of large amounts of juvenile lapilli and ash tephra mixed with relatively low amounts of accidental clasts (the lithic pyroclasts rarely exceed 50% of the unit) (Wohltez and Sheridan, 1983; Vespermann and Schmincke, 2000). Only tuff cones present an overlying unit of “thickly bedded deposits” that can be 1 m thick on average and consists of pyroclastic surge deposits interbedded with thin layers of poorly bedded fine ash resulting

from fallout deposition (Wohltey and Sheridan, 1983; Vespermann and Schmincke, 2000; White and Ross, 2011). Asymmetric ejecta rings are usually caused by strong wind conditions (Wohltey and Sheridan, 1983; Vespermann and Schmincke, 2000).

2.2.3 Subsurface diatreme structures

The subsurface cone-shaped diatremes are most prominent under maar volcanoes (Table 2.1). The diatreme-filling materials consist mostly of juvenile and lithic pyroclasts of ash and lapilli size, but large blocks of country rocks can also be observed (Lorenz *et al.*, 1970). A diatreme is commonly composed of three units having fairly different deposits characteristics: (1) the root zone, characterized by an irregular shape, represents the bottom end of the diatreme, being the transition between the feeder dike and the (2) lower diatreme that underlies the (3) upper diatreme (Figure 2.3) (e.g. White, 1991; Lorenz, 2003; Geshi *et al.*, 2011; White and Ross, 2011).

The root zone is the site of fragmentation (see section 2.1). It can exceed 50 m in width and 500 m in depth (Lorenz and Kurszlaukis, 2007 and references therein). The root zone is mainly composed of various types of breccia deposits originating either from country rocks (“contact breccias”, “subsidence breccias” and “breccias formed by rockfalls or rockslides”), or from volcanoclastic materials of the lower diatreme unit (“diatreme rocks”) (Lorenz and Kurszlaukis, 2007). The rework and chaotic aspect of the root zone deposits suggests some current movements through many “ejection/fallback” cycles caused by the fragmentation process (e.g. White, 1991; Geshi *et al.*, 2011).

The lower diatreme is mostly characterized by non-bedded reworked pyroclasts originating from both the rising juvenile material and the non-juvenile wall rocks. The deposits are coarsely arranged as a relatively homogeneous or well-mixed unit, due to the circulatory system of “ejection/fallback” process (e.g. White, 1991; Lorenz, 2003; White and Ross, 2011).

The upper diatreme commonly consists of volcanic tephra-filling bedded deposits. The occurrence of numerous fractures and normal faults at the upper diatreme margins testifies for syneruptive subsidence processes (White, 1991; Lorenz, 2003; Geshi *et al.*, 2011; White and Ross, 2011). The subsidence process within the craters is highlighted by the bowl-shape of the bedded deposits, better seen in the upper diatreme unit (e.g. Lorenz, 2003; Geshi *et al.*, 2011). When diatremes are relatively shallow, the upper diatreme may develop directly above the root zone: the bedding would dip less due to less subsidence (White and Ross, 2011).

The size of the crater is generally related to the size of the underlying diatreme and seems to be linked with the duration of the eruption: the shorter the eruptive activity, the smaller the crater and its associated diatreme (in terms of diameters and depths) (Lorenz, 1986).

The optimal pressure allowing phreatomagmatic explosions equals ~20-30 bars (e.g. Lorenz, 1986 and references therein; Vespermann and Schmincke, 2000). When an explosive burst (see section 2.1) occurs in the root zone, the water and the pyroclasts are expelled out of the diatreme: a zone of depression forms and the time-lapse before the zone will be again full of both water and rock materials triggers a cone of depression in the water level that pulls the explosion chamber slightly downward in order to reach again the required confining pressure (assuming a constant rate of water supply) (Figure 2.5)

(Lorenz, 1986). Therefore, this pressure-controlled downward penetration process is responsible for both the periodic growth of the explosive complex and the subsidence effects at the crater (e.g. Lorenz, 1986; White, 1991; Lorenz, 2000; Lorenz, 2003).

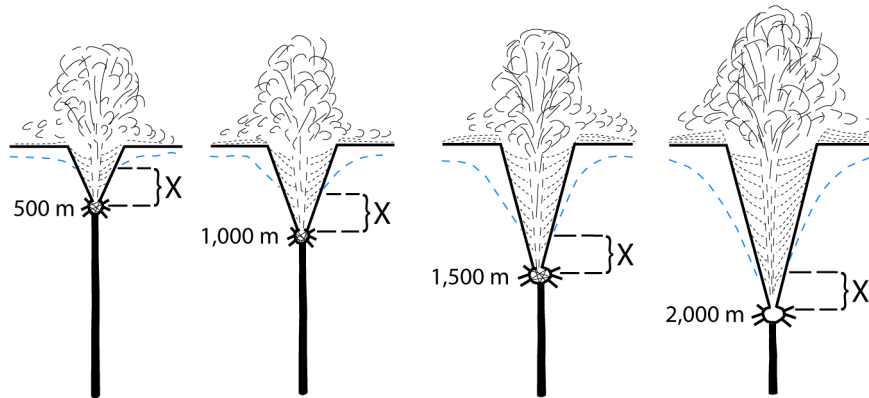


Figure 2.5 A diatreme forms by downward migration of the explosion chamber, located in the root zone, due to magma-water interactions, causing the formation of a cone of depression in the water level (blue dashed lines) (Lorenz, 1986).

When ample water is available, the explosion site is quickly replenished, preventing the formation of a cone of depression. Therefore, the downward development does not occur and collapsing and subsiding processes are negligible, leading to the absence of a diatreme and the formation of a tuff cone (Lorenz, 1986; Lorenz, 2003; Lorenz and Kurszlaukis, 2007). Tuff rings are commonly underlay by relatively shallow diatremes, testifying for relatively limited availability of water with respect to tuff cone formations: the lower diatreme is usually absent (Figure 2.6) (Lorenz, 1986; Lorenz, 2003).

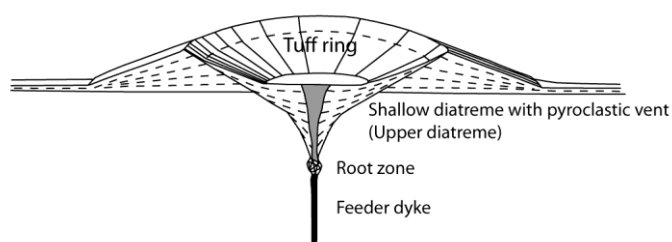


Figure 2.6 Schematic cross-section of a tuff ring volcano and its associated shallow diatreme. The dimensions (1 km in diameter and 150 m in height) are taken from the Hverfjall tuff ring in northern Iceland (Lorenz, 1986).

The shape and growth of diatremes are also largely influenced by the degree of consolidation of the country rock (Lorenz, 2003). Hard-rock environments (e.g. gneisses, granitoids, schists, basalts, sandstones, limestones) can be joint aquifers: many joints and faults intersecting the rock formations are good paths for channelling water to the system (Lorenz, 2003). When the successive explosion chambers form (Lorenz, 2000), the

downward migration process can give access to new sources of water by connecting joints and faults to the explosion chamber (Lorenz, 2003). Soft-rock environments are commonly more suitable for the growth of diatremes as they consist of highly permeable unconsolidated rock material (e.g. sands, pebble beds, unconsolidated breccias) (Lorenz, 2003). The slopes of the inner crater are usually less steep for explosive volcanoes in soft-rock environments rather than in hard-rock environments (Lorenz, 2003). Underground collapse and surface landslide can lead to irregular diatreme shapes in soft rock environments (e.g. Geshi *et al.*, 2011): the crater enlargement may be more “collapse-controlled” in soft-rock environment than “pressure-controlled”. If water-saturated sediments either overlie hard-rock formations (e.g. White, 1991) or are interbedded between hard-rock materials, a combination of both processes can occur during the formation of a maar-diatreme volcano (Lorenz, 2003).

2.2.4 Relation between explosive styles and basaltic volcanic structures

As discussed in section 2.1, when differentiating Taalian from Surtseyan eruptions, the former involve less water than the latter: relatively lower water/magma ratios leads to “drier” and more powerful phreatomagmatic eruptions. By connecting this concept to the structures of basaltic monogenetic volcanoes, tuff cones commonly form during Surtseyan eruptions (e.g. Kokelaar, 1986; Vespermann and Schmincke, 2000), as large amounts of water both prevent the development of diatremes and lead to the ejection of pyroclasts mainly by fallout transportation (Table 2.1). Tuff rings are usually produced by Taalian eruptions: the relatively less amount of water involved in the explosive process leads to the formation of a shallow diatreme and pyroclasts are mainly deposited by surges (e.g. Kokelaar, 1986; Vespermann and Schmincke, 2000) (Table 2.1). When limited water is available, the crater tends to become a maar (e.g. White and Ross, 2011).

Both the AD 871±2 Vatnaöldur and AD ~1477 Veiðivötn eruptions were first classified as Surtseyan due to the nature of the pyroclasts (Larsen, 1984). Later on, they were redefined as phreatoplinian because of both their high degree of fragmentation and large tephra dispersion recorded (Figure 2.1) (Thordarson and Larsen, 2007; Thordarson and Höskuldson, 2008; Larsen, 2005). The term Taalian has not been used in the classification of Icelandic eruptions.

2.3 Gravity investigations of the structure of explosive monogenetic volcanoes

As explained later, in section 3.1, gravity investigations highlight density contrasts in the subsurface: a denser body (with respect to the surrounding materials) generates a positive anomaly; whereas a less dense body produces a negative anomaly.

The structures of phreatomagmatic monogenetic volcanoes commonly display density contrasts: the diatreme-filling materials are usually composed of either relatively light tephra compared to the surrounding bedrock if the eruption was purely explosive, or of lava, denser than the surrounding bedrock, resulting from a late effusive stage. Therefore, gravity became an efficient tool for highlighting the bulk structure of monogenetic phreatomagmatic volcanoes. This geophysical method is used more and more for this purpose and may be coupled with other geophysical methods to obtain more precise data.

Two gravity studies have been selected for their pertinent similarities with the present study (see sections 4 and 5), in order to establish how reliable the gravity method is and what can be learned from gravity surveys about phreatomagmatism.

2.3.1 Efficiency and reliability of gravity investigations

Mrlina *et al.* (2007) proved the existence of a buried maar-diatreme volcano in the western Eger rift at the Czech/German border (Cheb basin, Central Europe), by using gravity investigations: a Bouguer map (map accuracy ± 0.06 mGal) spanned the area over the assumed buried maar-diatreme structure. 3-D forward modelling was performed along a cross-section. The forward modelling method consists of finding the shapes and densities of anomalous bodies to produce a calculated gravity signal that fits to the anomaly measured (e.g. Pedley *et al.*, 1993). 2.5-D models can be extended to 3-D models by allowing restricted lengths of the bodies in the direction perpendicular to the profile (i.e. strike direction) instead of keeping infinite lengths (e.g. Kearey *et al.*, 2002).

The model suggested the bulk shape of the now-called Mýtina maar volcano (Figure 2.7). The negative gravity anomaly indicated the presence of a relatively low dense body presenting a diatreme-shaped structure. An additional magnetic survey highlighted a relatively high magnetic susceptibility of this anomalous body, suggested to include magnetic minerals (Mrlina *et al.*, 2007). The materials filling the diatreme were therefore inferred to be composed of volcanic debris and relicts of country rocks; and a sediment-filled maar, expected to be overlain by alluvial sediments, was assumed to lie on the top of the diatreme structure (Mrlina *et al.*, 2007). It was also assumed that the density of the diatreme body increased with depth due to compaction (Mrlina *et al.*, 2007). No proof (e.g. drillholes, outcrops) could support the assumptions made regarding the nature and densities of the materials: the aim of the study was to reveal the approximate structure of the maar-diatreme volcano (Mrlina *et al.*, 2007).

As the gravity investigations were consistent with a maar-diatreme edifice, Mrlina *et al.* (2009) performed more detailed geophysical surveys (gravimetry, magnetometry, and electrical conductivity techniques) coupled with an exploratory drilling in the centre of the gravity anomaly (see section 3.1) in order to get a more precise 3-D forward model of the Mýtina maar, based on a new Bouguer map (map accuracy ± 0.10 mGal) (Figure 2.7). Both the complementary geophysical surveys and the exploratory drilling produced information about the internal maar-diatreme structure: the low density filling-diatreme materials consist of country rock breccias, mixed with volcanic products (e.g. bombs, lapilli and ash) and the maar is filled by low density sediments such as clay, gravel and sand (Mrlina *et al.*, 2009).

Comparison of the gravity models from both surveys (Figure 2.7) shows that the mean density values and body shapes are similar, even if the inner diatreme structure arrangements differ. The comparison of both studies reveals that the gravity method is an efficient and reliable tool for highlighting the bulk shape of maar-diatremes; but additional investigations (e.g. drillholes) are required to obtain more detailed information of the internal structures.

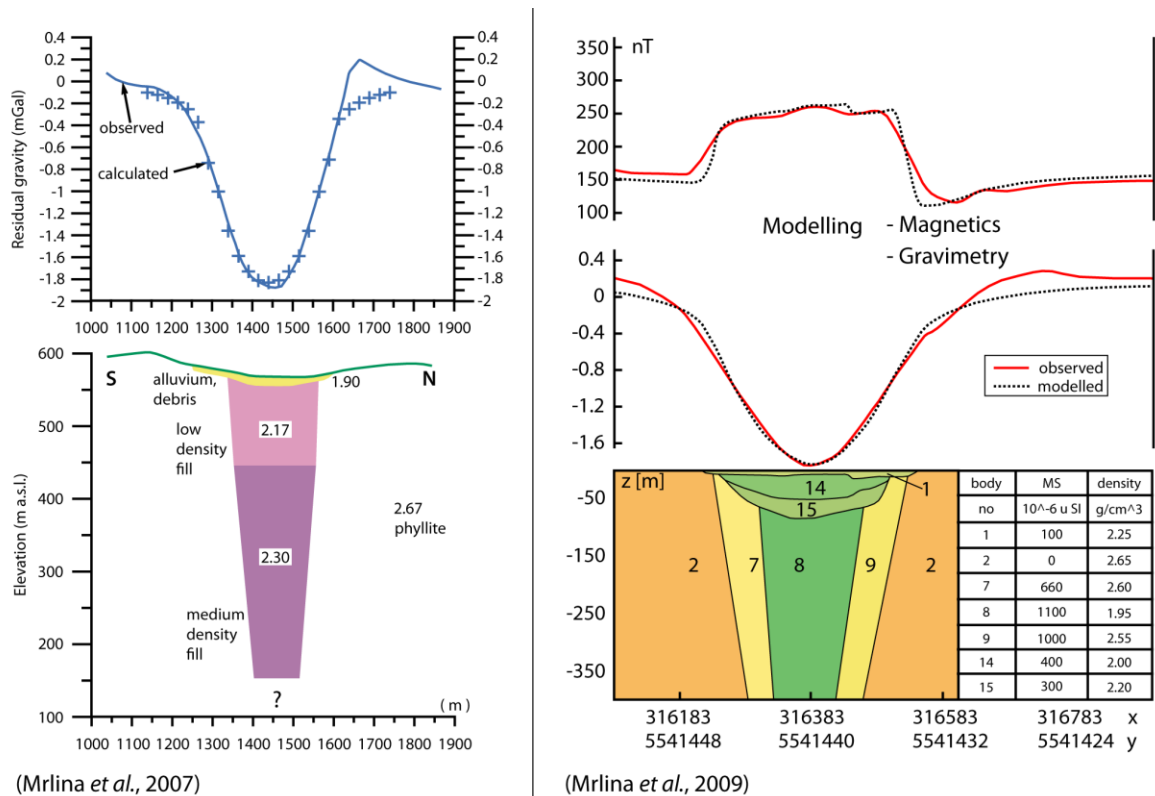


Figure 2.7 Cross-sections showing the structure of the Mýtina-maar volcano (Central Europe) inferred from 3-D modelling. The existence of the maar volcano was first emphasized from gravity, suggesting its bulk structure (left) (Mrlina et al., 2007). Later, the structure was more detailed from another survey coupling gravity and magnetic investigations (right) (Mrlina et al., 2009): 15 bodies were used but only seven are shown. Densities are in g/cm³ and the vertical scale is exaggerated.

2.3.2 Variations in eruptive styles highlighted from gravity

Cassidy *et al.* (2007) performed a detailed gravity survey across four monogenetic volcanoes that are part of the Auckland volcanic field (New Zealand) in order to model their subsurface structure and obtain new information about their magmatic evolution. Pukaki and Pukekiwiriki volcanoes are both tuff rings with a sediment-filled maar crater and lying in a soft-rock environment; Domain and Waitomokia volcanoes are tuff rings similar to the two former ones, but have a small scoria cone in the centre of their maar crater and lie in a hard-rock environment. Cassidy *et al.* (2007) created a Bouguer gravity map (map accuracy ± 0.10 mGal) covering each volcano and allowing 3-D forward modelling (Figure 2.8). A magnetic investigation was coupled to the gravity survey in order to highlight any possible magnetic volcanic materials from the sedimentary bedrock, and data from borehole drillings were used to control the relevance of the gravity results (Cassidy *et al.*, 2007). Pukaki gravity and magnetic data had been obtained in a previous study (Rout *et al.*, 1993) and were reinterpreted by Cassidy *et al.* (2007).

The gravity models reveal bowl-shaped crater structures that are consistent with phreatomagmatic activity (Cassidy *et al.*, 2007):

- At Pukaki, the eruption must have been purely explosive as the negative anomaly centred in the crater indicates the absence of any lava body in the conduit (all the magma must

have interacted explosively with the groundwater available) (Figure 2.8) (Cassidy *et al.*, 2007). The cessation of the eruption was interpreted as being due to a sufficient reduction of magma buoyancy because of stoppage of water-magma interaction and pressure release. The resulting potential intrusive solidified magma may either have a too small volume or may be at a depth beyond data resolution to generate any anomaly on the geophysical profiles (Cassidy *et al.*, 2007).

- At Pukekiwiriki, the phreatomagmatic eruption must have changed into effusive at the end: the model suggests magma ponding in the crater (Figure 2.8). Groundwater supply must have been exhausted before the eruption stopped (Cassidy *et al.*, 2007).

- At Domain and Waitomokia, magma supply and supply of available water must have been larger than at Pukaki and Pukekiwiriki as the bedrock was excavated to greater depths (Figure 2.8) (Cassidy *et al.*, 2007). The occurrence of a lava fill is probably due to a lack of groundwater availability at the end of the eruption (Cassidy *et al.*, 2007).

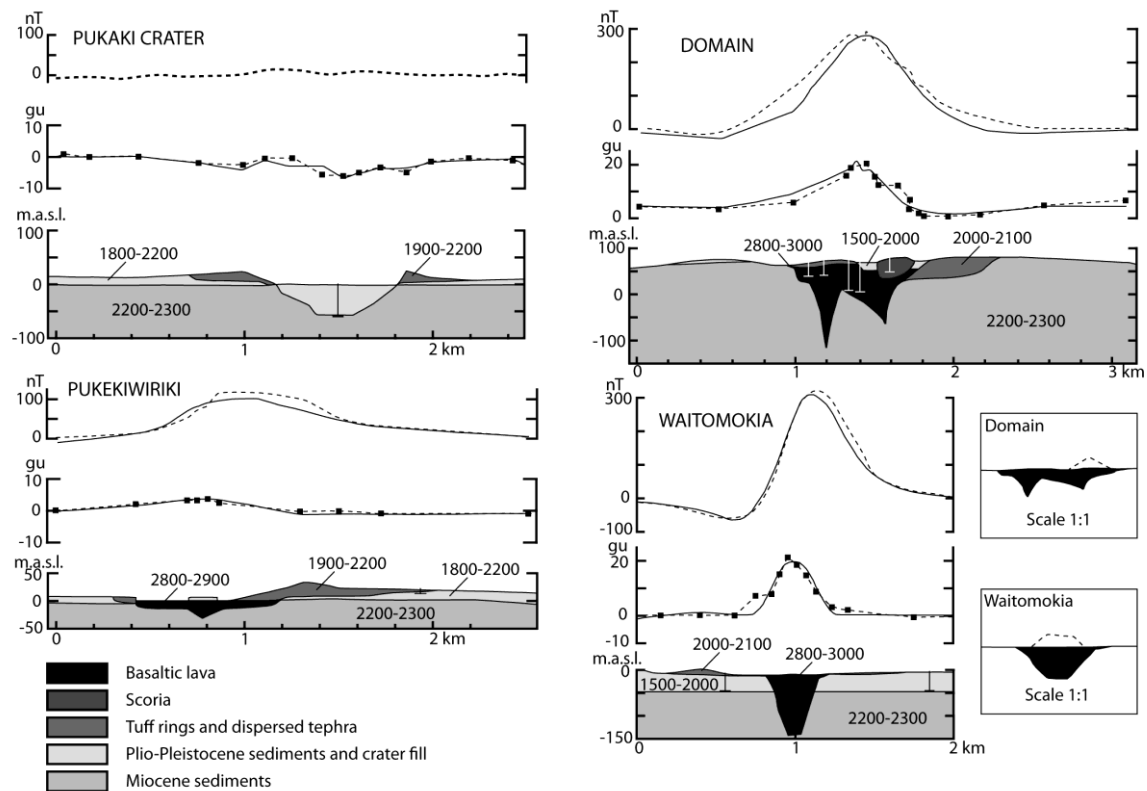


Figure 2.8 Cross-sections through 3-D models highlighting the bulk structures of four tuff ring volcanoes in the Auckland Volcanic Field (New Zealand), from both gravity and magnetic investigations (Cassidy *et al.*, 2007).

2.4 Choice of the study area

The AD 871 \pm 2 Vatnaöldur and AD ~1477 Veiðivötn fissure eruptions are known to have been predominantly phreatomagmatic leading to the formation of aligned tuff rings, tuff cones and maar volcanoes, forming crater rows (see section 1.4).

The first interesting comparison between the two events is that the AD 871±2 Vatnaöldur eruption has been interpreted as being almost purely explosive; whereas the AD ~1477 Veiðivötn eruption became effusive at the end, filling the bottom of the craters with lava.

In order to confirm this assumption made from geological mapping, gravity appeared to be a suitable method as the assumed Vatnaöldur tephra-filled conduits were expected to be less dense than the surrounding bedrock, expected to generate a gravity low; whereas the Veiðivötn dense lava-filled conduits were expected to generate a positive gravity anomaly.

3 Gravity theory

Gravity is a passive method of geophysics that contributed to a better understanding of the Earth's shape and its rotational properties (Fowler, 1990). This method can also give information about the Earth's structure at smaller scales as it can be used to detect lateral density variations in the subsurface (e.g. Gudmundsson and Högnadóttir, 2007). This chapter presents an overview of gravity theory, from the fundamental principles to the computation of gravity anomalies, including the corrections of the effects of some physical parameters that influence gravity measurements.

3.1 Basic principles

The force of gravity is determined by Newton's gravitational law, sometimes called the "Inverse square relationship" (Equation 3.1) that expresses the force of gravitational attraction between two point masses (Fowler, 1990; Sleep and Fujita, 1997; Kearey *et al.*, 2002).

$$F = \frac{G M_1 M_2}{r^2} \quad \text{Equation 3.1}$$

F: Force of attraction between the masses (m kg s^{-2})
G: Gravitational constant ($G = 6.673 \cdot 10^{-11} \text{ m}^3 \text{ kg}^{-1} \text{ s}^{-2}$)
 M_1 and M_2 : Point masses (kg)
r: Distance between the masses (m)

The gravity g (or gravitational acceleration, a force per unit mass) is obtained from Equation 3.1, by dividing the force of attraction, F , by the mass of the attracted body (M_1). (Equation 3.2) (Fowler, 1990; Sleep and Fujita, 1997; Kearey *et al.*, 2002).

$$g = \frac{F}{M_1} = \frac{G M_2}{r^2} \quad \text{Equation 3.2}$$

g : Gravitational acceleration, or Gravity (m s^{-2})
F: Force of attraction between the masses (m kg s^{-2})
 M_1 and M_2 : Point masses (kg)
G: Gravitational constant ($G = 6.673 \cdot 10^{-11} \text{ m}^3 \text{ kg}^{-1} \text{ s}^{-2}$)
r: Distance between the masses (m)

Equation 3.2 gives a constant value of gravity at the surface of a homogeneous, strictly spherical and non-rotating body. In reality, gravity is not constant at every point of the Earth's surface, due to its ellipsoidal shape, irregular surface, heterogeneous mass distribution and rotating behaviour (Fowler, 1990; Kearey *et al.*, 2002).

For local studies, the minute variations are expressed in milligal (mGal - c.g.s.) or gravity unit (gu - SI units) (Sleep and Fujita, 1997; Kearey *et al.*, 2002): $1 \text{ mGal} = 10 \text{ gu} = 10^{-5} \text{ m s}^{-2}$.

In the present study, the studied parameter is the mass distribution in the shallow subsurface, causing density contrasts: an anomalously dense or light body, with respect to

the surroundings, will generate gravity variations, called gravity anomalies, of which magnitude and extent depend on the size and density of the body (Figure 3.1).

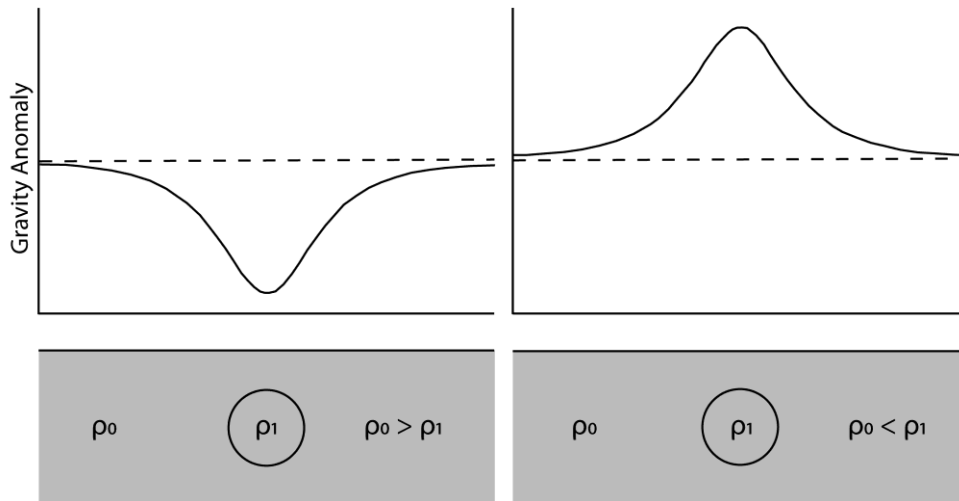


Figure 3.1 The gravity anomaly can be negative (left) or positive (right) and is influenced by the density contrast caused by an anomalous body of density ρ_1 with respect to the surrounding materials having a bulk density ρ_0 (Vilhjálmsdóttir, 2006).

From a mathematical point of view, density anomalies in the subsurface cause the vector of gravitational attraction (\mathbf{g}) to deviate in both magnitude and direction, this physical phenomenon is called the “deflection of the vertical” (Figure 3.2) (Sleep and Fujita, 1997).

Gravimeters (or gravity meters) are highly sensitive instruments used to measure the gravity anomalies at the Earth’s surface. A simplified description is that of a spring in equilibrium, carrying a mass (Sleep and Fujita, 1997; Kearey *et al.*, 2002). An anomalous body in the subsurface will cause a change in the measured spring length (Sleep and Fujita, 1997; Kearey *et al.*, 2002). The deflection of the vertical is usually extremely small; therefore, the gravity anomaly is equal to Δg , the vertical component of \mathbf{g}_a , the gravitational attraction of the anomalous body (Figure 3.2) (Sleep and Fujita, 1997).

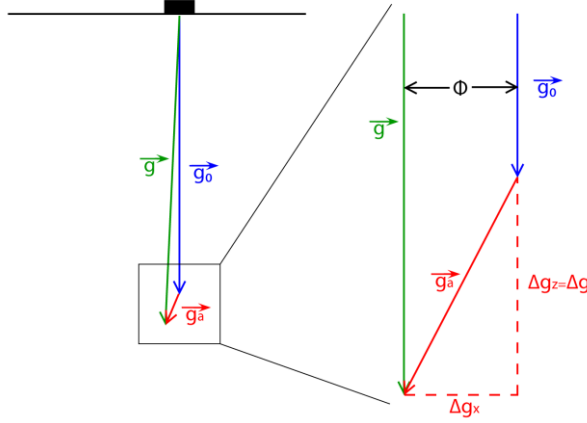


Figure 3.2 Deflection of the vertical of an angle Φ where \mathbf{g} is the total acceleration of gravity in the presence of an anomalous body, which causes a total gravity anomaly (\mathbf{g}_a), and \mathbf{g}_0 would be the gravitational acceleration in the absence of the anomalous body (Sleep and Fujita, 1997).

The gravity anomaly can be expressed from Equation 3.1 and Equation 3.2 considering the mass held by the spring in the gravimeter as M_1 , and the anomalous body as M_2 (Equation 3.3) (Fowler, 1990; Sleep and Fujita, 1997; Kearey *et al.*, 2002). Note that the anomalous body is assumed to be homogeneous, spherical, and non-rotating.

$$\Delta g = |\vec{g}_a| \cos\beta = \frac{G M_2}{r^2} \cos\beta \leftrightarrow \Delta g = \frac{G M_2 z}{r^3} \quad \text{Equation 3.3}$$

Δg : Gravity anomaly (m s^{-2})

\mathbf{g}_a : Gravity anomaly vector

β : Angle between the \mathbf{g}_a and \mathbf{g}_0 (Figure 3.2)

G : Gravitational constant ($G = 6.673 \cdot 10^{-11} \text{ m}^3 \text{ kg}^{-1} \text{ s}^{-2}$)

M_2 : Mass of the anomalous body (kg)

r : Distance between the anomalous body and the gravimeter (m)

z : Vertical depth to the anomalous body (m)

3.2 Gravity reductions

The aim of the present gravity survey was to highlight the structure of anomalously high or low density bodies, lying in the uppermost few hundred meters of the crust. Therefore, all the effects other than arising from the mass distribution have to be removed (i.e. the Earth's ellipsoid shape, its rotating behaviour, its irregular surface).

Note that the term “reduction”, often used in gravity, means “reduction to zero” as the gravity effects of the parameters are entirely removed (or corrected) from the “observed” gravity values. The values measured with the gravimeters are usually called “readings”. Their conversion in milligals using a calibration table (LaCoste & Romberg, Inc., 1979), gives gravity values relative to a reference values at a base station of known absolute value.

3.2.1 Tidal correction

The periodic tidal effect is due to both the rotation of the Earth around its own axis and the rotation of the Earth-Moon system (and Earth-Sun system) around its own centre of mass

(e.g. Sleep and Fujita, 1997; Kearey *et al.*, 2002). Gravimeters are very sensitive and precise enough to detect those gravity variations, which therefore influence the readings (Sleep and Fujita, 1997; Kearey *et al.*, 2002). The tidal effect is the first parameter that needs to be corrected, and it is directly applied to the reading gravity values after they have been converted to milligals. The Longman algorithm (Longman, 1959) is an algebraic method that calculates this undesirable effect and allows for its removal from the data.

3.2.2 Drift correction

The reading value on the gravimeter is related to the extension of the spring due to the gravitational attraction of the mass, held by the spring, towards the anomalous body (Figure 3.2) (Sleep and Fujita, 1997). Some minute changes, due to the imperfect elasticity of the spring, are referred to as the instrumental drift. In order to reduce this effect, readings are performed at regular intervals at a base station, where the absolute gravity value is known (Sleep and Fujita, 1997; Kearey *et al.*, 2002). A linear trend in drift is assumed in between the base-station readings. An absolute, observed gravity value (g_{obs}) is obtained for each survey point by calculating the difference in gravity relative to the base station.

3.2.3 Latitude correction

The gravity value at the Earth's surface ($\sim 9.81 \text{ m s}^{-2}$ on average) depends on the distance to the centre of the Earth. The relatively gradual $\sim 21\text{-km}$ -change in the Earth's radius, from the poles to the equator induces some gravity variations along the latitudes. In addition, the centrifugal effect arising from the rotation of the Earth lowers the gravity values (Fowler, 1990). The combined effect is a reduction from $\sim 9.83 \text{ m s}^{-2}$ at the poles to $\sim 9.78 \text{ m s}^{-2}$ at the equator (Sleep and Fujita, 1997; Kearey *et al.*, 2002). The International Gravity Formula 1980 (Equation 3.4) (International Association of Geodesy, 1980) reduces those two effects by considering the Earth as a symmetric spheroid model called "reference ellipsoid" (e.g. Fowler, 1990). For each survey point, the reduction is applied by subtracting the latitude correction $g_n(\lambda)$ from the observed value g_{obs} in order to only consider the gravity between the reference datum and the survey points (Fowler, 1990; Kearey *et al.*, 2002).

$$g_n(\lambda) = g_0 (1 + \alpha \sin^2 \lambda + \beta \sin^4 \lambda + \gamma \sin^6 \lambda) \quad \text{Equation 3.4}$$

$g_n(\lambda)$: Normal gravity at the latitude λ (mGal)
 g_0 : Value of gravity at the equator ($g_0 = 978031.85 \text{ mGal}$)
 $\alpha = 5.278895 \cdot 10^{-3}$
 $\beta = 2.3462 \cdot 10^{-5}$
 $\gamma = 1.262 \cdot 10^{-7}$

3.2.4 Free air correction

The irregularities of the Earth's surface induce changes in the distance to the centre of the Earth's mass that lead to minute gravity variations. This elevation effect is reduced by adjusting the gravity values to a same reference datum (Equation 3.5) (Fowler, 1990; Sleep and Fujita, 1997; Kearey *et al.*, 2002), the geoid, being the mean sea level and its continuation on land. For each survey point, the reduction is applied by adding the free-air correction, FAC, to the observed gravity value g_{obs} , as the elevation of the survey point

above sea level lowers the gravity anomaly due to increase in the distance to the centre of the Earth.

$$FAC = \frac{G M_e}{r_e^2} - \frac{G M_e}{(r_e + h)^2} \leftrightarrow FAC = 0.3086 h \quad \text{Equation 3.5}$$

FAC: Free-air correction (mGal)

G: Gravitational constant ($G = 6.673 \cdot 10^{-11} \text{ m}^3 \text{ kg}^{-1} \text{ s}^{-2}$)

M_e : Mass of the Earth (kg)

r_e : Mean radius of the Earth (m)

h: Height of the survey point (m a.s.l.)

3.2.5 Correction for topography: a combined Bouguer and terrain correction

Two different approaches are commonly used to remove the effects of the topography from the observed gravity values. (1) The Bouguer plate method removes the gravitational effect of the rock between the survey point and sea-level from the observed gravity anomaly g_{obs} , considering an infinite horizontal plate of thickness that is equal to the elevation of the survey point above sea level (Equation 3.6). When using this approach, terrain corrections need to be applied, removing effects that arise because the topography deviates considerably from a flat surface (e.g. Kearey *et al.*, 2002) (2) The total terrain correction takes into account both the Bouguer and the terrain corrections as the gravitational effect of the mass above sea level is calculated by integrating a digital elevation model (DEM) that represents the topography around each survey point (Equation 3.7). In the present study, the total terrain correction method was chosen, using a set of DEMs, which cover large enough area that extends at least out to 50 km from each survey point.

$$BC_{pl} = 2\pi G \rho h \quad \text{Equation 3.6}$$

BC_{pl} : Bouguer correction (Bouguer plate method) ($\text{m s}^{-2} = 10^5 \text{ mGal}$)

G: Gravitational constant ($G = 6.673 \cdot 10^{-11} \text{ m}^3 \text{ kg}^{-1} \text{ s}^{-2}$)

ρ : Bulk density of the Bouguer plate (kg m^{-3})

h: Height of the survey point (m a.s.l.)

$$BC_{tc} = G \rho \iiint_V \frac{z \, dx \, dy \, dz}{r^3} \quad \text{Equation 3.7}$$

BC_{tc} : Total terrain correction ($\text{m s}^{-2} = 10^5 \text{ mGal}$)

G: Gravitational constant ($G = 6.673 \cdot 10^{-11} \text{ m}^3 \text{ kg}^{-1} \text{ s}^{-2}$)

ρ : Reduction density, i.e. bulk density of the Bouguer plate (kg m^{-3})

z: Elevation (m a.s.l.)

dx=dy: side length of each prism (m)

dz: height of each prism (m)

$r = (x^2 + y^2 + z^2)^{1/2}$: Distance to the survey point (m)

The Hammer graticule splits the area around each survey point into segments of a cylinder with an inner and outer radius. An analytical method for terrain corrections exists to calculate the gravitational effect of each cylinder segment, where the height of the segment is the difference in survey point height and height of the topography within the segment. This method is usually carried out by using tables for the corrections values for segment and several elevation differences (Fowler, 1990; Kearey *et al.*, 2002). The three Hammer zones closest to the survey point, known as A, B and C, span the radial areas from 0 to 2

m, 2 to 16.6 m and 16.6 to 53.3 m, respectively (Milsom, 2003). The location of each survey point is selected in such a way that zone A is flat and no corrections are therefore applied for that zone. The elevation differences within the segments of zones B and C are usually estimated by eye during the fieldwork (Milsom, 2003).

3.3 Free-air and Bouguer anomalies

Two main types of gravity anomalies can be calculated from the reductions, depending mostly on the topographic conditions.

The free-air anomaly (g_{FA}) is obtained by correcting for both the latitude and elevation effects from the observed gravity values (g_{obs}) (Equation 3.8) (Sleep and Fujita, 1997; Kearey *et al.*, 2002). This gravity anomaly does not take the reduction for the mass of topography into account (see section 3.2.5). At sea, the absence of topography variations enables the use of this type of gravity anomaly.

$$g_{FA} = g_{obs} - g_n + 0.3086 h \quad \text{Equation 3.8}$$

g_{FA} : Free-air anomaly (mGal)

g_{obs} : Observed gravity value obtained after the tidal and drift corrections (mGal) (see sections 3.2.1 and 3.2.2)

g_n : Normal gravity at the latitude λ (mGal) (see section 3.2.3)

h : Height of the survey point (m a.s.l.)

The Complete Bouguer anomaly (g_{BA}) takes all the reductions into account (Sleep and Fujita, 1997; Kearey *et al.*, 2002) and therefore, gives the gravity values at the survey points as if they had been measured on a homogeneous horizontal infinite slab of crust, at the same latitude (Sleep and Fujita, 1997; Kearey *et al.*, 2002). Equation 3.9 refers to the formula using the total terrain correction method for correcting for the topography (see section 3.2.5). The Complete Bouguer gravity anomaly is preferably used on land.

$$g_{BA} = g_{FA} - G\rho \iiint_V \frac{z \, dx \, dy \, dz}{r^3} \quad \text{Equation 3.9}$$

g_{BA} : Complete Bouguer anomaly (mGal)

g_{FA} : Free-air anomaly (mGal)

G : Gravitational constant ($G = 6.673 \cdot 10^{-11} \, \text{m}^3 \, \text{kg}^{-1} \, \text{s}^{-2}$)

ρ : Bulk density of mass of the topography = Reduction density ($\text{kg} \, \text{m}^{-3}$)

TC: Terrain corrections

Refer to section 3.2.5 and Equation 3.7 for the term with the integral

After the corrections and the choice of the density value that best represents the mean density of the topography, the Bouguer anomaly should highlight the effect of subsurface lateral relative density variations, highs over high density bodies and lows over low density bodies (Figure 3.1). Note that uncertainties in all the measured values contribute to uncertainties in the the final Bouguer anomalies (see further, section 4.3.5).

For local studies, Bouguer maps and gravity profiles are the two most common ways of representing the residual gravity anomaly variations over an area (e.g. Gudmundsson and Högnadóttir, 2007). The term “residual” means that the regional gravity effects have been removed graphically from the signal of the Complete Bouguer anomaly obtained (e.g. Kearey *et al.*, 2002). For the present study, profiling was chosen as a first approach to highlight the bulk structure of six phreatomagmatic edifices.

4 Gravity survey, data and methods

In the present study, gravity was surveyed across the Vatnaöldur and the Veiðivötn crater rows, belonging to the Veiðivötn fissure swarm (see section 1). In total, 65 of the survey points measured were considered. Four profiles cross the Vatnaöldur fissure (Va-1, Va-2, Va-3 and Va-4 from SW to NE) and two across the Veiðivötn fissure (Ve-1 and Ve-2 from SW to NE) (Figure 4.1).

Va-1 and Va-2 on one hand and Va-3 and Va-4 on the other hand crosses adjacent craters belonging to Vatnaöldur Fremri and Vatnaöldur Innri, respectively (Figures 4.1 and 1.3). The Ve-1 profile crosses a crater from Veiðivatnagígar whereas the Ve-2 profile crosses a crater belonging to Fossvatnagígar.

Both gravity data acquisition and gravity data processing were performed following the same methods already carried out in previous studies in Iceland (e.g. Gudmundsson and Milsom, 1997; Gudmundsson and Högnadóttir, 2001; Gudmundsson *et al.*, 2002; Vilhjálmsson, 2006; Gudmundsson and Högnadóttir, 2007; Ágústsdóttir, 2009).

This chapter summarizes the methods used in the study. Data acquisition is explained before giving details about digital elevation models and data processing; the choices of densities are then discussed; and finally, the accuracy of the Bouguer anomalies is calculated.

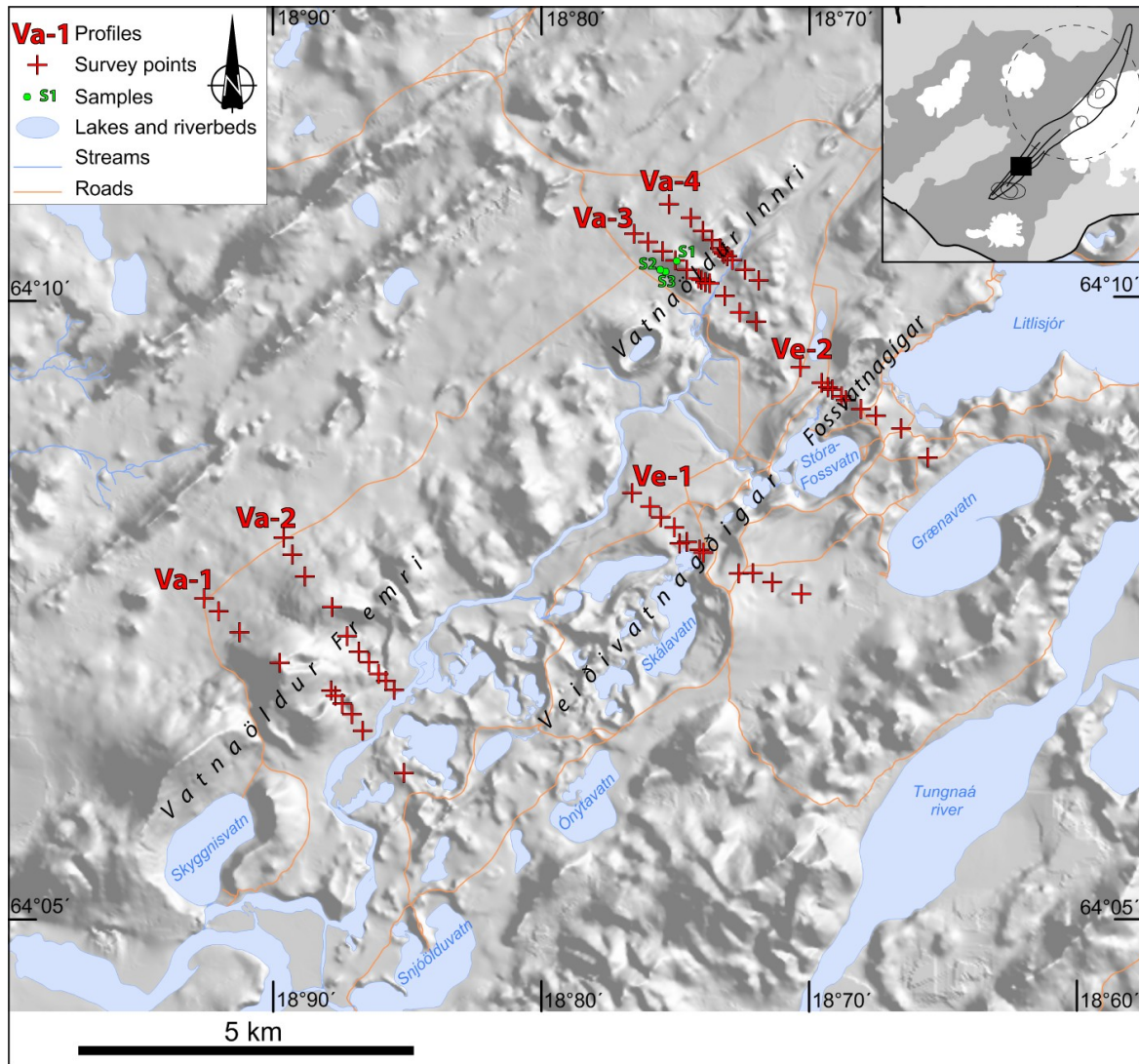


Figure 4.1 Area of study in the Veidivötn area, South Central Iceland. The location of the area (top right corner) is given in Figure 1.2.

4.1 Data acquisition

The survey was conducted by Jeanne M. Ginioux and Thorbjörg Ágústsdóttir, during six days, in July 2012. Most of the survey points were reached on foot, but several could be reached by car. The LaCoste&Romberg (G445) gravimeter was used for gravity measurements (LaCoste & Romberg, Inc., 1979) and a kinematic Trimble GPS 5700 enabled the measurement of the elevations (Figure 4.2).

The gravimeter is highly sensitive to any force acting on it (e.g wind, passing car, instability on ash ground). In order to reduce the error of the readings, wind forces were decreased by sheltering the gravimeter and a wooden plank was used in addition to the conventional disc, to have the instrument more stable on the loose tephra material (Figure 4.2).



Figure 4.2 Picture taken during the fieldtrip, showing all the equipment required for precise gravity and elevation measurements: (1) the LaCoste&Romberg (G445) gravimeter; (2) a disk to level precisely the gravimeter; (3) a wooden plank to help stabilising the disk; (4) a solid box for carrying the gravimeter, containing its battery; and a kinematic GPS Trimble 5700 composed of the receiver (in the back pack) (5), the command of control (6) and the GPS antenna (7).

Three GPS measurements were usually carried out at each survey point. The duration of the records was 3 minutes on average except on the Va-2 profile, where the records lasted only for 1.5 minutes at each survey point. However, the accuracy of the survey points was still reasonable. The measurements were either performed having the GPS back pack on the ground (antenna height of 1.13 m) for the survey points that could only be reached by walking; where the survey points could be reached by car, the antenna was fixed on the top of the car (antenna height of 2.14 m). Variations from these heights of a few centimetres were taken into account, for the survey points that were a little lower or higher with respect to the ground surface (Appendix A). The survey points on the Ve-1 profile were difficult to measure along a straight line because of fishing huts.

4.2 Digital Elevation Models

Digital elevation models (DEMs) were generated from a dense set of digitized contour lines of maps, using the method of kriging. The Golden Software program Surfer 10 was

used for the map generation (see section 3.2.5). Three DEMs were generated using both different data sources and different grid spacing.

The most precise DEM spans the entire area of study, with a grid spacing of 25 m (Figure 4.1). The X-Y-Z data obtained from an accurate map have a resolution of 5-10 m close to the gravity profiles and 10-20 m further away. The close surroundings of the profiles have been digitized in ArcGis 10, using 5-m-contour topographic maps (1:20,000) (OS, 1959a,b,c; OS, 1960; OS, 1961a,b) whereas data digitized by Rósa Ólafsdóttir at the University of Iceland were used for the furthest zones (LMÍ, 2011). The water-level of the rivers and lakes has been estimated from the final digitized topography.

A second DEM, calculated with a grid spacing of 200 m, extends over a region of $\sim 10 \times 10$ km out of the survey area and is centred on it. The X-Y-Z data were obtained from a digital database of the National Land Survey of Iceland (LMÍ, 2010).

The third and larger DEM spans a region of $\sim 100 \times 100$ km further away from the second DEM, centred on the survey area, with a grid spacing of 1000 m. The DEM is a part of a DEM that had already been created by Gudmundsson and Högnadóttir (2001) using 1:50,000 maps of the Iceland Geodetic Survey. Outside of the larger DEM, the topography was assumed to be flat in order to minimize the topography effect (see section 3.2.5) (Gudmundsson and Högnadóttir, 2001). This assumption is valid because of the relatively low relief of Iceland.

4.3 Data processing

In order to obtain the Complete Bouguer gravity anomalies (see section 3.3) for each profile, data processing was performed in three steps (Gudmundsson and Högnadóttir, 2001):

- Acquisition of precise X-Y-Z coordinates for each survey point from GPS measurements;
- Reduction of the tidal gravity effect at each survey point and computation of the free-air anomalies;
- Computation of the Complete Bouguer anomalies for each survey point.

4.3.1 Survey point coordinates

Finnur Pálsson (University of Iceland) processed the GPS data, using three base stations: HOFN (Sopac, 2013), JOKU (e.g. Jónsson *et al.*, 1997) and ISAK (IMO, 2005). The GPS solutions having the smallest vertical errors, Δz_{gps} , were selected for each survey point. When the smallest Δz_{gps} was repeated for several measurements at a same survey point, the average of the corresponding X-Y-Z coordinates was calculated.

About 89 % of the Δz_{gps} values do not exceed 0.1 m (Figure 4.3) but the other 11% have a relatively sparse distribution between 0.1 m and 0.6 m that influences the mean Δz_{gps} of 0.07 m. For better confidence, 95% of the values were considered for estimating the vertical error in GPS measurements. Therefore, the maximum uncertainty, ΔZ_{gps} , in GPS

vertical coordinates equals 0.3 m. This error induces an uncertainty of 0.06 mGal (Equations 3.5 and 3.6).

One point on the Ve-2 profile (the 6th from the NW end) was not taken into account in the total vertical error calculation because it does not have accurate GPS measurements. However, because of its location within the crater and as the topography does not look abnormal at this location, the survey point was not removed for the computation processes.

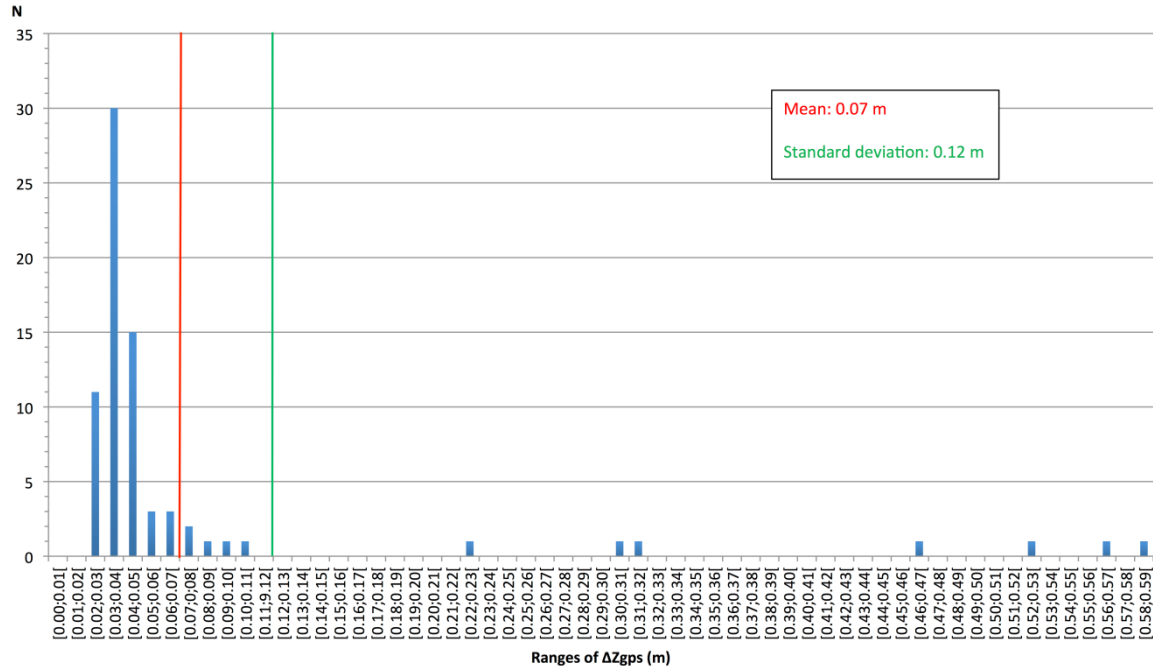


Figure 4.3 Chart of the distribution of the vertical errors (Δz_{gps}) from the GPS measurements

4.3.2 Reading corrections and free-air anomalies

A Fortran routine (flod.exe) from the National Energy Authority (Orkustofnun), based on the Longman algorithm (Longman, 1959) was used to calculate the tidal corrections (see section 3.2.1) for every hour and day of the survey period. Another Fortran routine (freeair.exe) computed the free-air anomalies by reducing the drift, latitude and free-air effects (see sections 3.2.2, 3.2.3 and 3.3) and including the tidal corrections, previously calculated (Gudmundsson and Högnadóttir, 2001).

To determine the drift corrections, the closest base station used was at Jökulhleimar (JH) (Table 4.1): it is not an official base station but its absolute value has been calculated by repeated ties with the HALD base station (Gudmundsson and Högnadóttir, 2001). As it was at ~30 km away from the area of study (~1:00-1:30 of driving), some survey points were measured several times during the day to ensure that a jump in the drift would not go undetected. No such jumps were observed.

Table 4.1 Information about the gravity base station JH (at Jökulhleimar) used for the data processing.

Latitude (°N)	Longitude (°W)	h (m a.s.l.)	g_{absolute} (mGal)
64.3099	18.2383	672.7	982093.64±0.14

4.3.3 Complete Bouguer anomalies

In order to compute the complete Bouguer anomalies, a Fortran routine (ttc25.exe) was developed by David Harrison (University College of London) in 1989, and improved by Magnús Tumi Gudmundsson (University of Iceland) in 1997 (Gudmundsson and Högnadóttir, 2001; Vilhjálmsson, 2006). The correction for topography was integrated over a square of 100 km-side length centred on the survey points, using the three DEMs in the Fortran routine (see section 4.2) (Figure 4.4) (Gudmundsson and Högnadóttir, 2001).

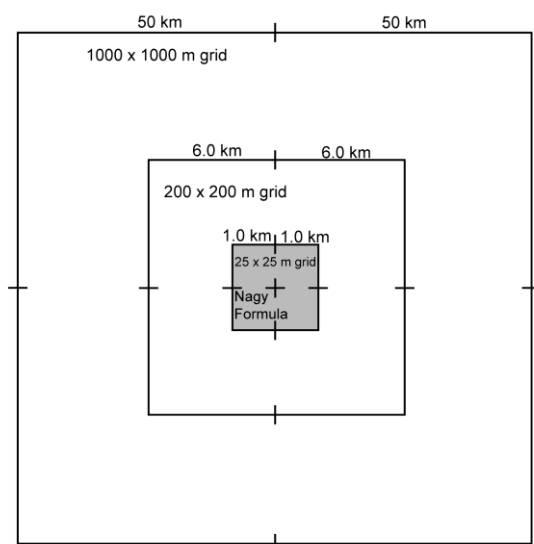


Figure 4.4 The mass effect of the topography is integrated over a square of 100 km-side-length, centred on each survey point, using three DEMs of different node spacing values: 25 m, 200 m and 1000 m, from the smallest to the biggest square, respectively) (Gudmundsson and Högnadóttir, 2001).

On a 2 by 2 km square centre around each survey point, the Fortran program uses the Nagy formula (Nagy, 1966), which is an analytical solution for Equation 3.7 for a vertical single prism. The whole bedrock topography is integrated over the 2 by 2 km square by summing the effect of all the prisms within the square (Figure 4.5 and Equation 4.1) (Gudmundsson and Högnadóttir, 2001; Vilhjálmsson, 2006; Ágústssdóttir, 2009). The DEM used as input for the Nagy calculation is the precise DEM of 25 m grid spacing that spans the area of study (see section 4.2).

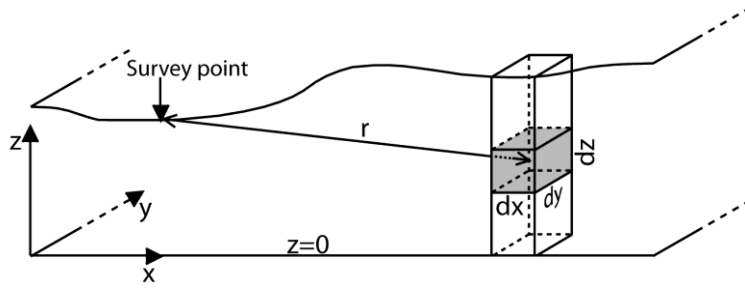


Figure 4.5 Graphical representation of the integration of the effect of the bedrock topography over the 25 m grid spacing DEM, using the Nagy formula: the volume of the Bouguer plate is divided into right rectangular prisms (Vilhjálmsón, 2006).

$$\delta_g = G\rho \left[\int_{x_1}^{x_2} \int_{y_1}^{y_2} \left[x \ln(y+r) + y \ln(x+r) - z \arcsin \left(\frac{z^2 + y^2 + yr}{(y+r) \sqrt{(y^2 + z^2)}} \right) \right] dx dy \right]_{z_1}^{z_2} \quad \text{Equation 4.1}$$

δ_g : Correction for topography of a prism with height $z_2 - z_1$, and side lengths of $x_2 - x_1$ and $y_2 - y_1$ ($\text{m s}^{-2} = 10^5 \text{ mGal}$)

G: Gravitational constant ($G = 6.673 \cdot 10^{-11} \text{ m}^3 \text{ kg}^{-1} \text{ s}^{-2}$)

ρ : Reduction density (kg m^{-3})

z: Elevation (m a.s.l.)

$dx=dy$: Side length of each prism (m)

dz : Thickness of element (m)

$r = (x^2 + y^2 + z^2)^{1/2}$: Distance to the survey point (m)

Outside of the smallest (2 by 2 km) square a more simple formula (Equation 4.2) is used to facilitate the integration of topography over both the 200 m grid spacing and the 1000 grid spacing DEMs (see section 4.2) (Gudmundsson and Högnadóttir, 2001; Vilhjálmsón, 2006). The terrain corrections were evaluated by eye during the fieldtrip for the Hammer zones A, B and C (see section 3.2.5).

$$\delta_g = G\rho \left(\frac{1}{r_1} - \frac{1}{r_2} \right) dx dy \quad \text{Equation 4.2}$$

δ_g : Approximate correction for topography using a line mass approximation for prisms ($\text{m s}^{-2} = 10^5 \text{ mGal}$)

G: Gravitational constant ($G = 6.673 \cdot 10^{-11} \text{ m}^3 \text{ kg}^{-1} \text{ s}^{-2}$)

ρ : Reduction density (kg m^{-3})

$dx = dy$: Grid spacing, respectively in x and y directions (m)

r_1 : Distance from the survey point to the top of the prism (m)

r_2 : Distance from the survey point to the bottom of the prism (m)

4.3.4 Densities

4.3.4.1 Bedrock density

A single density value, called bedrock density or reduction density (e.g. Gudmundsson and Högnadóttir, 2007), is used in the calculation of the Bouguer anomalies, considering the bedrock as homogeneous. In forward modelling, the densities of the anomalous bodies are obtained from the density contrasts with respect to this reduction density. To facilitate the comprehension of the results, it is best to choose a same reduction density for all the profiles.

The geological cross-section through both the Vatnaöldur and Veiðivötn fissures (Figure 4.6) indicates that the uppermost ~100 m of the crust consist of young volcanic rocks. Beneath ~100 m from the surface, some areas are either known to be composed of Pleistocene hyaloclastite formations (e.g. Vatnaöldumóberg beneath Vatnaöldur) or the geological formations could not be identified with certainty (e.g. beneath Veiðivötn) (Vilmundardóttir *et al.*, 1988). On a larger scale, the bedrock is known to be mainly composed of some Upper-Pleistocene subglacial formations (see section 1.1), sometimes lying under fresh Holocene lava flows (Figure 4.7) (e.g. Vilmundardóttir *et al.*, 1988; Jakobsson *et al.*, 2008; Thordarson and Höskuldsson, 2008). Those observations show that the bedrock in the area of study seems to be characteristic for an active rift zone (see section 1.1). Therefore, it should have properties similar to the seismic layer 0 defined as the uppermost crust within the volcanic zones (Pálmason, 1971; Flóvenz, 1980; Flóvenz and Gunnarson, 1991), and having an estimated bulk density ranging from 2100 to 2500 kg m⁻³.

The main third geological unit of the area, in addition to lava flows and hyaloclastites, is the tephra unit, making up the crater rims. As the aim of the study is to highlight dense lava bodies and tephra bodies of relatively low densities, a medium density, close to the density of hyaloclastites (Table 4.2), would be the most appropriate for defining the bedrock.

Choosing a reduction density of 2300 kg m⁻³ seems to be a good compromise as it is the mean value of the seismic layer 0 and remains coherent with a water-saturated bedrock mainly composed of hyaloclastite formations. Gudmundsson and Högnadóttir (2007) chose the same value for a gravity survey slightly further to the Northwest, in an area including the middle part of the Bárðarbunga-Veiðivötn system.

Table 4.2 Density of Quaternary and Holocene rocks in Iceland (Gudmundsson and Milsom, 1997 and references therein).

Rock samples	Dry density (kg m⁻³)	Wet density (kg m⁻³)
Hyaloclastites	1600	2100
Basaltic pillow lavas	2250	2450
Basaltic lava flows	2650	2780
Tillite	2100	2400
Rhyolites	2120	2230

Table 4.2, continued from previous page

Nettleton's method	Density range (kg m⁻³)	Mean density (kg m⁻³)
Hyaloclastites ridges	1600-2450	2000
Piles of lava	2500-2800	2600

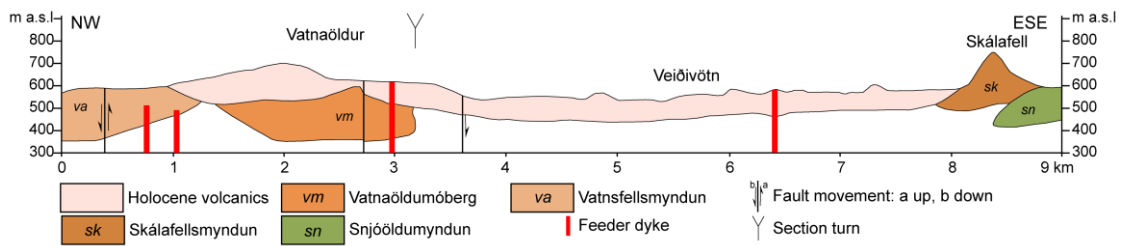


Figure 4.6 Cross-section over the Vatnaöldur and Veiðivötn fissures (see Figure 4.7 for the precise location) (Vilmundardóttir et al., 1988).

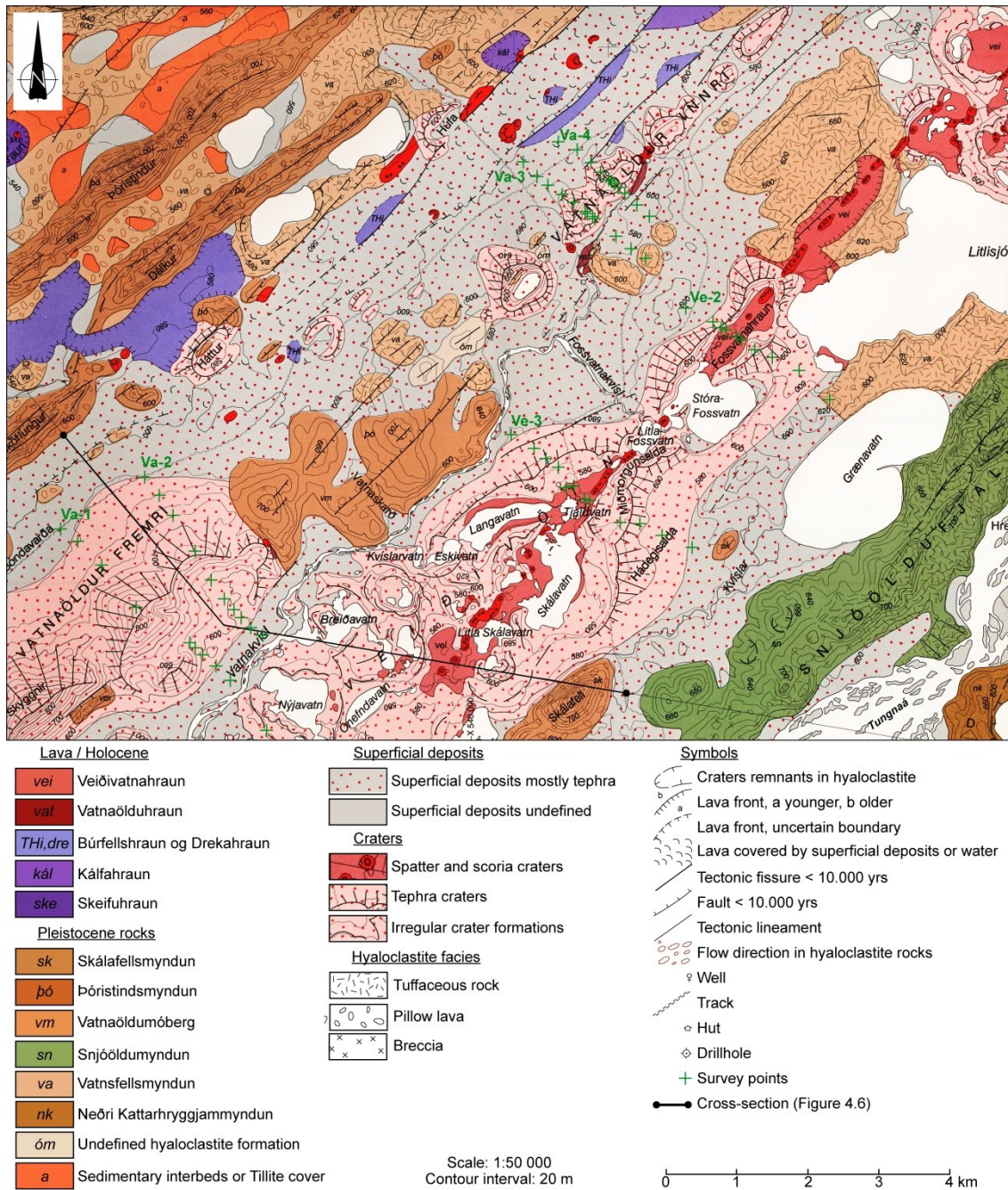


Figure 4.7 Bedrock geology at the Vantaöldur and Veiðivötn fissures, and immediate surroundings (Taken from Vilmundardóttir et al., 1988).

4.3.4.2 Tephra density measurements

Three tephra samples were taken at the northwestern side of Va-3 by Þorsteinn Jónsson (Figure 4.1 and Appendix B). A measuring glass of 0.0005 m^3 (500 mL) and a weight were used in the lab for determining both wet tephra and dry tephra densities. For calculating the wet densities, the tephra-filled measuring glass was weighted once per sample. The mass of the glass was subtracted from the obtained value in order to get the mass (kg) of 0.0005 m^3 of wet tephra. The wet density in kg m^{-3} was calculated by dividing the tephra mass by the filling volume of 0.0005 m^3 . The samples were then dried in an oven at 40° , for 92 hours. The dry densities were obtained following the same procedure, but a mean mass of tephra was determined out of 10 measurements for each sample.

One of the samples mostly contains lapilli-size tephra, whereas the two others are mainly composed of fine-grained ash. The coarser tephra S1 has a bulk wet density of $\sim 1000 \text{ kg m}^{-3}$ and a bulk dry density of 800 kg m^{-3} (Table 4.3). Both finer-grained tephra have a bulk wet densities of $\sim 1900 \text{ kg m}^{-3}$; whereas the bulk dry tephra density is $\sim 1400 \text{ kg.m}^{-3}$ for sample S2 and $\sim 1550 \text{ kg.m}^{-3}$ for sample S3, which is slightly finer-grained than S2. The density differences between the samples are mainly due to porosity: the larger the pyroclasts, the more vesicles, the higher the porosity, the less dense the tephra. Note that the three samples come from the same area but do not have the same grain-sizes, neither the same densities. A relatively wide range of densities has therefore to be considered.

In the present area of study, the groundwater level is relatively high, causing the full saturation of the tephra deposits that are mostly ash-sized (Larsen, 1984). At the groundwater level, the bulk water-saturated density of the basaltic tephra should therefore be close to 1900 kg.m^{-3} ; whereas at the crater rims, the tephra is mostly expected to have a bulk density closer to dry densities. Since there are only three samples, one must be careful in drawing conclusions from the density values. However, given that they lie within the values commonly found for basaltic tephra (e.g. Oddsson, 2007, 2012), it is reasonable to assume that the bulk densities used for modelling of the gravity at the rims should lie within the range of the sample dry densities. Density is expected to increase somewhat with depth due to compaction, and given the abundance of submillimeter tephra in both Vatnaöldur and Veiðivötn (Larsen, 1984), mean dry density values closer to the higher end are considered to be the most appropriate.

Table 4.3 Bulk basaltic tephra densities determined from density measurements.

	Sample S1	Sample S2	Sample S3
Bulk grain size	Lapilli	Ash (dominant) and Lapilli	Ash
Wet density (kg m^{-3})	980 ± 65	1885 ± 40	1900 ± 40
Dry density (kg m^{-3})	805 ± 65	1420 ± 40	1545 ± 40

4.3.4.3 Topography densities of the anomalous bodies (Nettleton's method)

The Nettleton's method (Nettleton, 1976) is used to determine the densities of the topographic formations crossed by a gravity profile, in local survey investigations. It consists of calculating the Bouguer anomalies (BA) along the profile for a specific range of density values and comparing the resulting curves: the gravity anomaly curve that shows the least correlation with the topography is assumed to refer to the density of the

topographic formations (Kearey *et al.*, 2002). The Nettleton's method can therefore be applied to determine the density of anomalous bodies lying close to the surface and that are not buried beneath other geological formations of different densities, but they can overlie some materials of constant density (Ágústsdóttir, 2009).

The Nettleton's method was used in the present study to gain a first idea of the density of the crater rims. The selection of the densities that produced the anomaly curves with the least topographic correlation was usually relatively difficult as there was still some correlation observed with respect to the topographies (Figures 4.8 and 4.9). The topographic formations are probably underlain by other formations of different densities and along Veiðivötn, the additional effect of the dense lava within the craters may influence the density determinations of the ring formations. Table 4.3 summarizes the density values of the topographic materials, along each profile, inferred from the Nettleton's method.

Table 4.4 Density values of the topographic formations inferred from the Nettleton's method (a density value showing the least correlation with topography can be in many cases determined with an uncertainty of $\pm 50 \text{ kg m}^{-3}$).

Profile	Nettleton density (kg m^{-3})
Va-1	1700
Va-2	~1400-1500
Va-3	~1200-1300
Va-4	~1300-1400
Ve-1	~1500-1600
Ve-2	~1500-1600

Note that all the Nettleton densities are relatively close to the measured dry densities of the samples (see section 4.3.4.2), except at Va-1, where the density seems too high for basaltic tephra.

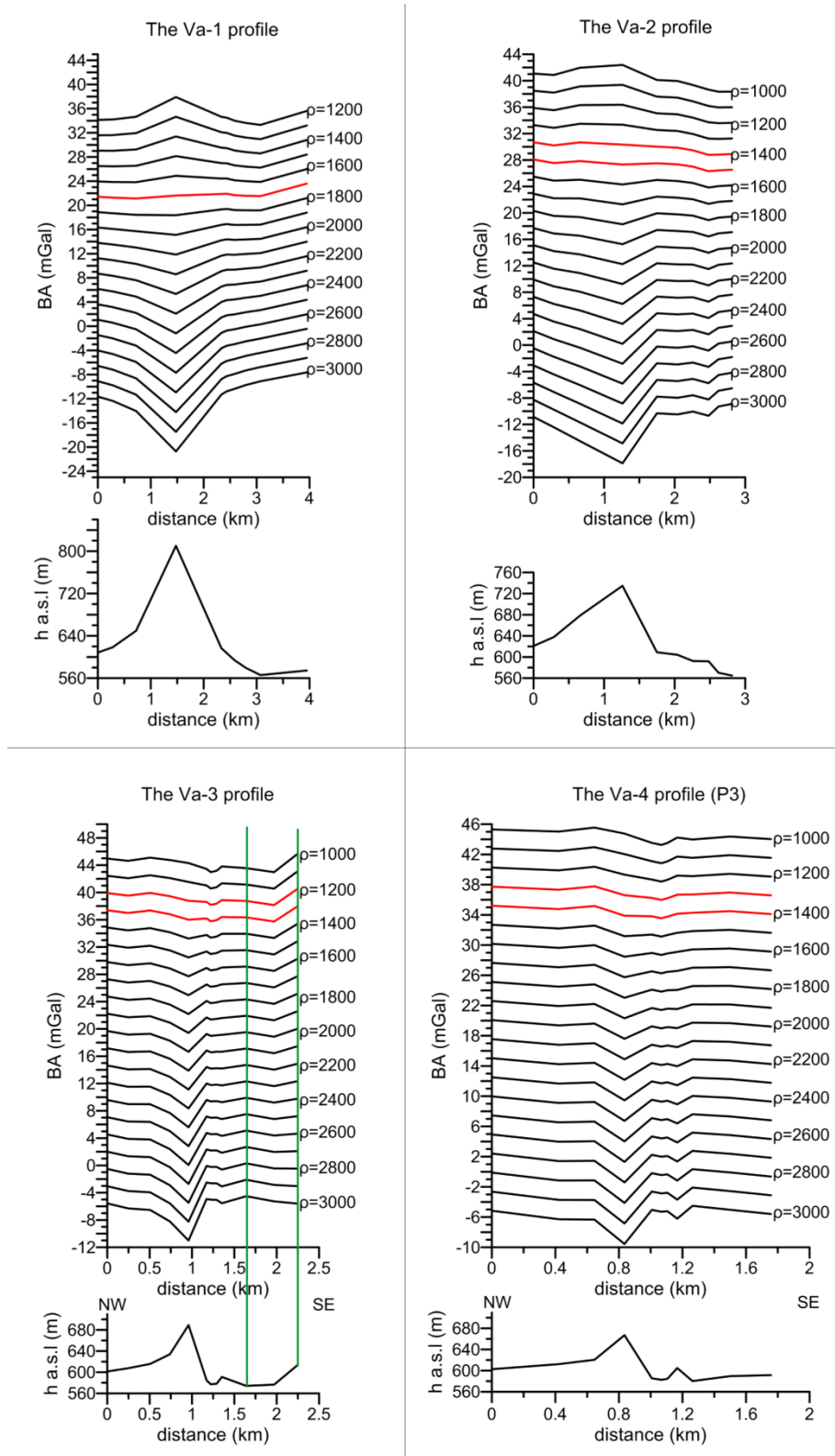


Figure 4.8 Density determinations of the topographic formations along the Vatnaöldur profiles using the Nettleton's method. The vertical green lines delimit some extra formations that need to be ignored as they do not belong to the volcanic edifices considered. "BA" refers to "Bouguer Anomaly", "h a.s.l." to the elevation above sea level and ρ to density values in kg m^{-3} .

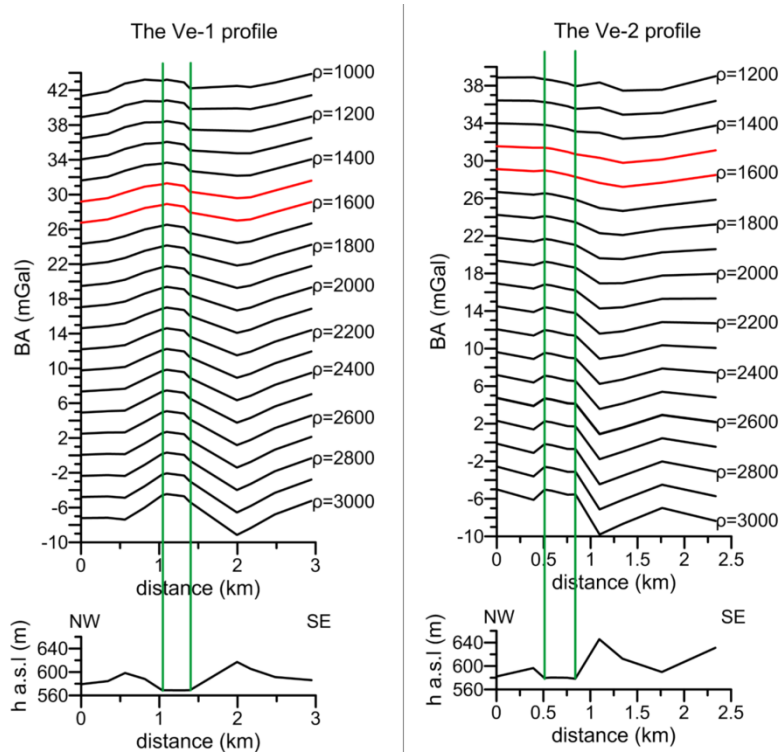


Figure 4.9 Density determinations of the topographic formations along the Veidivötn profiles using the Nettleton's method. The vertical green lines delimit the outcropping lava that may disturb the determination of the tephra topographic formations. "BA" refers to "Bouguer Anomaly", "h a.s.l." to the elevation above sea level and ρ to density values in kg m^{-3} .

4.3.5 Accuracy of the Bouguer anomalies

In general, the Bouguer anomaly values obtained at the end of the data processing are influenced by two main types of errors: systematic errors and random errors (Vilhjálmsón, 2006).

The uncertainty of the reduction density (2300 kg m^{-3}) is a systematic error that cannot be estimated, but its effect can be neglected for the present study (see section 4.3.4.1).

The random errors are either due to uncertainties in the measurements or due to particular environmental conditions (Vilhjálmsón, 2006). They must be estimated because they can greatly influence the Bouguer anomalies.

In order to reduce the errors when measuring with the LaCoste&Romberg (G445) gravimeter, the same surveyor measured all the survey points of the same profile. The reading accuracy of the LaCoste&Romberg (G445) gravimeter equals $\pm 0.01 \text{ mGal}$ (LaCoste & Romberg, Inc., 1979). Regarding the elevation measurements, an uncertainty of 0.06 mGal in the Bouguer anomalies was estimated (see section 4.3.1). Therefore, the error due to the equipment, $\Delta_{\text{equipment}}$, is equal to 0.07 mGal .

A small difference between the gravity station height and the DEM at the station is removed by setting the pixel containing the survey point at the height of the gravity station. This is done automatically by the `ttc25.exe` (see section 4.3.3) Fortran program. The

surrounding pixels are not adjusted. The random error, Δ_{TC} , expresses the slight potential height differences between the DEM topography and the GPS data out of each survey point pixel. For the present survey, Δ_{TC} , was estimated to be equal to or better than 0.1 mGal. Therefore, the maximum (worse case) error in the gravity anomaly was estimated to be equal to 0.17 mGal (Equation 4.3).

$$\Delta g_{\text{total}} = \Delta g_{\text{equipment}} + \Delta g_{TC} = 0.17 \text{ mGal}$$

Equation 4.3

Δg_{total} : Total uncertainty of the gravity anomalies (mGal)

$\Delta g_{\text{equipment}}$: Uncertainty of the gravity anomalies due to measurement errors (0.07 mGal)

Δg_{TC} : Uncertainty of the gravity anomalies in the data processing (0.1 mGal)

5 Forward modelling

The observed gravity signal of a profile represents the Complete Bouguer anomalies, BA (see section 3.3), against distance, for a specific background density. The term “observed” is used for the survey results, in contrast with the “calculated anomaly”, computed by the software used for modelling (see further); and should not get confused with the “observed gravity” value obtained after the tidal and drift corrections (see section 3.2.2).

The observed gravity signal is influenced by both local and regional density anomalies. The fluctuations highlighted on the observed gravity signal reflect local density variations within the subsurface just along the profile; whereas the overall tilt of the observed gravity curve expresses regional density variations (e.g. Kearey *et al.*, 2002). For the present study, the overall trend of each gravity signal was removed graphically in order to eliminate the regional effects and to focus on the residual observed gravity anomaly (e.g. Kearey *et al.*, 2002).

The Gravmag software (Pedley *et al.*, 1993) was used for 2.5-D forward modelling, which consists of drawing polygons of specific densities along a profile (i.e. in the X-Z plane), and assigning them half-strike length values in the third dimension (Figure 5.1). The program divides each polygon into several compartments of regular shapes and calculates their gravity anomaly effects at each survey point, on the basis of Equation 3.6 (where h represents the distance from the survey point to the slab of finite strike length, in the X-Z plane) (e.g. Kearey *et al.*, 2002). A calculated gravity anomaly is generated from the summing of all the polygons making the model. By modifying both the shapes and densities of the polygons, the calculated gravity signal can be adjusted to the residual observed gravity anomaly. Infinite combinations of density values and polygon shapes can produce the same calculated gravity signals (Figure 5.2). The number of plausible models for a given profile can however be strongly reduced by considering the geology of the area. In the following paragraphs, the residual observed Bouguer gravity anomaly is simply referred to as observed gravity.

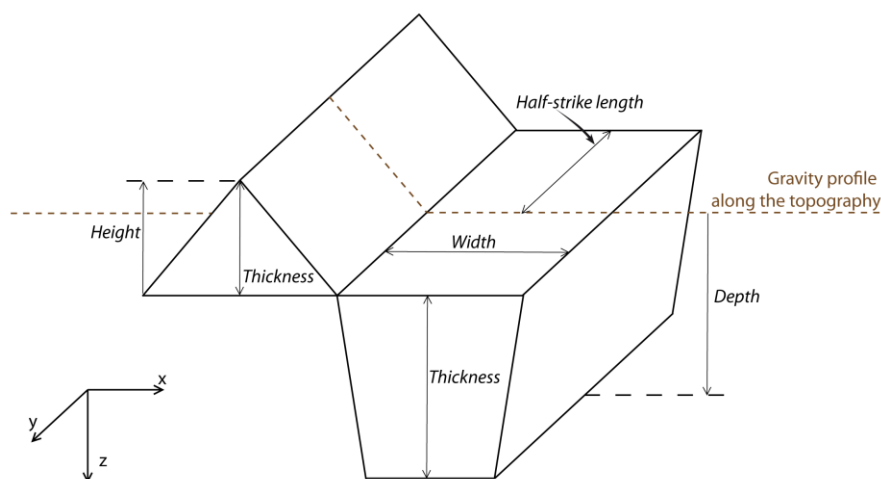


Figure 5.1 Schematic cross-section of a 2.5-D gravity forward model defining the terminology used for modelling descriptions. The gravity profile lies in the X-Z plane and the polygons have a finite strike length defined in the Y-direction.

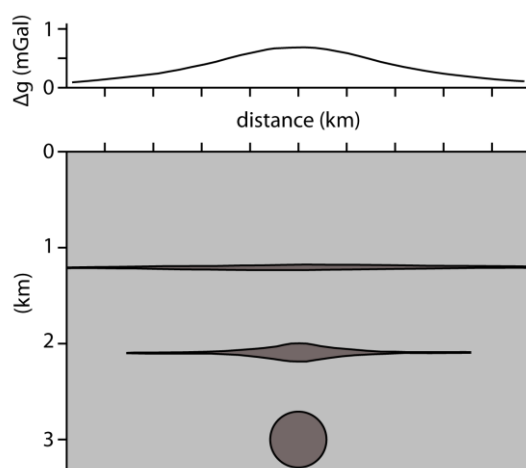


Figure 5.2 Bodies of same densities having different shapes and lying at different depths can produce the same gravity anomaly (Lutz, 2009).

For each observed gravity profile of the present survey, the horizontal line of 0.00 mGal represents the gravity signal that would be produced by a homogeneous subsurface (see further, Figure 5.4). An anomalously low density body would generate a negative gravity anomaly (below the reference line); whereas an anomalously dense body would produce a positive gravity anomaly (above the reference line). The locations of the bodies can therefore be assumed relatively precisely through the observed gravity fluctuations. In the present study, based on the geology of the area (see sections 1.3 and 1.4), a relatively dense body would refer to lava; whereas a relatively light body would refer to tephra.

2.5-D forward modelling was performed in three steps for each gravity profile:

- Nettleton densities (see section 4.3.2.3) were attributed to polygons representing the topographic formations, i.e. the rim formations;
- Densities and polygon shapes were adjusted in order to reproduce the observed gravity anomaly, i.e. to fit as best as possible the calculated gravity signal to the observed gravity signal;
- Alternative models were suggested in coherence with the geological context of the area.

Note that the half-strike lengths of the polygons were determined from the approximate crater diameters (Table 5.1).

Table 5.1 Half-strike lengths of the polygons determined from the approximate crater diameters.

Profile	Half-strike length of the polygons (m)
Va-1	670
Va-2	540
Va-3	190
Va-4	190
Ve-1	390
Ve-2	260

The aim of the present study was to study shapes and densities of the volcanic conduits as a first approach, similar to Mrlina *et al.* (2007) (see section 2.3.1). The polygons were constructed with the simplest geometry that provided good fit of calculated to observed gravity values.

The profiles at Vatnaöldur have been grouped by region for modelling descriptions, i.e. Vatnaöldur Innri and Vatnaöldur Fremri (Figure 5.3); finally both profiles from Veiðivötn are detailed.

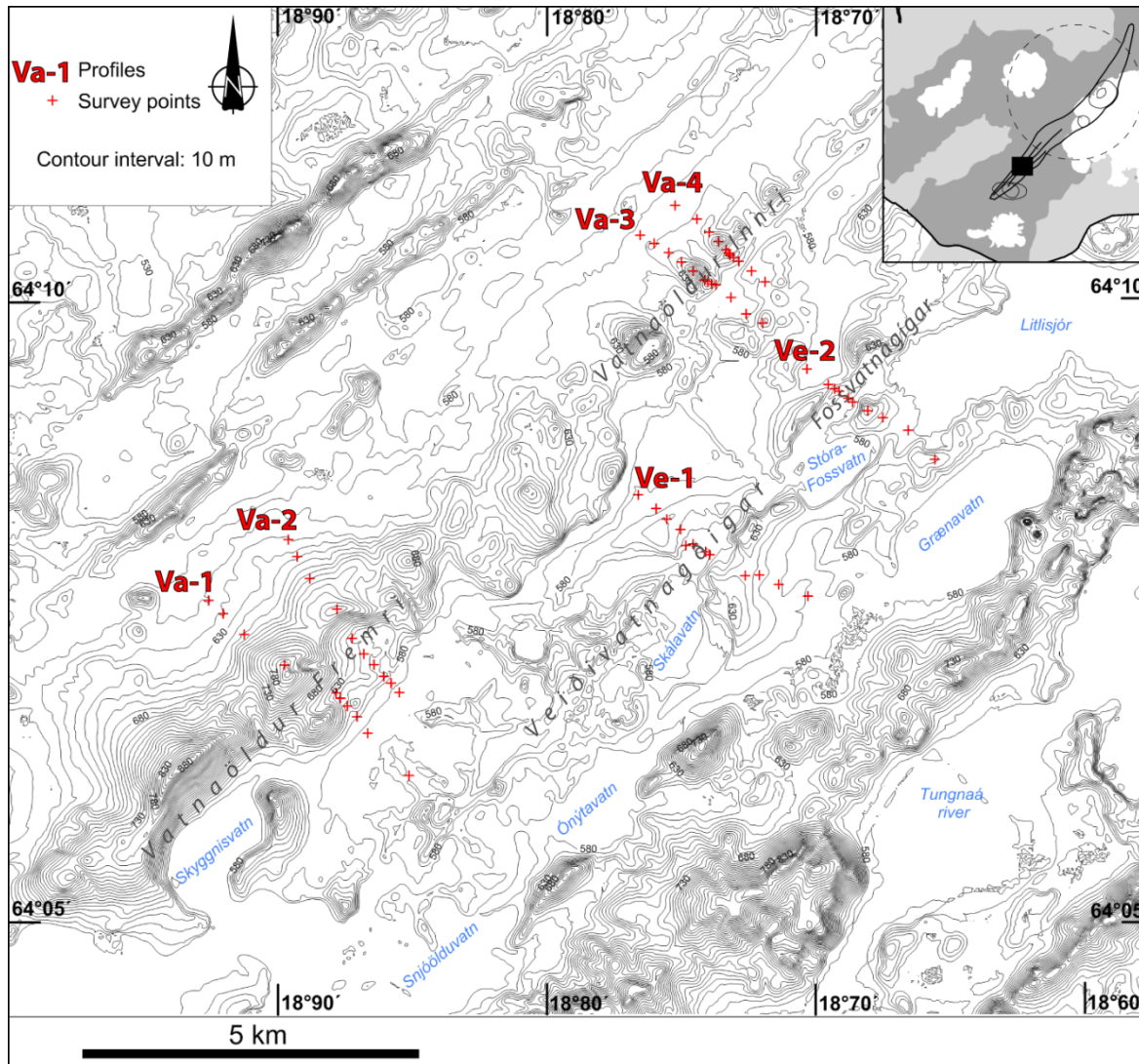


Figure 5.3 Topographic map of the area of study (DEM of 25 m grid spacing - see section 4.2.). The names in blue refer to the main lakes and river beds (see Figure 4.1 for more details). The location of the area (top right corner) comes from Figure 1.2.

5.1 Forward modelling at Vatnaöldur Innri

The Nettleton densities of the topographic formations at both Va-3 and Va-4 were inferred to be $\sim 1200\text{--}1300 \text{ kg m}^{-3}$ and $1300\text{--}1400 \text{ kg m}^{-3}$, respectively (see section 4.3.4.3). Instead of choosing the mean density values, the common value of 1300 kg m^{-3} was attributed to the rims at both Va-3 and Va-4 as starting values for forward modelling, as it allowed a better fit in gravity signals than 1400 kg m^{-3} .

5.1.1 Profile Va-3

The Bouguer anomaly in profile Va-3 is dominated by gravity lows (Figure 5.4), implying the presence of relatively low density bodies ($< 2300 \text{ kg m}^{-3}$): the main gravity low anomaly reaches -3.86 mGal at the NW-rim; whereas the SE-rim produces a low of -0.50 mGal . The two survey points, seen on the SE edge of the profile (Figure 5.4), are not

considered in the modelling procedure because they belong to a geologic formation not related to the crater row under consideration (Figure 4.7).

The main negative peak of gravity anomaly, reaching -3.86 mGal, aligns with the crest of the NW crater rim that rises at ~690 m a.s.l. The SE crater rim, rising at ~590 m a.s.l., produces a lower gravity anomaly of -0.50 mGal (Figure 5.4). Those relative lows indicate the approximate locations of low density bodies.

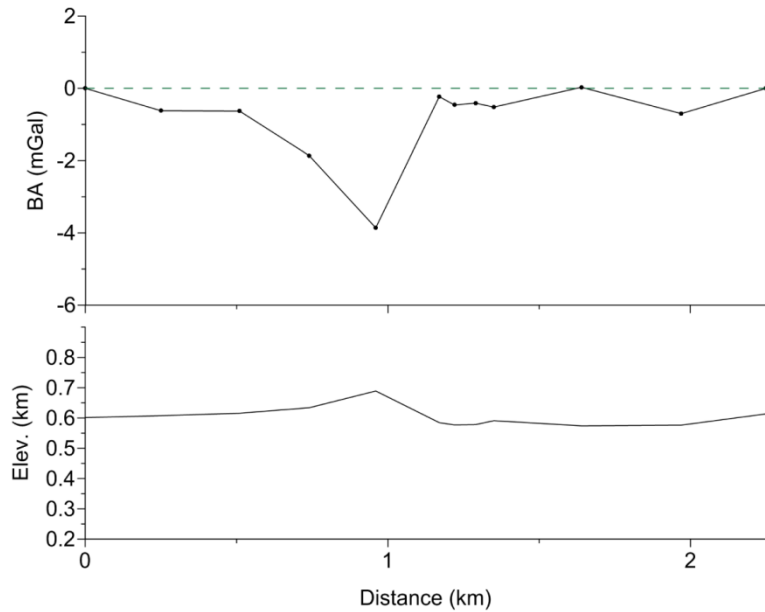


Figure 5.4 Observed gravity anomaly (top) along the Va-3 profile (Vatnaöldur Innri): the variations of the Bouguer anomaly (BA) are compared with the topography (bottom). The green dashed line refers to the gravity signal produced by a homogeneous subsurface of 2300 kg m^{-3} . Note that “Elev.” refers to “Elevation” (Scale 1:1).

A simple model, only taking into account densities of the crater rims using the best-fitting Nettleton density of 1300 kg m^{-3} , is shown (Figure 5.5.a) and two observations can be made. (1) The fit at the crater is not good, since a small gravity high appears where none is observed. An additional anomalous body having a density below 2300 kg m^{-3} has to be inserted under the crater’s centre to obtain a decent fit. (2) The Nettleton density is apparently somewhat too high to provide a proper fit over the northwestern (higher) crater rim.

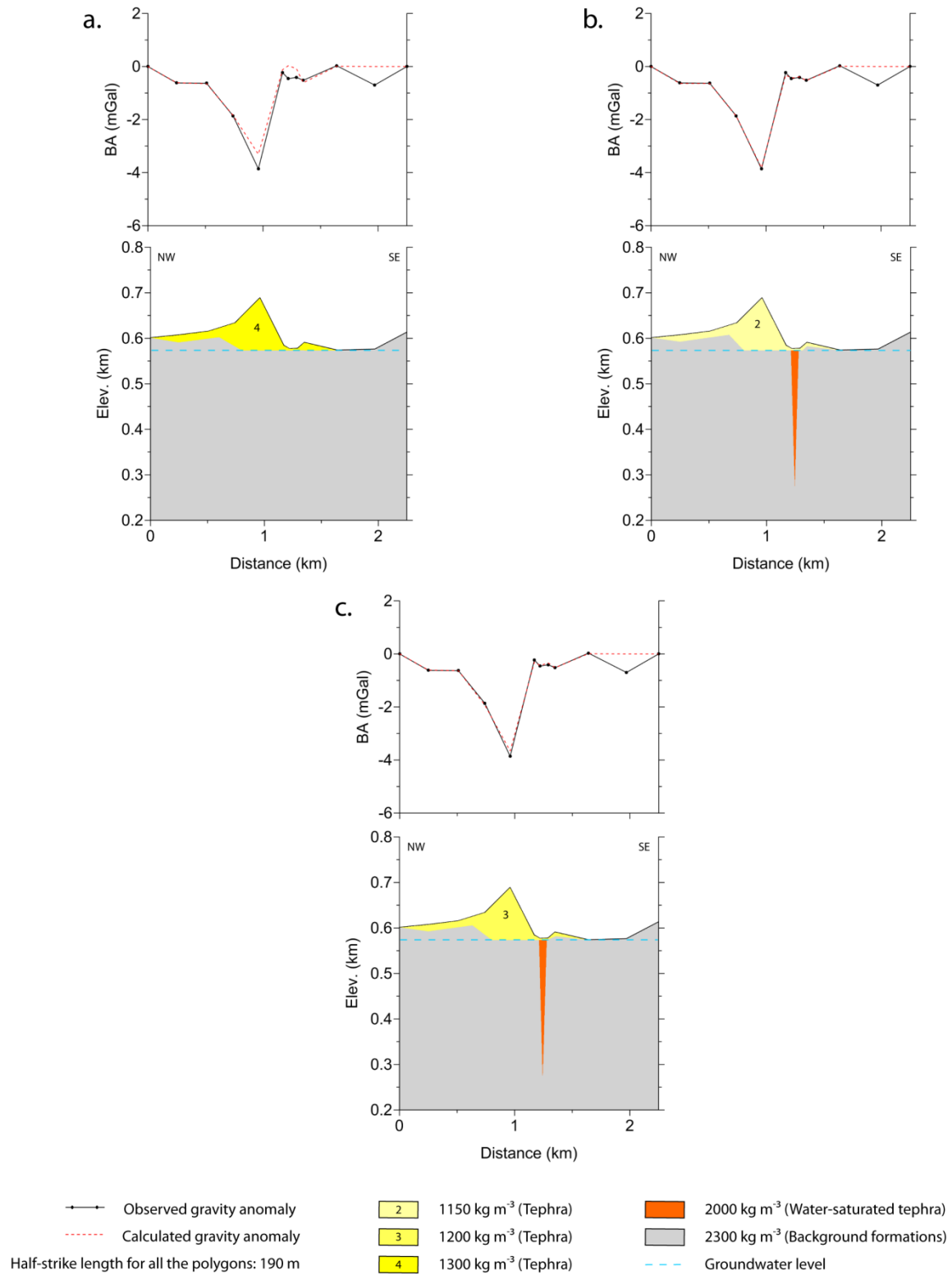


Figure 5.5 2.5-D gravity forward modelling highlighting the volcanic structure of the edifice crossed by the Va-3 gravity profile (Vatnaöldur Innri). a. Forward model based on the Nettleton density; b. Forward model showing the adjustments inferred from a.; c. Alternative plausible forward model. Note that “BA” refers to “Bouguer Anomaly” and “Elev.” refers to “Elevation” (Vertical exaggeration 4:1).

A second forward model is presented in Figure 5.5.b. The density of the crater rims has been lowered to 1150 kg m^{-3} , providing a good fit to the observations. The shapes of the polygons were also slightly modified to improve the fit. The steps that appear at the bottom of the rim polygons seem to be coherent with the location of the graben faults shown on the geological map (Figure 4.7). At the crater location, a cone-shaped body of $\sim 300 \text{ m}$ length and $\sim 65 \text{ m}$ maximum width at its top, having a bulk density of 2000 kg m^{-3} has been inserted. Its density value of 2000 kg m^{-3} was decided as the most plausible one, being consistent with unconsolidated and water-saturated tephra, lying as it does below the groundwater table. The average density of basaltic glass is close to 2700 kg m^{-3} (e.g. Franzson *et al.*, 2001). A porosity of 40% is a reasonable value for phreatomagmatic tephra (e.g. Franzson *et al.*, 2001). Using these values, the bulk density of the unconsolidated water-saturated tephra is $\sim 2000 \text{ kg m}^{-3}$ (Equation 5.1).

$$\rho = (1 - \phi) \rho_g + \phi \rho_{\text{por}} = 2020 \text{ kg m}^{-3} \approx 2000 \text{ kg m}^{-3} \quad \text{Equation 5.1}$$

ρ : Bulk density of unconsolidated water-saturated basaltic tephra (kg m^{-3})
 ϕ : Assumed porosity of the unconsolidated tephra (40%)
 ρ_g : Basaltic glass mean density (2700 kg m^{-3})
 ρ_{por} : Density of the water-saturated pores (1000 kg m^{-3})

A third alternative model demonstrates the approximate nature of the density values attributed to the tephra rims. In Figure 5.5.c, tephra rims of 1200 kg m^{-3} produce a good fit, obtained by slightly altering the basal geometry of the polygons.

5.1.2 Profile Va-4

The observed gravity anomaly at Va-4 is very similar to that of Va-3 but the gravity low associated with the rims are not as deep, reaching -2.69 mGal and -0.38 mGal at the NW- and SE-rims, respectively. Models for Va-4 (Figure 5.6.a, b and c) based on the same principles as for Va-3 yield essentially the same results. The main difference is that the assumed low density water-saturated tephra lying under the centre of the crater is shallower ($\sim 85 \text{ m}$) and slightly wider ($\sim 85 \text{ m}$).

The graben faults noticed at the bottom of the tephra polygons at Va-3 (see section 5.1.1) are also apparent in Va-4. The throw of the NW-margin of the graben is 20-25 m towards southeast. This is similar to the elevation difference of the land on the northwestern and southeastern sides of the crater row.

Comparing the tephra density errors inferred from both Va-3 and Va-4, it can be considered that the average error for density values of the tephra polygons is $\pm 100 \text{ kg m}^{-3}$. This observation confirms that the choice of 1300 kg m^{-3} for the Nettleton density at Va-3 and Va-4 remains consistent.

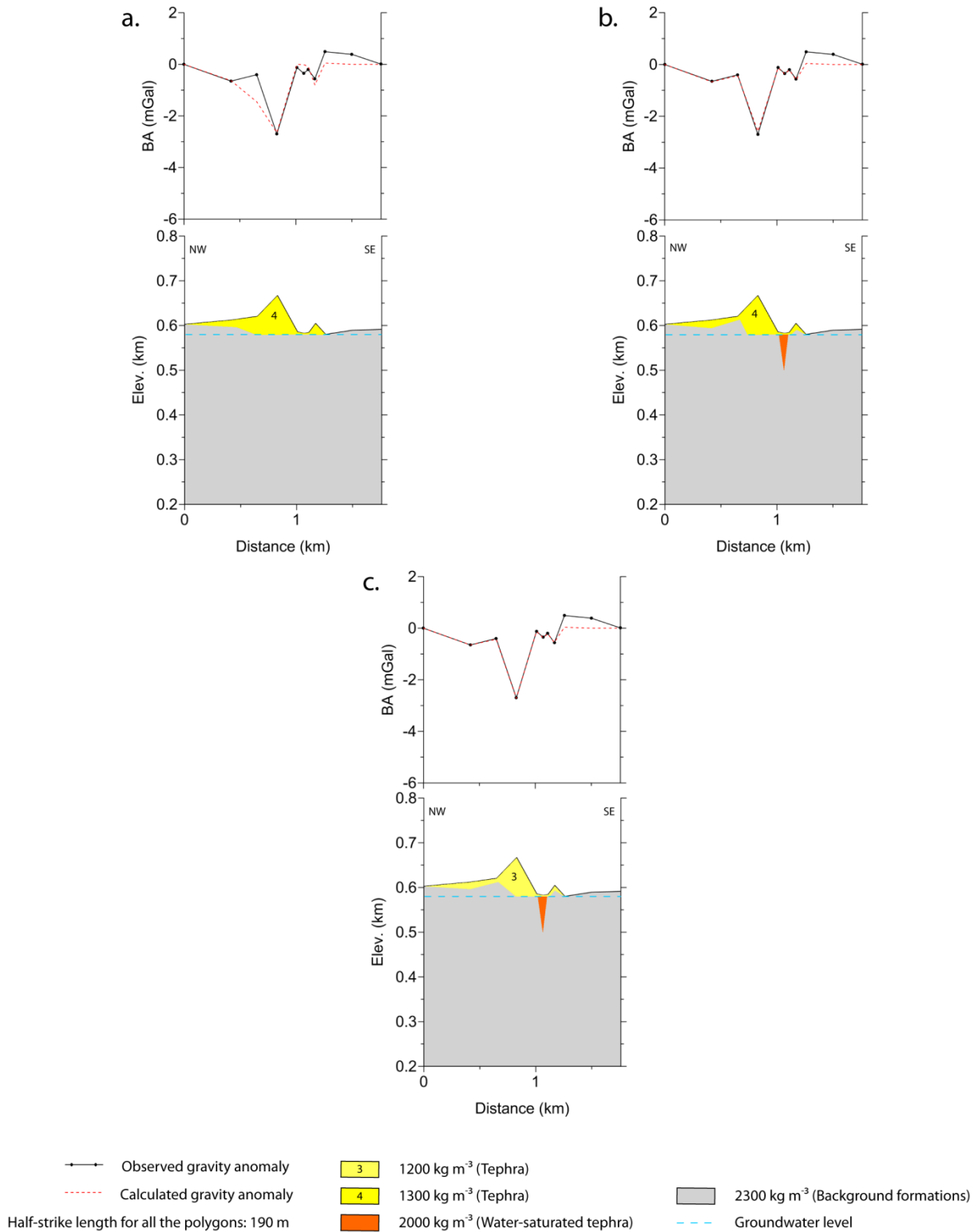


Figure 5.6 2.5-D gravity forward modelling highlighting the volcanic structure of the edifice crossed by the Va-4 gravity profile (Vatnaöldur Innri). a. Forward model based on the Nettleton density; b. Forward model showing the adjustments inferred from a.; c. Alternative plausible forward model. Note that “BA” refers to “Bouguer Anomaly” and “Elev.” refers to “Elevation” (Vertical exaggeration 4:1).

5.2 Forward modelling at Vatnaöldur Fremri

The Nettleton densities of Va-1 and Va-2 are 1700 kg m^{-3} and $\sim 1400\text{-}1500 \text{ kg m}^{-3}$, respectively (see section 4.3.4.3). Instead of choosing a common mean value for both adjacent profiles, the forward modelling procedure was started using the Nettleton density of 1700 kg m^{-3} at Va-1. At Va-2, the value of 1400 kg m^{-3} was selected as a starting density.

5.2.1 Profile Va-1

The observed Bouguer anomaly Va-1 is dominated by lows as in Va-3 and Va-4. The main signal is a low registering a relative value of -5.20 mGal , observed at the crest of the NW crater rim that rises at $\sim 810 \text{ m a.s.l.}$ (Figure 5.7). No crater rim appears on the SE part of the profile and no significant gravity anomaly is apparent. Between the distances of ~ 2.5 and $\sim 3.0 \text{ km}$ from the NW end of the profile, a relatively wide low anomaly is observed, from -1.14 to -1.23 mGal .

Using the Nettleton density of 1700 kg m^{-3} , the calculated gravity anomaly fits relatively well with the observed gravity anomaly (Figure 5.7.a), but the low observed between ~ 2.5 and $\sim 3.0 \text{ km}$ is not reproduced: an additional low density body would be required to simulate the calculated anomaly.

As mentioned in section 4.3.4.3, a density of 1700 kg m^{-3} for basaltic tephra seems too high and a density value closer to the one suggested at Va-3 and Va-4 (see sections 5.1.1 and 5.1.2) would be more suitable. A first assumption explaining this relatively high Nettleton density would be that greater compaction in a thicker pile of tephra would lead to higher bulk density in Va-1 compared to Va-3 and Va-4 (Figure 5.3). However, this hypothesis needs to be quantified in order to be certified. A second assumption is supported by the geology: the presence of a hyaloclastite ridge would reach $\sim 700 \text{ m a.s.l.}$ beneath the NW-rim (Figure 4.7). A second forward model is based on this assumption (Figure 5.7.b): the density of the hyaloclastite ridge was assumed to be in the range of 1800 kg m^{-3} to 2000 kg m^{-3} (Schopka *et al.*, 2006; Table 4.2). The resulting hyaloclastite body has a maximum height of $\sim 150 \text{ m}$, a minimum width of $\sim 600 \text{ m}$ at its top and a maximum width of $\sim 2.2 \text{ km}$ at its bottom. The inclusion of the hyaloclastite ridge in the model results in a best fit density for the tephra of 1300 kg m^{-3} , in agreement with the tephra densities used for Va-3 and Va-4. A parallelepiped body of unconsolidated water-saturated tephra of 2000 kg m^{-3} (Equation 5.1), measuring $\sim 55 \text{ m}$ height and $\sim 280 \text{ m}$ width improves the fit, between ~ 2.5 and $\sim 3.0 \text{ km}$. However, the origin of this body cannot be explained in association with the formation of the craters, as it lies outside the crater area (Figure 4.7).

A model with a shorter hyaloclastite body that does not overlap the conduit is shown in Figure 5.7.c. In order to adjust both gravity anomalies, a high density body has to be inserted where the upmost part of the conduit is located. This body is cone-shaped, reaching a depth of $\sim 100 \text{ m}$, a maximum width of $\sim 380 \text{ m}$ and having a density of 2600 kg m^{-3} . The choice of 2600 kg m^{-3} is based on previous gravity studies performed in Iceland indicating that this density is common for surface lava bodies (e.g. Gudmundsson and Högnadóttir, 2007).

5.2.2 Profile Va-2

The observed gravity anomaly of Va-2 is similar to the Va-1 gravity signal: the NW-rim produces a gravity low of -4.30 mGal and a low of -1.03 mGal appears between ~2.2 and ~2.6 km, i.e. outside the crater area. A series of models using the same methodology as for the other Vatnaöldur profiles is shown for Va-2 in Figure 5.8. The simple, single density contrast model (Figure 5.8.a) fails to explain the observed anomalies as in the previous models. It is not possible to distinguish between models b and c in Figure 5.8 since both satisfy the constraints from the surface geology and both provide good fits to the anomalies: gravity data do not allow the evidence of a clear volcanic conduit. This highlights a limitation of the present gravity survey: the presence or absence of relatively small bodies of light material is hard to verify or discard.

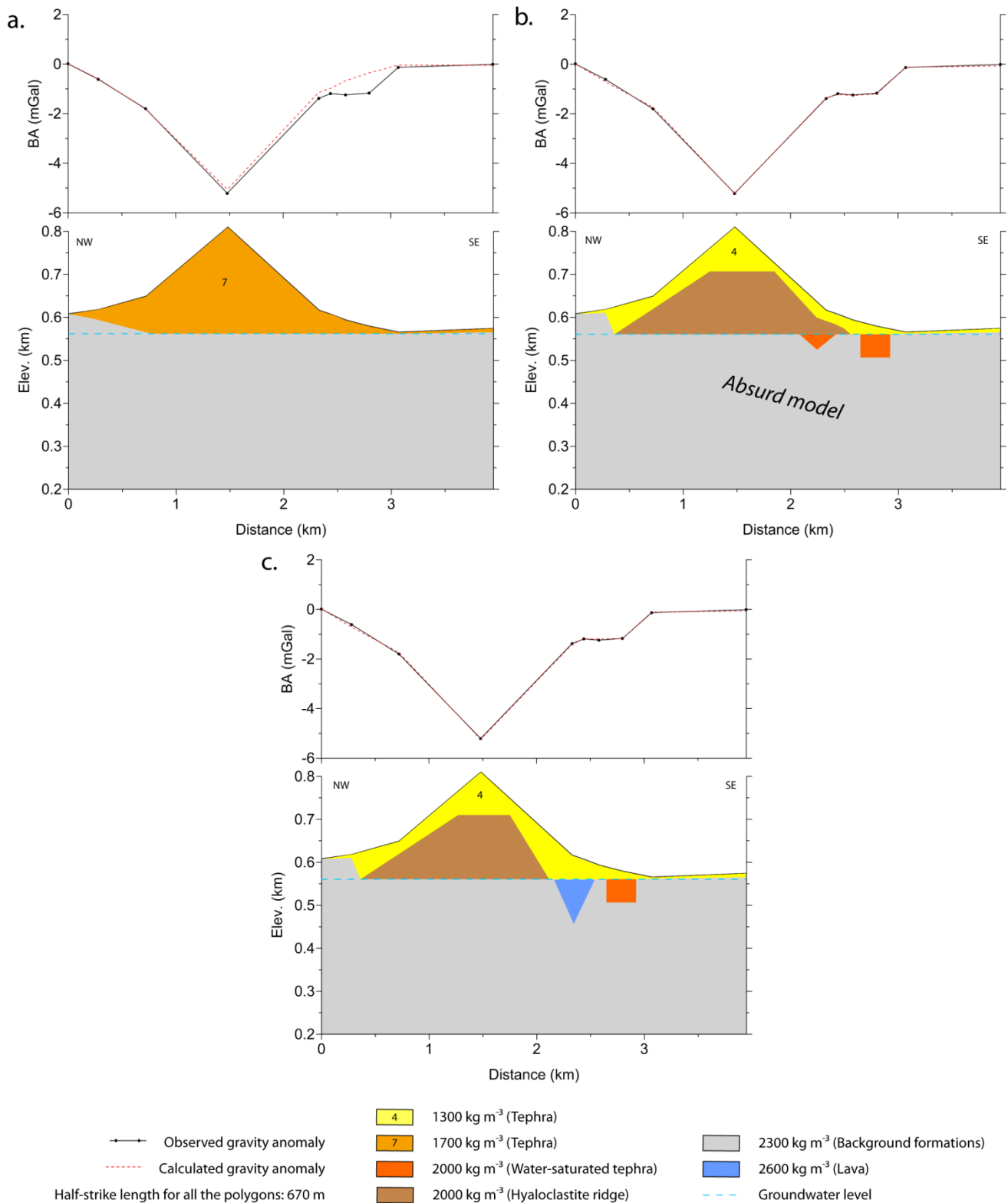


Figure 5.7 2.5-D gravity forward modelling highlighting the volcanic structure of the edifice crossed by the Va-1 gravity profile (Vatnaöldur Fremri). a. Forward model based on the Nettleton density; b. Forward model showing the adjustments inferred from a. (absurd solution); c. Forward model adjusted from b., in coherence with the geological history. Note that “BA” refers to “Bouguer Anomaly” and “Elev.” refers to “Elevation” (Vertical exaggeration 4:1).

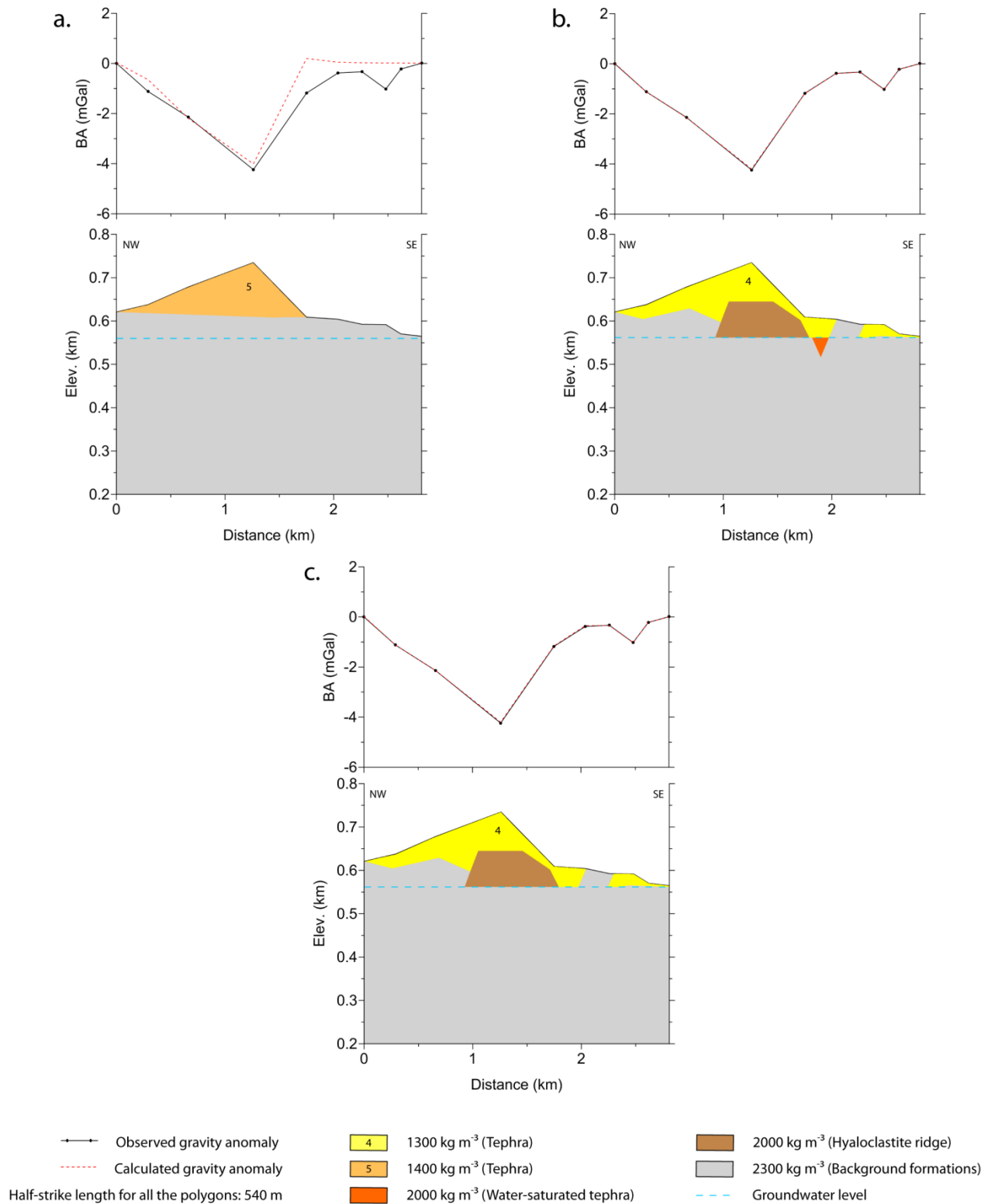


Figure 5.8 2.5-D gravity forward modelling highlighting the volcanic structure of the edifice crossed by the Va-2 gravity profile (Vatnaöldur Fremri). a. Forward model based on the Nettleton density; b. Forward model showing the adjustments inferred from a.; c. Alternative plausible forward model. Note that “BA” refers to “Bouguer Anomaly” and “Elev.” refers to “Elevation” (Vertical exaggeration 4:1).

5.3 Forward modelling of the Veiðivötn profiles Ve-1 and Ve-2

The Nettleton density at both Ve-1 and Ve-2 is $\sim 1500\text{--}1600\text{ kg m}^{-3}$ (see section 4.3.4.3). The common value of 1500 kg m^{-3} was chosen to start the forward modelling procedure, as it led to the closest fit between the calculated and observed gravity signals, compared with 1600 kg m^{-3} .

5.3.1 Profile Ve-2

The observed gravity anomaly at Ve-2 is similar to the Vatnaöldur profiles, with two gravity lows (-2.17 mGal and -0.33 mGal), produced respectively by the SE and NW crater rims. The SE-rim rises at $\sim 645\text{ m a.s.l.}$; whereas the NW rim reaches $\sim 595\text{ m a.s.l.}$ The gravity anomaly is positive within the crater, where a relative high of $+0.33\text{ mGal}$, indicates the presence of a body with a density higher than the reduction density of 2300 kg m^{-3} . This effect must rise from the lava body that outcrops in the bottom of the crater (Figure 4.7).

The first forward model at Ve-2, based on the Nettleton density illustrates two main observations (Figure 5.9.a): (1) changing the shape of the SE tephra rim body to adjust both gravity anomalies would lead to an absurd shape; the tephra density should rather be decreased; (2) an anomalously dense body would be required beneath the NW half of the crater to raise the calculated anomaly to fit to the observed anomaly.

To fulfil those adjustments, the density of the tephra was lowered to 1100 kg m^{-3} and the lava body at the bottom of the crater was assigned a density of 2800 kg m^{-3} (Figure 5.9.b). The step at the bottom of the SE tephra rim body cannot be explained with features on the geological map (Figure 4.7). The value of 2800 kg m^{-3} for the lava body was preferred to 2600 kg m^{-3} (see section 5.2.1) because the lava was assumed to have degassed as a lava pond, since it stagnated within the crater. The lava body presents an irregular shape close to a non-symmetrical cone of maximum $\sim 275\text{ m}$ width at the surface, i.e. filling almost the entire crater, and having a maximum thickness of $\sim 35\text{ m}$, on the NW side of the crater.

The addition of an unconsolidated water-saturated tephra body of 2000 kg m^{-3} (Equation 5.1) beneath the SE crater rim, measuring $\sim 35\text{ m}$ in thickness, $\sim 515\text{ m}$ of maximum width at its top, and $\sim 260\text{ m}$ of minimum width at its bottom, allows an increase in the tephra rim density to 1300 kg m^{-3} (Figure 5.9.c), which is more coherent with the density measurements (see section 4.3.4.2). The assumed step at the base of the SE crater rim appears softened.

The idea that the 2800 kg m^{-3} body of lava could overlie a cone-shaped body of unconsolidated water-saturated tephra of 2000 kg m^{-3} (Equation 5.1) was explored in an alternative forward model (Figure 5.9.d). This possible model remains hypothetical, as it cannot be tested with the gravity data alone. Here tephra and lava bodies compensate each other since tephra produces a gravity low, whereas the overlying lava produces a gravity high. Infinite possible combinations of this type can be fitted to the observed Bouguer anomaly.

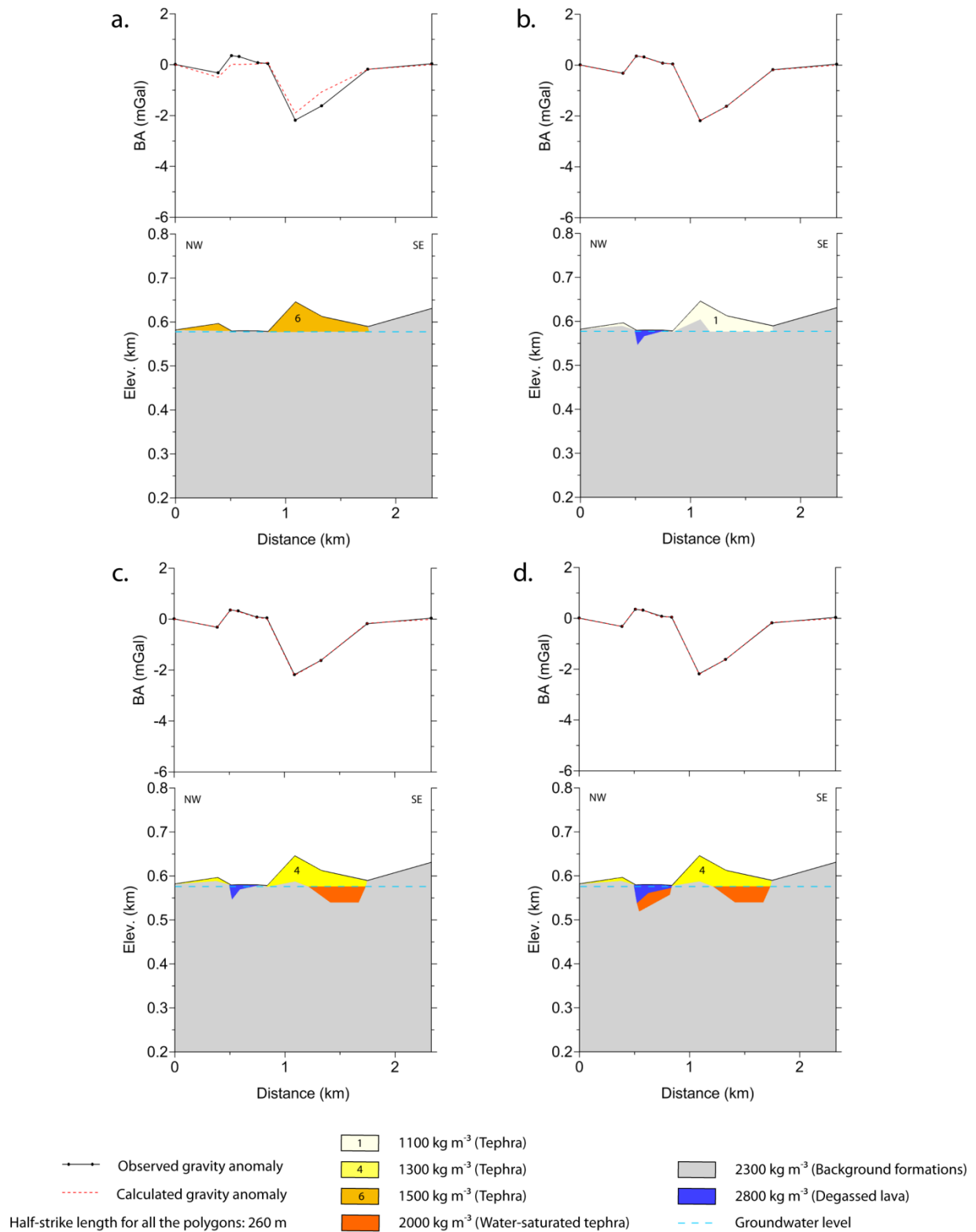


Figure 5.9 2.5-D gravity forward modelling highlighting the volcanic structure of the edifice crossed by the Ve-2 gravity profile (Veidivötn). a. Forward model based on the Nettleton density; b. Forward model showing the adjustments inferred from a.; c. A refined forward model; d. Alternative plausible forward model. Note that “BA” refers to “Bouguer Anomaly” and “Elev.” refers to “Elevation” (Vertical exaggeration 4:1).

5.3.2 Profile Ve-1

The Ve-1 profile shares the same characteristics as Ve-2, but the gravity high associated with the crater bottom is much larger. The SE crater rim of ~620 m height a.s.l. produces a low anomaly of -2.36 mGal; whereas the ~600 m high a.s.l. NW crater rim does not produce a low anomaly: a neutral gravity signal corresponds to the outer slope of the rim and the inner slope aligns with the start of a high positive anomaly of which the peak of +1.64 mGal is observed at the crater location.

The Ve-1 forward model using the Nettleton density of 1500 kg m^{-3} (Figure 5.10.a) shows that (1) the value of 1500 kg m^{-3} seems to be too high for characterizing the density of the SE crater rim; (2) a dense anomalous body is required at the crater location to explain the gravity high; (3) the NW-rim, made of tephra, seems to overlie a high density body. Note that the high associated with the crater bottom extends over the southeastern part of the rim.

In order to explain as well as possible the observed anomaly, the density of the tephra rim bodies was lowered to 1200 kg m^{-3} and a 30 m thick body of possible unconsolidated water-saturated tephra (2000 kg m^{-3} - Equation 5.1) was required for a better fit (Figure 5.9.b). Without this body, the tephra density had to be lowered to 1100 kg m^{-3} , which seems implausibly low compared to the other models and the measured bulk density of tephra (Table 4.3).

The lava body of 2800 kg m^{-3} is here interpreted as two distinct bodies: one within the crater, and the other below the NW crater rim. The latter could be explained as remnants from a possible older fissure. The prism shape of the lava body within the crater is ~85 m thick, ~350 m wide at the surface and ~235 m wide at its bottom. This exact prism is of course very approximate, and an alternative interpretation is given as a cone-shaped body of ~135 m maximum thickness and a maximum width of ~350 m (Figure 5.10.c).

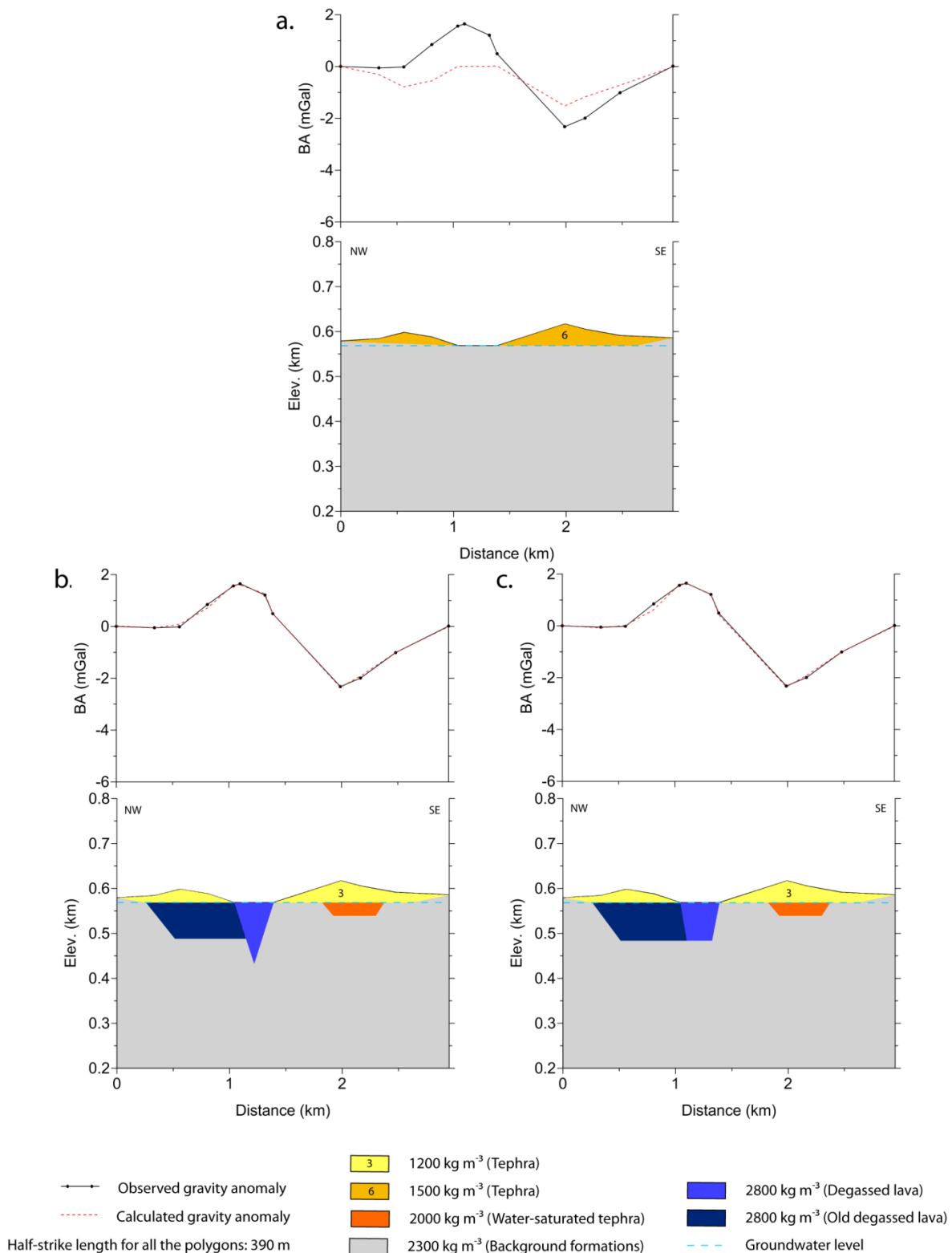


Figure 5.10 2.5-D gravity forward modelling highlighting the volcanic structure of the edifice crossed by the Ve-1 gravity profile (Veidivötn). a. Forward model based on the Nettleton density; b. Forward model adjusted with respect to the geological context; c. Alternative plausible forward model. Note that “BA” refers to “Bouguer Anomaly” and “Elev.” refers to “Elevation” (Vertical exaggeration 4:1).

6 Discussion

The gravity results provide important new insight regarding both the Vatnaöldur and Veiðivötn fissures. In this chapter, the implications of the results are discussed.

6.1 Conduit structures at Vatnaöldur

At Vatnaöldur Innri (Va-3 and Va-4), the most plausible forward gravity models to retain are Figure 5.5.b and Figure 5.6.c. They suggest tephra densities of 1150 kg m^{-3} and 1200 kg m^{-3} at Va-3 and Va-4, respectively (with a probable error of $\pm 100 \text{ kg m}^{-3}$); and the volcanic conduits appear to be filled with unconsolidated water-saturated tephra of $\sim 2000 \text{ kg m}^{-3}$ (see sections 5.1.1 and 5.1.2). At Vatnaöldur Fremri (Va-1 and Va-2), the most probable forward models are Figure 5.7.c and Figure 5.8.c. Both suggest a tephra density of 1300 kg m^{-3} underlain by an old hyaloclastite ridge of 2000 kg m^{-3} at the NW-rim (see section 5.2.1). A lava-filled volcanic conduit of 2600 kg m^{-3} is suggested at Va-1; whereas no clear evidence of a volcanic conduit can be brought out from gravity data at Va-2 (see section 5.2.2).

All models, except Va-2, suggest a shallow cone-shaped volcanic conduit significantly wider than any dike would be and resemble shallow diatreme structures (see section 2.2.3). The geometry of the volcanic edifices (scale 1:1) is more similar to tuff rings (Figures 2.4 and 2.6) (e.g. Lorenz and Sheridan, 1983; Lorenz, 1986) rather than maar volcanoes (Figure 2.3) (e.g. Lorenz, 2003): the gravity modelling suggests volcanic conduits shallower and thinner than common maar diatremes with respect to the rim sizes, and the bottoms of the craters remain above groundwater level (e.g. Lorenz *et al.*, 1970; Lorenz, 1986; White and Ross, 2011).

The absence of an anomalous cone-shaped body beneath the crater at Va-2 is not an argument to ensure that there is not a diatreme-like structure: a cone-shaped volcanic conduit may be filled by explosive material having a total bulk density that equals the reduction density of 2300 kg m^{-3} (see section 4.3.4.1). This hypothesis is likely as the process of formation of the Va-2 edifice must have been similar to the three other volcanic edifices studied, since they are composed of the same tephra (Larsen, 1984) and look similar apart from differences in size.

At Vatnaöldur Innri (Va-3 and Va-4), where the edifices are much smaller than at Vatnaöldur Fremri (Va-1 and Va-2), the preferred models indicate relatively thin conduits (~ 65 and ~ 85 m); whereas at Va-1, the conduit is much wider (~ 385 m) (Table 6.1). The depth to which the diatremes reach is not strongly constrained but seems to lie in the range 100-300 m.

The diatremes at both Va-3 and Va-4 were apparently filled with low density pyroclastic material ($\sim 2000 \text{ kg m}^{-3}$), characterizing the eruption at those vents as purely explosive (Figure 6.1). The Va-1 conduit seems to be filled with higher density material, consistent with a lava fill ($\sim 2600 \text{ kg m}^{-3}$). The assumed diatreme at Va-2 would also suggest filling-materials denser than pyroclasts.

The difference in diatreme filling materials between Vatnaöldur Innri and Vatnaöldur Fremri may indicate that the explosive phase of the AD 871±2 eruption first ended at Vatnaöldur Innri but lasted longer at Vatnaöldur Fremri. The isopach map of the Vatnaöldur tephra layer (Larsen, 1984) could support this assumption as the largest amounts of tephra seem to have been produced from the edifices of Vatnaöldur Fremri: the tephra layer around Va-1 and Va-2 is about 4 times thicker than around Va-3 and Va-4. This ratio can also be noticed from the difference in cross-sectional areas of tephra on the preferred models (Table 6.1). At Vatnaöldur Fremri, an effusive stage may have started at the very end of the eruption.

Table 6.1 Approximate dimensions of the volcanic edifices at Vatnaöldur (Va-) and Veiðivötn (Ve-), from the most probable forward models (Figures 5.5.b, 5.6.c, 5.7.c, 5.8.c, 5.9.c and 5.10.c). Refer to Figure 2.2 for terminology.

	Va-1	Va-2	Va-3	Va-4	Ve-1²	Ve-2
Bottom of the crater above/below groundwater level ¹	?	?	Above	Above	Below	Below
Maximum thickness of tephra at the rims (m)	~100	~90	~115	~90	~75	~65
Cross-sectional area of the tephra rim in model section (m ²)	~140,000	~130,000	~40,000	~20,000	~70,000	~45,000
Ring (or crater) diameter (m)	~385	?	~65	~85	~350	~275
Diatreme thickness (m)	~100	?	~300	~85	~135	?
Cross-sectional area of diatreme in model section (m ²)	~20,000	?	~10,000	~4,000	~25,000	?

¹ Conditions after the end of the eruption.

² The cone-shaped model has been chosen for better comparison

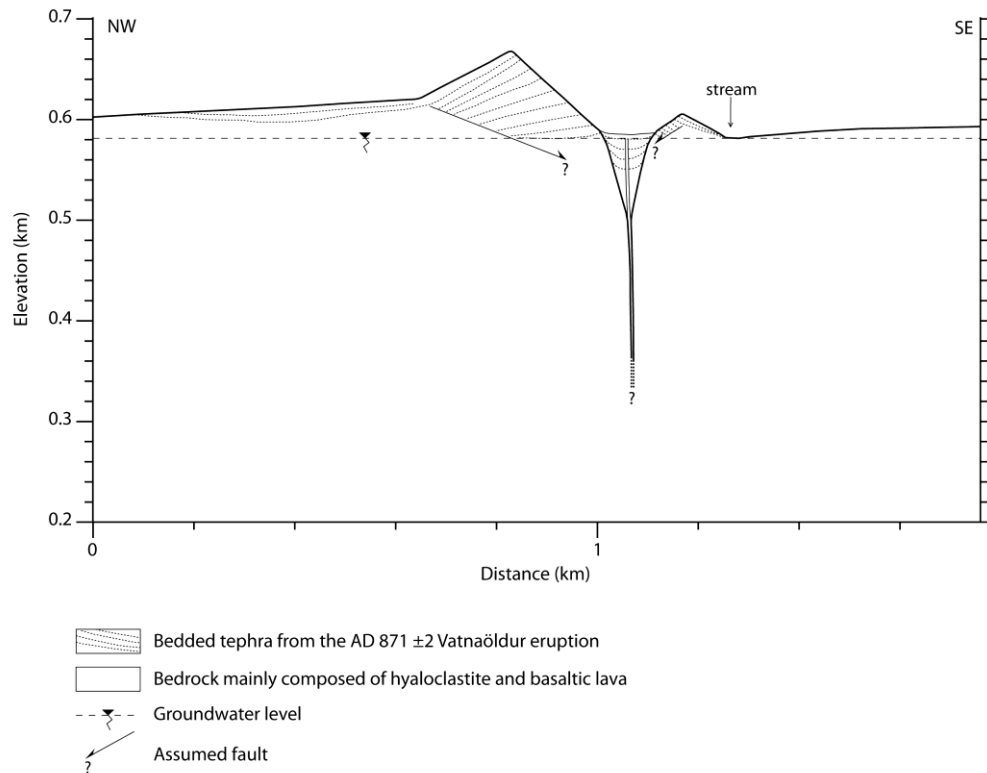


Figure 6.1 Schematic cross-section showing the phreatomagmatic structure of the purely explosive Va-4 edifice, highlighted by the forward gravity model of Figure 5.6.c (Vertical exaggeration 2:1).

6.2 Conduit structures at Veidivötn

At Ve-2, Figure 5.9.c refers to the most probable forward model that would best explain the observed gravity anomaly, in accordance with constraints provided by the geology. At Ve-1, the forward models that seem most plausible are 5.10.b and 5.10.c as the shape of the volcanic conduit cannot be determined from the present gravity data. At both locations, the models suggest similar tephra density values for the crater rims (1300 and 1200 kg m^{-3} at Ve-2 and Ve-1, respectively); and require some water-saturated tephra of 2000 kg m^{-3} beneath the SE tephra rims. The crater bottoms are covered with subaerial lava. Gravity modelling suggests that the volcanic conduits at both eruption sites are filled up with degassed lava having a density similar to 2800 kg m^{-3} . The amount of lava is significantly larger at Ve-1.

The preferred model 5.10.b at Ve-1 shows a cone-shaped volcanic conduit that resembles diatreme structure (see section 2.2), reaching a depth of $\sim 135 \text{ m}$ and having a width of $\sim 350 \text{ m}$ (Table 6.1). The “cut-cone-shaped” body suggested in the model 5.10.c may represent a diatreme structure that formed in a layered environment, where a soft-rock geological layer (Larsen, 1988) overlies a hard-rock layer (Figure 6.2). The Ve-1 crater can be considered as a maar volcano since its bottom lies under the groundwater table (e.g. Lorenz *et al.*, 1970; Lorenz, 1986; White and Ross, 2011).

The volcanic conduit suggested at Ve-2 does not match an explosive volcanic structure but it has a similar crater width as Ve-1 ($\sim 275 \text{ m}$). Moreover, as Ve-1 and Ve-2 both have

landforms resembling tuff rings (Figure 2.4) (Lorenz and Sheridan, 1983) and result from the same eruption, it can be assumed that the volcanic conduit at Ve-2 is also cone-shaped but the gravity survey does not show it: (1) the possible compensation of gravity signal from the dense lava body on the surface by an underlying low density tephra may make the entire conduit hard to highlight (Figure 5.9.d); (2) the cone-shaped diatreme may simply be filled with some material having a bulk density similar to that of the surrounding bedrock density. Neither of the two hypotheses can be selected as being the more probable from the present gravity survey.

Gravity modelling at Ve-1 suggests that the last effusive stage of the AD ~1477 Veidivötn eruption (Larsen, 1984) produced a significance amount of lava. The presence of older lava underlying the NW-rim can be plausible since a large number of lava flows have originated in this area before the Norse Settlement of Iceland (e.g. Vilmundardóttir, 1977).

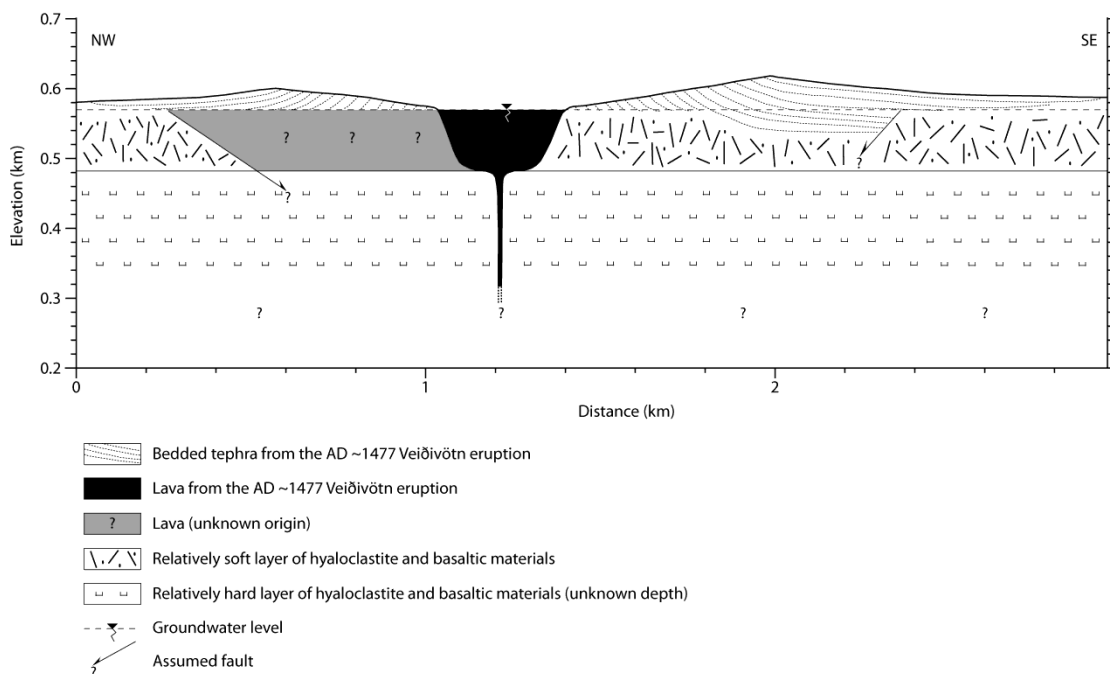


Figure 6.2 Schematic cross-section showing the phreatomagmatic structure of the explosive Ve-1 edifice, highlighted by the gravity forward model of Figure 5.10.c (Vertical exaggeration 2:1).

The craters studied form a spectrum from the Vatnaöldur purely explosive edifices (Va-3 and Va-4) to the Ve-1 crater, where effusive activity largely filled the explosive conduit. The Va-1 model shows a volcanic conduit of comparable size to that of the Veidivötn crater Ve-1, filled with lava (Table 6.1). However, the presence of lava remains hypothetical as no outcrops or drillholes exist at present to confirm it. Therefore, this edifice cannot be considered as an end-member with Ve-1 from the present gravity data.

The shallow conduit dimensions appear significantly greater at Ve-1 than at both Va-3 and Va-4: from the gravity modelling, Ve-1 has a diatreme ~3.5 times larger and a crater diameter ~4.5 times larger than both Va-3 and Va-4. Moreover, the amount of tephra

making the rims is ~2.5 times larger at Ve-1 (Table 6.1). The explosive activity must have been much greater at Veiðivötn than at Vatnaöldur Innri, leading to more excavation and larger tephra productions, which are supported by Larsen (1984). Note that the assumption of a soft-rock layer at Veiðivötn, inferred from the model 5.10.c could have contributed to the greater excavations of the conduits along this fissure (e.g. Lorenz, 2003).

The differences in dimensions between those two end-members can be supported by two studies based on volcanoclastic deposits: the mafic purely explosive Maegok tuff ring volcano (SE Korea) has a cone-shaped diatreme of ~185 m in thickness and being ~160 m wide (Kwon and Sohn, 2008); whereas, the andesitic Suoana maar volcano (Japan), where the activity changed from effusive to explosive, has a larger cone-shaped diatreme, being ~265 m wide, the diatreme is ~260 m thick (Geshi *et al.*, 2011).

7 Conclusions

The present gravity survey is a first step in the study of the subsurface volcanic structures at Vatnaöldur and Veiðivötn, where the surface geology has been studied in detail (e.g. Vilmundardóttir, 1977; Larsen, 1984). It reveals the overall structure and geometry of the diatremes, linked with either lava or water-saturated tephra-filling materials.

The two main questions addressed in the Introduction could be successfully answered:

- *What is the structure of the conduits at the selected volcanic edifices that formed during the AD 871±2 Vatnaöldur and AD ~1477 Veiðivötn phreatomagmatic eruptions and are there differences between both crater rows?*

The gravity survey gives indications of diatreme structures at both Vatnaöldur and Veiðivötn. The purely explosive and smaller edifices at Vatnaöldur Innri have apparently much narrower diatremes than at the Veiðivötn edifices, where a last effusive stage filled the conduits with lava.

- *What can those crater/conduit structures tell about the mechanism of the two eruptions and how do they compare with the results of other studies of similar volcanic structures?*

The difference in volcanic structure dimensions between the purely explosive edifices at Vatnaöldur Innri and the Veiðivötn edifices filled with lava indicate a greater volcanic activity at Veiðivötn that excavated more the diatremes and expelled a larger amount of pyroclasts. The contrast in dimensions and subsurface structure suggested by the results of the present gravity study broadly agree with what was expected from previous work based on geological studies of the products of the two eruptions (Larsen, 1984) and look similar to structure dimensions found at craters in Korea and Japan (Kwon and Sohn, 2008; Geshi *et al.*, 2011).

More complete results could be obtained by additional work:

- Borehole investigations within the Ve-2 crater would help defining the geometry of the lava body;
- Borehole investigations at the NW-rim of the Ve-1 volcano could confirm the assumptions made about the shape of the tephra body underlain by a relatively old lava body;
- Borehole investigations at the Va-1 crater would confirm the presence of lava filling the diatreme;
- Additional seismic refraction may be a relevant geophysical tool to delineate the assumed cone-shaped volcanic conduit at Va-2 (e.g. Schulz *et al.*, 2005).

References

- Ágústsdóttir, Th., 2009. On the dynamics of rhyolite dome displacement: densities and deformation fields. Master's thesis, University of Iceland, Reykjavík, 91pp.
- Bijwaard, H., W. Spakman, 1999. Tomographic evidence for a narrow whole mantle plume below Iceland. *Earth and Planetary Science Letters* 166, 121-126.
- Bjarnason, I.Th., 2008. An Iceland hot-spot saga. *Jökull* 58, 3-16.
- Björnsson, H., P. Einarsson, 1990. Volcanoes beneath Vatnajökull Iceland: Evidence from radio echo-sounding, earthquakes and jökulhlaups., *Jökull* 40, 147-168.
- Blake, S., 1984. Magma mixing and hybridization processes at the alkalic, silicic, Torfajökull central volcano triggered by tholeiitic Veiðivötn fissuring, South Iceland. *Journal of Volcanology and Geothermal Research* 22, 1-31.
- Cassidy J., S.J. France, A.A. Locke, 2007. Gravity and magnetic investigation of maar volcanoes, Auckland volcanic field, New Zealand, *Journal of Volcanology and Geothermal Research* 159, 153-163.
- Chambers, F.M., J.R.G. Daniell, J.B. Hunt, K. Molloy, M. O'Connell, 2004. Tephrostratigraphy of An Loch Mór, Inis Oírr, western Ireland: implications for Holocene tephrochronology in the northeastern Atlantic region. *The Holocene* 14(5), 703-720.
- Darbyshire, F.A., I.Th. Bjarnason, R.S. White, Ó.G. Flóvenz, 1998. Crustal structure above the Iceland mantle plume imaged by the ICEMELT refraction profile. *Geophysical Journal International* 135, 1131-1149.
- Davies, S.M., M. Elmquist, J. Bergman, B. Wohlfarth, D. Hammarlund, 2007. Cryptotephra sedimentation processes within two lacustrine sequences from west central Sweden. *The Holocene* 17(3), 1-13.
- Einarsson, P., 1991. Earthquakes and present-day tectonism in Iceland. *Tectonophysics* 189, 261-279.
- Foulger, G.R., M.J. Pritchard, B.R. Julian, J.R. Evans, R.M. Allen, G. Nolet, W.J. Morgan, B.H. Bergsson, P. Erlendsson, S. Jakobsdóttir, S. Ragnarsson, R. Stefansson, K. Vogfjörð, 2001. Seismic tomography shows that upwelling beneath Iceland is confined to the upper mantle. *Geophysical Journal International* 146, 504-530.
- Flóvenz, Ó.G., 1980. Seismic structure of the Icelandic crust above layer three and the relation between body wave velocity and the alteration of the basaltic crust. *Journal of Geophysics*. 47, 211-220.

- Flóvenz Ó.G., K. Gunnarson, 1991. Seismic crustal structure in Iceland and surrounding area. *Tectonophysics* 189, 1-17.
- Fowler, C.M.L, 1990. *The solid Earth: An introduction to global geophysics*. Cambridge University Press, Cambridge, 472pp.
- Francis, P., C. Oppenheimer, 2004. *Volcanoes*. Oxford University Press, Oxford, 521pp.
- Franzson, H., S.Th. Gudlaugsson, G.Ó. Fridleifsson, 2001. Petrophysical properties of Icelandic rocks. *Proceedings of the 6th Nordic Symposium on Petrophysics*. Trondheim, Norway, 1-14.
- Gebrande H., H. Miller, P. Einarsson, 1980. Seismic structure of Iceland along RRISP-profile I. *Journal of Geophysical Research* 47, 239-249.
- Geirsdóttir, Á., J. Eiríksson, 1994. Growth of an intermittent Ice Sheet in Iceland during the Late Pleistocene and Early Pleistocene. *Quaternary Research* 42, 115-130.
- Geshi, N., K. Németh, T. Oikawa, 2011. Growth of phreatomagmatic explosion craters: A model inferred from Suoana crater in Miyakejima volcano, Japan. *Journal of Volcanology and Geothermal Research* 201, 30-38.
- Grönvold, K., N. Óskarsson, S. Johnsen, H.B. Clausen, C.U. Hammer, G. Bond, E. Bard, 1995. Ash layers from Iceland in the Greenland GRIP ice core correlated with oceanic and land sediments. *Earth and Planetary Science Letters* 135, 149-155.
- Gudmundsson, A. 2000. Dynamics of volcanic systems in Iceland: examples of tectonism and volcanism at juxtaposed hot spot and mid-ocean ridge systems. *Annual Review of Earth and Planetary Sciences* 28, 107-140.
- Gudmundsson, M.T., 2005. Subglacial volcanic activity in Iceland. In: C. Caseldine, A. Russel, J. Harnadóttir, Ó. Knudsen (eds), *Iceland: Modern processes and past environments*. *Developments in Quaternary science* 5, Amsterdam, 127-151.
- Gudmundsson, M.T., J. Milsom, 1997. Gravity and magnetic studies of the subglacial Grimsvotn volcano, Iceland: Implications for crustal and thermal structure. *Journal of Geophysical Research* 102(B4), 7691-7704.
- Gudmundsson M.T., Th. Högnadóttir, 2001. Gravity surveying 1988-2001: Central volcanoes in the Eastern Volcanic Zone and hyaloclastite regions in the Western Volcanic Zone. *Raunvísindastofnun Háskólans*, Technical report RH-22-2001, Reykjavík.
- Gudmundsson, M.T., T. Högnadóttir, 2007. Volcanic systems and calderas in the Vatnajökull region, central Iceland: constraints on crustal structure from gravity data. *Journal of Geodynamics* 43, 153-169.
- Gudmundsson, M.T., F. Pálsson, H. Björnsson, Th. Högnadóttir, 2002. The hyaloclastite ridge formed in the subglacial 1996 eruption in Gjálpi, Vatnajökull, Iceland: present day shape and future preservation. In: J.L. Smellie, M.G. Chapman (eds), *Volcano-*

Ice Interactions on Earth and Mars. Geological Society, London, Special Publications 202, 319-336.

Hardarson B.S., J.G. Fitton, Á. Hjartarson, 2008. Tertiary volcanism in Iceland. *Jökull* 58, 161-178.

Hjartarson, Á., 1988. Þjórásáhraunið mikla - stærsta nútímahraun jarðar [The great Thjórásá lava - the largest Holocene lava on Earth. In Icelandic]. *Náttúrufræðingurinn*, 58(1), 1-16.

Houghton, B.F., C.J.N. Wilson, I.E.M. Smith, 1999. Shallow seated controls on styles of explosive basaltic volcanism: a case study in New Zealand. *Journal of Volcanology and Geothermal Research* 91, 97-120.

Houghton B.F., C.J.N. Wilson, R.T. Smith, J.S. Gilbert, 2000. Phreatoplinian eruptions. In: H. Sigurdsson, B.F. Houghton, S.R. McNutt, H. Rymer, J. Stix (eds), *Encyclopedia of volcanoes*. Academic Press, San Diego, 513-525.

IMO, 2005. [website] Icelandic Meteorological Office. Continuous GPS measurements in Iceland - the ISGPS network. Available from: <https://hraun.vedur.is/ja/englishweb/gps/isak.html>

International Association of Geodesy, 1980. The geodesist's handbook. *Bulletin Géodésique* 54.

Jakobsdóttir, S.S., 2008. Seismicity in Iceland: 1994-2007. *Jökull* 58, 75-100.

Jakobsson, S.P., 1979a. Petrology of recent basalts of the Eastern volcanic zone, Iceland. *Acta Naturalia Islandica* 26, Reykjavík, 103pp.

Jakobsson, S.P., 1979b. Outline of the petrology of Iceland. *Jökull* 29, 57-73.

Jakobsson, S.P., M.T. Gudmundsson, 2008. Subglacial and intraglacial volcanic formations in Iceland. *Jökull* 58, 179-197.

Jakobsson, S.P., K. Jónasson, I.A. Sigurdsson, 2008. The three igneous rock series of Iceland. *Jökull* 58, 117-138.

Jóhannesson H., K. Saemundsson, 1998. Geological map of Iceland, 1:500000. Bedrock geology. Icelandic Institute of Natural History and Iceland Geodetic Survey, Reykjavík.

Jónsson, S., P. Einarsson, F. Sigmundsson, 1997. Extension across a divergent plate boundary, the Eastern Volcanic Rift Zone, south Iceland, 1967-1994, observed with GPS and electronic distance measurements. *Journal of Geophysical Research* 102(B6), 11913-11929.

Kearey, P., M. Brooks, I. Hill, 2002. *An Introduction to Geophysical Exploration*. Blackwell Science Inc., 3rd Edition, Oxford, 256pp.

- Kokelaar, P., 1986. Magma-water interactions in subaqueous and emergent basaltic volcanism. *Bulletin of Volcanology* 48, 275-289.
- Kwon, C.W., Y.K. Sohn, 2008. Tephra-filled volcanic neck (diatreme) of a mafic tuff ring at Maegok, Miocene Eoil Basin, SE Korea. *Geosciences Journal* 12-4, 317-329.
- LaCoste & Romberg, Inc., 1979. Instruction manual for LaCoste & Romberg, Inc. model G gravity meter no. 445, Austin, Texas, 20pp.
- LaFemina, P.C., T.H. Dixon, R. Malservisi, T. Árnadóttir, E. Sturkell, F. Sigmundsson and P. Einarsson, 2005. Geodetic GPS measurements in south Iceland: strain accumulation and partitioning in a propagating ridge system. *Journal of Geophysical Research* 110, B11405.
- Larsen, G., 1984. Recent volcanic history of the Veidivötn fissure swarm, southern Iceland - an approach to volcanic risk assessment. *Journal of Volcanology and Geothermal Research* 22, 33-58.
- Larsen, G., 1988. Veidivötn og Veidivatnagos á 15 öld [Veidivötn lakes and the 15th century Veidivötn eruption. In Icelandic]. *Árbók Ferðafélags Íslands* 1988, 149-163.
- Larsen, G., 2002. A brief overview of eruptions from ice-covered and ice-capped volcanic systems in Iceland during the past 11 centuries: frequency, periodicity and implications. In: J.L. Smellie, M.G. Chapman (eds), *Volcano-Ice Interactions on Earth and Mars*. Geological Society, London, Special Publications 202, 81-90.
- Larsen, G., 2005. Explosive volcanism in Iceland: three examples of hydromagmatic basaltic eruptions on long volcanic fissures within the past 1200 years. *European Geosciences Union, Vienna, Austria, Geophysical Research Abstracts* 7, 10158.
- Larsen, G., J. Eiríksson, 2008a. Late Quaternary terrestrial tephrochronology of Iceland - Frequency of explosive eruptions, type and volume of tephra deposits. *Journal of Quaternary Science* 23, 109-120.
- Larsen, G., J. Eiríksson, 2008b. Holocene tephra archives and tephrochronology in Iceland - a brief overview. *Jökull* 58, 229-250.
- Larsen, G., J. Eiríksson, 2010. Explosive and partly explosive eruptions during the last millenium: Dispersal of airfall tephra and ocean-rafted pumice towards the North Icelandic Shelf. *Millennium SG 4: Marine Proxies for the Millenium*, University of Iceland, Reykjavík, Technical Report RH-07-2010.
- Larsen, G., M.T. Gudmundsson, H. Björnsson, 1998. Eight centuries of periodic volcanism at the centre of the Iceland hotspot revealed by glacier tephrostratigraphy. *Geology* 26, 943-946.
- Larsen, G., J. Eiríksson, K.L. Knudsen, J. Heinemeier, 2002. Correlation of late Holocene terrestrial and marine tephra markers, north Iceland: implications for reservoir age changes. *Polar Research* 21(2), 283-290.

- Larsen, G., Th. Thordarson, B.A. Óladóttir, 2008. Excursion 7 - Phreatomagmatism in the Eastern Volcanic Zone. IAVCEI 2008 Conference Field Excursions, Iceland.
- Larsen, G., M.T. Gudmundsson, P. Einarsson, T. Thordarson, 2013. Bardarbunga. In: J. Sólnes, F. Sigmundsson, B. Bessason (eds), Náttúruvá á Íslandi - Eldgos og Jarðskjálftar, Viðlagatrygging Íslands/Háskólaútgáfan, Reykjavík, 253-261.
- LMÍ, 2010. National Land Survey of Iceland (Landmælingar). IS 50V, digital database, version 3.0.
- LMÍ, 2011. National Land Survey of Iceland (Landmælingar). IS 50V, digital database, version 3.1.
- Longman, I.M., 1959. Formulas for computing the tidal correction due to the moon and the sun. *Journal of Geophysical Research* 64, 2351-2356.
- Lorenz, V., 1986. On the growth of maars and diatremes and its relevance to the formation of tuff rings. *Bulletin of Volcanology* 48, 265-274.
- Lorenz, V., 2000. Explosion and intrusions in rootzones of maar-diatreme volcanoes. Abstract, IAVCEI General Assembly 2000, Bali, Indonesia.
- Lorenz, V., 2003. Maar-diatreme volcanoes, their formation, and their setting in hard-rock or soft-rock environments. *Geolines* 15, 72-83.
- Lorenz, V., S. Kurszlaukis, 2007. Root zone processes in the phreatomagmatic pipe emplacement model and consequences for the evolution of maar-diatreme volcanoes. *Journal of Volcanology and Geothermal Research* 159, 4-32.
- Lorenz, V., A.R. McBirney, H. Williams, 1970. An investigation of volcanic depressions - Part III - Maar, tuff-rings, tuff-cones and diatremes. Manned Spacecraft Center, Houston Texas, 198pp.
- Lutz, P., 2009. La Gravimétrie. Lecture in Geophysics. Institut Polytechnique LaSalle Beauvais, Beauvais.
- Milsom, J., 2003. *Field Geophysics*. John Wiley & Sons Inc., 3rd Edition, Chichester, England, 222pp.
- Moore, J.G., K. Nakamura, A. Alcaraz, 1966. The 1965 Eruption of Taal volcano - Catastrophic explosions are caused by lake water entering a volcanic conduit. *Science* 151, 955-960.
- Morrissey, M., B. Zimanowski, K. H. Wohletz, R. Buttner, 2000. Phreatomagmatic fragmentation. In: H. Sigurdsson, B.F. Houghton, S.R. McNutt, H. Rymer, J. Stix (eds), *Encyclopedia of volcanoes*. Academic Press, San Diego, 431-445.
- Mrlina, J., H. Kämpf, W.H. Geissler, P. Van Den Bogaard, 2007. Assumed Quaternary maar structure at the Czech/German border between Mýtina and Neualbenreuth (western Eger Rift, Central Europe): geophysical, petrochemical and

- geochronological indications. *Zeitschrift für Geologische Wissenschaften* 35 (4-5), 213-230.
- Mrlina J., H. Kämpf, C. Kroner, J. Mingram, A. Brauer, W.H. Geissler, J. Kallmeyer, H. Matthes, M. Seidl, 2009. Discovery of the first Quaternary maar in the Bohemian Massif, Central Europe, based on combined geophysical and geological surveys. *Journal of Volcanology and Geothermal Research* 182, 97-112.
- Nagy, D., 1966 The gravitational attraction of a right rectangular prism. *Geophysics* 31(2), 362-371.
- Nettleton, L.L., 1976. Gravity and magnetics in oil prospecting. McGraw-Hill, New York, 464pp.
- Oddsson B., 2007. The Grímsvötn eruption in 2004: Dispersal and total mass of tephra and comparison with plume transport models. Master's thesis, University of Iceland, 76pp.
- Oddsson B., M.T. Gudmundsson, G. Larsen, S. Karlsdóttir, 2011. Monitoring of the plume from the basaltic phreatomagmatic 2004 Grímsvötn eruption - application of weather radar and comparison with the plume models. *Bulletin of Volcanology* 74, 1395-1407.
- OS, 1959a. National Energy Authority (Orkustofnun). Faxi, Sheet 3339 (OS-90), 1:20000, Energy base map series, Raforkumálastjóri. Available from: <http://orkuveysja.is>.
- OS, 1959b. National Energy Authority (Orkustofnun). Litlisjór, Sheet 3340 (OS-91), 1:20000, Energy base map series, Raforkumálastjóri. Available from: <http://orkuveysja.is>.
- OS, 1959c. National Energy Authority (Orkustofnun). Tjörfafell, Sheet 3439 (OS-106), 1:20000, Energy base map series, Raforkumálastjóri. Available from: <http://orkuveysja.is>.
- OS, 1960. National Energy Authority (Orkustofnun). Fontur, Sheet 3341 (OS-92), 1:20000, Energy base map series, Landsvirkjun. Available from: <http://orkuveysja.is>.
- OS, 1961a. National Energy Authority (Orkustofnun). Tungnaárkrokur, Sheet 3440 (OS-107), 1:20000, Energy base map series, Raforkumálastjóri. Available from: <http://orkuveysja.is>.
- OS, 1961b. National Energy Authority (Orkustofnun). Snoðnafit, Sheet 3441 (OS-108), 1:20000, Energy base map series, Raforkumálastjóri. Available from: <http://orkuveysja.is>.
- Óladóttir, B.A., G. Larsen, O. Sigmarsson, 2011. Holocene volcanic activity at Grímsvötn, Bárdarbunga and Kverkfjöll subglacial centres beneath Vatnajökull, Iceland. *Bulletin of Volcanology* 73, 1187-1208.
- Pálmason, G., 1971. Crustal structure of Iceland from explosion seismology. Prentsmiðjan Leiftur H. F., Reykjavík, 171pp.

- Pedley, R.C., J.P. Busby, Z.K. Dabek, 1993. Gravmag user manual: Interactive 2.5 D gravity and magnetic modelling. Regional Geophysics serie, British Geological survey, Nottingham, UK, Technical report WK/93/26/R, 51pp.
- Rout, D.J., J. Cassidy, C.A. Locke, I.E.M. Smith, 1993. Geophysical evidence for temporal and structural relationships within the monogenetic basalt volcanoes of the Auckland volcanic field, northern New Zealand. *Journal of Volcanological and Geothermal Research* 57, 71-83.
- Saemundsson, K., 1978. Fissure swarms and central volcanoes of the neovolcanic zones of Iceland. *Geological Journal Special Issue* 10, 415-432.
- Saemundsson, K., 1979. Outline of the geology of Iceland. *Jökull* 29, 7-28.
- Schopka, H.H., M.T. Gudmundsson, H. Tuffen, 2006. The formation of Helgafell, southwest Iceland, a monogenetic subglacial ridge: Sedimentology, hydrology and volcano-ice interaction. *Journal of Volcanology and Geothermal Research* 152, 359-377.
- Schulz, R., H. Buness, G. Gabriel, R. Pucher, C. Rolf, H. Wiederhold, T. Wonik, 2005. Detailed investigation of preserved maar structures by combined geophysical surveys. *Bulletin of Volcanology* 68, 95-106.
- Self, S., R.S.J. Sparks, 1978. Characteristics of widespread pyroclastic deposits formed by the interaction of silicic magma and water. *Bulletin of Volcanology* 41, 196-212.
- Sigmundsson, F., 2006. Iceland geodynamics, crustal deformation and divergent plate tectonics. Praxis Publishing, Springer Verlag, Chichester, UK, 209pp.
- Sleep, N.H., K. Fujita, 1997. Principles of Geophysics. Blackwell Science Inc., Malden, Massachusetts, 586pp.
- Sohn, Y.K., 2012. Hydrovolcanic processes forming basaltic tuff rings and cones on Cheju Island, Korea. *GSA Bulletin* 108, 1199-1211.
- Sopac, 2013. [website] Scripps Orbit and permanent Array Center. Archives of high-precision GPS data. Available from: <http://sopac.ucsd.edu>.
- Thorarinsson, S., 1976. Gjóskulög og gamlar rústir [Tephra layers and old ruins. In Icelandic]. *Árbók hins Íslenska Fornleifafélags* 1976, Reykjavík, 5-38.
- Thorarinsson, S., 1979. Tephrochronology and its applications in Iceland. *Jökull* 29, 33-36.
- Thorarinsson, S., K. Saemundsson, R.S. Williams, 1973. ERTS-1 Image of Vatnajökull: analysis of glaciological, structural and volcanic features. *Jökull* 23, 7-17.
- Thordarson, T., G. Larsen, 2007. Volcanism in Iceland in historical time: Volcano types, eruption styles and eruptive history. *Journal of Geodynamics* 43, 118-152.
- Thordarson, T., Á. Höskuldsson, 2008. Postglacial volcanism in Iceland, *Jökull* 58, 197-228.

- Thordarson, T., S. Self, D.J. Miller, G. Larsen, E.G. Vilmundardóttir, 2003. Sulphur release from flood lava eruptions in the Veiðivötn, Grímsvötn and Katla volcanic systems, Iceland. Geological Society, London, Special Publications 213, 103-121.
- Vespermann, D., H.U. Schmincke, 2000. Scoria cones and tuff rings. In: H. Sigurdsson, B.F. Houghton, S.R. McNutt, H. Rymer, J. Stix (eds), Encyclopedia of volcanoes. Academic Press, San Diego, 683-694.
- Vilhjálmsson, A. M., 2006. A gravity study of hyaloclastite formations and lava fields around Kleifarvatn, Reykjanes Peninsula, Iceland. Master's thesis, University of Iceland, Reykjavík, 82pp.
- Vilmundardóttir, E.G., 1977. Tungnaárhraun [The Tungnaá lava flows. In Icelandic]. Orkustofnun National Energy Authority, Reykjavík, Technical Report OS-ROD 7702, 156pp.
- Vilmundardóttir, E.G., S.P. Snorrason, G. Larsen, Á. Gudmundsson, 1988. Geological map, Sigalda-Veiðivötn, 3340 B, National Energy Authority, Hydro Power Division and the National Power Company, Reykjavík.
- Walker, G.P.L., 1973. Explosive eruptions - a new classification scheme. Geologische Rundschau 62, 431-446.
- Walker, G.P.L., 1980. The Taupo pumice: product of the most powerful known (ultraplinian) eruption?. Journal of Volcanology and Geothermal Research 8, 69-94.
- White, J.D.L., 1991. Maar-diatreme phreatomagmatism at Hopi Buttes, Navajo Nation (Arizona), USA. Bulletin of Volcanology 53, 239-258.
- White, J.D.L., B. Houghton, 2000. Surtseyan and related phreatomagmatic eruptions. In: H. Sigurdsson, B.F. Houghton, S.R. McNutt, H. Rymer, J. Stix (eds), Encyclopedia of volcanoes. Academic Press, San Diego, 495-511.
- White, J.D.L., P.S. Ross, 2011. Maar-diatreme volcanoes: A review. Journal of Volcanology and Geothermal Research 201, 1-29.
- Wohletz, K.H., 1983. Mechanisms of hydrovolcanic pyroclasts formation: grain size, scanning electron microscopy, and experimental studies. Journal of Volcanology and Geothermal Research 17, 31-63.
- Wohletz, K.H., M.F. Sheridan, 1983. Hydrovolcanic explosions II. Evolution of basaltic tuff rings and tuff cones. American Journal of Science 283, 385-413.
- Wolfe, C.J., I.Th. Bjarnason, J.C. Van Decar, S.C. Solomon, 1997. Seismic structure of the Icelandic plume. Nature 385, 245-247.
- Zellmer, G.F., K. H. Rubin, K. Grönvold and Z. Jurado-Chichay, 2008. On the recent bimodal magmatic processes and their rates in the Torfajökull-Veiðivötn area, Iceland. Earth and Planetary Science Letters 269, 387-397.

Zimanowski, B., 1998. Phreatomagmatic explosions. In: A. Freundt, M. Rosi (eds), From magma to tephra, Elsevier, Amsterdam, 25-54.

Appendix A

Gravity data

This appendix lists all the survey points that have been used for gravity modelling in the present study. A LaCoste&Romberg (G445) gravimeter and a kinematic Trimble GPS 5700 were used for gravity and elevation measurements, respectively (see section 4.1)

Explanations:

- g_{obs} Observed gravity values (see section 3.2.2). For all the survey points, the same base station JH (Jökulhleimar) was used (Table 1.4).
- Surveyors: JMG Jeanne M. Giniaux
ÞÁ Þorbjörg Ágústsdóttir
- ΔZ_{gps} Uncertainty in survey point elevation (see section 4.3.1)
- g_{BA} Complete Bouguer anomalies for $\rho = 2300 \text{ kg m}^{-3}$ (Equation 3.9)
- g_{FA} Free-air anomalies (Equation 3.8)
- $\text{TC}_{\text{B-C}}$ Terrain corrections of the Hammer zones B and C (see section 3.2.5).

Table A.1 Data of the survey points (from NW to SE) at the Va-1 profile.

Survey point	Lat. (°N)	Long. (°W)	Elev. (m a.s.l.)	g_{obs} (mGal)	Date yymmdd	Surveyor	ΔZ_{gps} (m)	g_{BA} (mGal)	g_{FA} (mGal)	$\text{TC}_{\text{B-C}}$ (mGal)
V401	64.12680	18.93899	608.5	982104.44	120713	JMG	0.3	22.91	64.66	0.00
V402	64.12510	18.93463	618.4	982101.85	120713	JMG	0.3	23.28	65.25	0.00
V403	64.12230	18.92817	649.5	982093.92	120713	JMG	0.3	24.34	67.11	0.00
V404	64.11816	18.91590	810.3	982053.89	120714	JMG	0.3	29.32	77.01	0.00
V405	64.11447	18.90013	616.6	982101.70	120714	JMG	0.3	22.98	65.29	0.00
V406	64.11375	18.89877	607.4	982103.87	120714	JMG	0.3	22.64	64.69	0.00
V407	64.11269	18.89676	593.8	982106.90	120714	JMG	0.3	22.20	63.58	0.00
V408	64.11126	18.89381	579.5	982110.14	120714	JMG	0.3	21.68	62.54	0.00
V409	64.10909	18.89053	565.8	982113.30	120714	JMG	0.3	21.25	61.59	0.00
V410	64.10342	18.87798	574.5	982113.05	120714	JMG	0.3	21.63	64.46	0.00

Table A.2 Data of the survey points (from NW to SE) at the Va-2 profile.

Survey point	Lat. (°N)	Long. (°W)	Elev. (m a.s.l.)	g_{obs} (mGal)	Date yymmdd	Surveyor	ΔZ_{gps} (m)	g_{BA} (mGal)	g_{FA} (mGal)	$\text{TC}_{\text{B-C}}$ (mGal)
V501	64.13494	18.91466	620.9	982103.55	120712	PÁ	0.3	23.37	67.04	0.00
V502	64.13263	18.91205	637.7	982098.66	120712	PÁ	0.3	23.98	67.51	0.00
V503	64.12976	18.90818	678.3	982088.63	120712	PÁ	0.3	25.42	70.21	0.02
V504	64.12566	18.89989	734.6	982073.23	120714	PÁ	0.3	27.12	72.49	0.03
V510	64.12174	18.89527	607.7	982104.57	120714	PÁ	0.3	22.64	64.92	0.11
V509	64.11965	18.89166	604.2	982105.79	120714	PÁ	0.3	22.70	65.18	0.00
V508	64.11820	18.88861	592.5	982108.15	120714	PÁ	0.3	22.23	64.05	0.00
V507	64.11669	18.88555	591.9	982107.46	120714	PÁ	0.3	22.20	63.31	0.01
V506	64.11578	18.88345	570.2	982112.94	120714	PÁ	0.3	21.44	62.15	0.00
V505	64.11450	18.88085	564.9	982114.33	120714	PÁ	0.3	21.27	61.97	0.00

Table A.3 Data of the survey points (from NW to SE) at the Va-3 profile.

Survey point	Lat. (°N)	Long. (°W)	Elev. (m a.s.l.)	g_{obs} (mGal)	Date yymmdd	Surveyor	ΔZ_{gps} (m)	g_{BA} (mGal)	g_{FA} (mGal)	$\text{TC}_{\text{B-C}}$ (mGal)
V204	64.17550	18.80703	601.4	982115.64	120712	JMG	0.3	22.74	70.23	0.00
V205	64.17433	18.80272	607.6	982113.53	120712	JMG	0.3	22.92	70.10	0.00
V206	64.17309	18.79821	615.7	982111.78	120712	JMG	0.3	23.23	70.91	0.00
V207	64.17186	18.79433	633.9	982106.36	120712	JMG	0.3	23.83	71.23	0.06
V208	64.17065	18.79073	689.2	982089.96	120712	JMG	0.3	24.89	71.96	0.44
V209	64.16949	18.78727	584.6	982117.78	120712	JMG	0.3	21.76	67.62	0.14
V210	64.16925	18.78640	577.1	982119.45	120712	JMG	0.3	21.60	66.98	0.01
V211	64.16894	18.78516	578.2	982119.42	120712	JMG	0.3	21.71	67.29	0.03
V212	64.16881	18.78381	591.0	982116.64	120712	JMG	0.3	22.21	68.46	0.10
V201	64.16714	18.77925	574.1	982120.85	120711	JMG	0.3	21.63	67.58	0.00
V202	64.16490	18.77464	576.5	982119.43	120711	JMG	0.3	21.71	67.09	0.00
V203	64.16367	18.76959	613.6	982112.12	120711	JMG	0.3	23.07	71.29	0.02

Table A.4 Data of the survey points (from NW to SE) at the Va-4 profile.

Survey point	Lat. (°N)	Long. (°W)	Elev. (m a.s.l.)	g_{obs} (mGal)	Date yymmdd	Surveyor	ΔZ_{gps} (m)	g_{BA} (mGal)	g_{FA} (mGal)	$\text{TC}_{\text{B-C}}$ (mGal)
V311	64.17944	18.79623	602.7	982115.86	120712	JMG	0.3	22.71	70.54	0.00
V310	64.17762	18.78950	611.1	982112.88	120712	JMG	0.3	23.06	70.28	0.00
V309	64.17581	18.78586	620.5	982111.08	120712	JMG	0.3	23.38	71.50	0.02
V308	64.17462	18.78308	667.0	982097.01	120712	JMG	0.3	24.44	71.91	0.16
V307	64.17348	18.78066	585.4	982118.04	120712	JMG	0.3	21.86	67.82	0.09
V306	64.17303	18.77992	582.6	982118.56	120712	JMG	0.3	21.85	67.54	0.00
V305	64.17274	18.77946	584.5	982118.32	120712	JMG	0.3	21.93	67.88	0.06
V304	64.17242	18.77841	604.8	982113.64	120712	JMG	0.3	22.70	69.46	0.19
V303	64.17190	18.77684	580.2	982119.92	120712	JMG	0.3	21.82	68.22	0.13
V302	64.17060	18.77300	589.5	982117.83	120711	JMG	0.3	22.23	69.06	0.00
V301	64.16921	18.76876	591.4	982116.89	120711	JMG	0.3	22.33	68.83	0.00

Table A.5 Data of the survey points (from NW to SE) at the Ve-1 profile.

Survey point	Lat. (°N)	Long. (°W)	Elev. (m a.s.l.)	g_{obs} (mGal)	Date yymmdd	Surveyor	ΔZ_{gps} (m)	g_{BA} (mGal)	g_{FA} (mGal)	$\text{TC}_{\text{B-C}}$ (mGal)
V712	64.14079	18.80787	579.2	982115.41	120713	JMG	0.3	21.84	65.59	0.00
V711	64.13897	18.80225	584.4	982114.46	120713	JMG	0.3	22.06	66.36	0.00
V709	64.13757	18.79901	598.3	982111.53	120713	JMG	0.3	22.58	67.85	0.00
V710	64.13617	18.79493	588.1	982114.53	120713	JMG	0.3	22.16	67.83	0.01
V704	64.13403	18.79326	568.9	982119.44	120713	JMG	0.3	21.46	66.94	0.02
V703	64.13423	18.79110	568.8	982119.58	120713	JMG	0.3	21.45	67.05	0.00
V702	64.13315	18.78723	568.7	982119.20	120713	JMG	0.3	21.42	66.70	0.00
V705	64.13277	18.78597	569.0	982118.42	120713	JMG	0.3	21.41	66.01	0.02
V701	64.12997	18.77526	617.1	982105.63	120711	JMG	0.3	23.24	68.32	0.00
V706	64.13002	18.77082	605.4	982108.65	120713	JMG	0.3	22.83	67.73	0.01
V707	64.12880	18.76499	591.4	982112.89	120713	JMG	0.3	22.35	67.71	0.00
V708	64.12721	18.75599	586.1	982115.13	120713	JMG	0.3	22.10	68.43	0.00

Table A.6 Data of the survey points (from NW to SE) at the Ve-2 profile.

Survey point	Lat. (°N)	Long. (°W)	Elev. (m a.s.l.)	g_{obs} (mGal)	Date yymmdd	Surveyor	ΔZ_{gps} (m)	g_{BA} (mGal)	g_{FA} (mGal)	$\text{TC}_{\text{B-C}}$ (mGal)
V109	64.15754	18.75612	582.1	982118.22	120710	JMG	0.3	21.93	68.10	0.00
V112	64.15548	18.74957	596.5	982114.37	120711	JMG	0.3	22.49	68.88	0.00
V113	64.15484	18.74764	579.6	982118.51	120711	JMG	0.3	21.85	67.81	0.00
V114	64.15452	18.74631	580.3	982118.15	120711	JMG	0.3	21.86	67.73	0.00
V115	64.15361	18.74348	580.0	982117.88	120711	JMG	0.3	21.90	67.43	0.00
V116	64.15313	18.74214	578.3	982117.90	120711	JMG	0.3	21.74	66.93	0.01
V117	64.15193	18.73762	645.8	982100.44	120711	JMG	0.3	24.07	70.42	0.00
V120	64.15104	18.73289	612.5	982108.45	120711	JMG	0.3	23.07	68.22	0.01
V118	64.14932	18.72518	589.8	982114.37	120711	JMG	0.3	22.27	67.26	0.00
V119	64.14541	18.71707	631.1	982104.69	120711	JMG	0.3	23.67	70.57	0.01

Appendix B

Density measurements

This appendix lists the density values measured for three samples collected on the northwestern side of the Va-3 profile. For all three samples, the surveyor was Þorsteinn Jónsson and the technician was Jeanne M. Giniaux.

Both wet and dry densities were calculated by dividing each mass by its volume. A constant volume of 0.0005 m³ was weighted for all the measurements (see section 4.3.4.2).

Table B.1 Density measurements of the samples in wet conditions.

Sample	Lat. (°N)	Long. (°W)	Mass (g)	Density (kg m ⁻³)	Sample description
S1	64.17182	18.79388	490.91	981.82	lapilli size
S2	64.17065	18.79900	942.18	1884.36	ash size
S3	64.17042	18.79726	949.45	1898.9	ash size

Table B.2 Density measurements of the dried lapilli-sized tephra S1 (64.17182°N; 18.79388°W).

Sample	Mass (g)	Density (kg m ⁻³)
S1a	438.44	876.88
S1b	394.36	788.72
S1c	394.02	788.04
S1d	408.13	876.26
S1e	413.99	827.98
S1f	397.15	794.30
S1g	396.91	793.82
S1h	372.16	744.32
S1i	416.91	833.82
S1j	390.75	781.50
Mean values	402.28	804.56

Table B.3 Density measurements of the dried ash-sized tephra S2 (64.17065°N; 18.79900°W).

Sample	Mass (g)	Density (kg m⁻³)
S2a	716.40	1432.80
S2b	726.72	1453.44
S2c	711.17	1422.34
S2d	720.96	1441.92
S2e	709.66	1419.32
S2f	706.68	1413.36
S2g	708.17	1416.34
S2h	729.55	1459.10
S2i	698.59	1397.18
S2j	689.14	1378.28
Mean values	711.70	1423.41

Table B.4 Density measurements of the dried ash-sized tephra S3 (64.17042°N; 18.79726°W).

Sample	Mass (g)	Density (kg m⁻³)
S3a	789.83	1579.66
S3b	756.24	1512.48
S3c	749.14	1498.28
S3d	779.32	1558.64
S3e	771.81	1543.62
S3f	765.01	1530.02
S3g	783.40	1566.80
S3h	771.84	1543.68
S3i	791.12	1582.24
S3j	777.01	1554.02
Mean values	773.47	1546.94